RADIATION-TOLERANT FERROELECTRIC MATERIALS FOR MULTIFUNCTIONAL DEVICES

A Dissertation
Presented to
The Academic Faculty

by

Evelyn S. Chin

In Partial Fulfillment
of the Requirements for the Degree
Doctor of Philosophy in the
School of Materials Science & Engineering

Georgia Institute of Technology
August 2020

RADIATION-TOLERANT FERROELECTRIC MATERIALS FOR MULTIFUNCTIONAL DEVICES

Approved by:

Dr. Nazanin Bassiri-Gharb, Advisor
School of Materials Science and Engineering
Georgia Institute of Technology

Dr. Mark Losego
School of Materials Science and Engineering
Georgia Institute of Technology

Dr. Eric Vogel
School of Materials Science and Engineering
Georgia Institute of Technology

Dr. Asif Khan
School of Electrical Engineering
Georgia Institute of Technology

Dr. Chaitanya Deo
School of Mechanical Engineering
Georgia Institute of Technology

Date Approved: [July 13, 2020]

To the LGBTQ+ and BIPOC who were never allowed an opportunity to pursue a Ph.D.

ACKNOWLEDGEMENTS

First, and foremost, I would like to give the biggest thanks to my advisor, Prof. Bassiri-Gharb, for allowing me the incredible opportunity to be a part of her group. Her unwavering guidance and support in every step of my graduate career has undoubtedly shaped me into a stronger person, in academia and in life. I will forever be inspired by her passionate leadership, and hope that someday I may impact others as positively as she has impacted me.

I would like to thank my committee members: Prof. Deo, Prof. Khan, Prof. Losego, and Prof. Vogel for volunteering their time to ask challenging questions and provide excellent research advice for my thesis.

I thank my parents for supporting me throughout my entire life; without them this journey would have been much more difficult. I also thank my friends from high school, college, graduate school, and online communities for giving me much needed emotional support throughout the years.

Finally, I thank all those who have helped me one way or another with the work presented in this thesis: Steven Brewer, Carmen Deng, Yulian Yao, Lee Griffin, Kerisha Williams, Sam Williams, Valeria Boesch, Grace Wei, Carl Morandi, David Tavakoli, Eric Woods, Charlie Suh, Cory Cress, Ryan Rudy, Shimeng Yu, Jae Hur, and anyone else I may have forgotten.

TABLE OF CONTENTS

LIST OF TABLES

LIST OF FIGURES

LIST OF SYMBOLS AND ABBREVIATIONS

2-MOE	2-Methoxyethanol
A	Cross-sectional area of parallel plate capacitor, equal to top electrode area
AFM	Atomic force microscopy
ARL	US Army Research Laboratory
BOE	Buffered oxide etch
C	Capacitance
CMOS	Complementary metal-oxide-semiconductor
CSD	Chemical solution deposition
C-V	Capacitance-voltage (permittivity-field measurement)
d	Thickness of dielectric media in parallel plate capacitor, equal to film thickness
d'	Real component of the piezoelectric coefficient
d''	Imaginary component of the piezoelectric coefficient
d_{33}	Converse piezoelectric coefficient
$d_{33,f}$	Effective, converse piezoelectric coefficient
$d_{33,f,remanent}$ ($d_{33,f,rem}$)	Remanent, effective, converse piezoelectric coefficient
$d_{33,f,saturation}$ ($d_{33,f,sat}$)	Saturation, effective, converse piezoelectric coefficient
DBLI	Double beam laser interferometer
D_i	Electric displacement field
DI	Deionized (water)
d_{ij}	Longitudinal piezoelectric coefficients tensor (reduced engineering notation)

d_{ijk}	Longitudinal piezoelectric coefficients tensor
d_{init}	Reversible Rayleigh piezoelectric parameter
d_{space}	Interatomic spacing of atoms in crystal lattice
E	Electric field
E_{AC}	AC electric field
E_c	Coercive field
E_{DC}	DC electric field
EDX	Energy dispersive X-ray spectroscopy
e_{ij}	Transverse piezoelectric coefficients tensor (reduced engineering notation)
e_{kij}	Transverse piezoelectric coefficients tensor
$E_{internal}$	Horizontal shift in polarization-field and piezoelectric response hysteresis loops, equal to internal electrical bias
E_{th}	Threshold electric field for nonlinear AC dielectric response
FeRAM	Ferroelectric random access memory (RAM)
FE-SEM	Field-emission scanning electron microscopy
HAADF	High-angle annular dark field
HZO	$HfZrO_2$
I	Intensity (of collected diffracted X-rays)
I-E	Switching current-electric field
LCR	Inductance, capacitance, resistance
M	Molarity
MEMS	Microelectromechanical systems
MLCC	Multilayer ceramic capacitor
MPB	Morphotropic phase boundary
n	Diffraction order, Brag’s law

NRL	US Naval Research Laboratory
P	Polarization response
PDF	Powder diffraction file
P-E	Polarization-electric field (hysteresis loop measurement)
PEALD	Plasma-enhanced atomic layer deposition
PEB	Post-exposure bake
P_{LF}	Lotgering factor peak summations
PMN-PT	$Pb(Mg_{1/3}Nb_{2/3})O_3$-$PbTiO_3$ (lead magnesium niobate-lead titanate)
PR	Photoresist
P_{rem}	Remanent polarization
P_{sat}	Saturated polarization
PTFE	Polytetrafluoroethylene
PTO	$PbTiO_3$ (lead titanate)
PZT	$Pb(Zr,Ti)O_3$ (lead zirconate titanate)
RID	Radiation-induced degradation
RTA	Rapid thermal annealer
SEM	Scanning electron microscopy
STEM	Scanning transmission electron microscopy
T	Temperature
$\tan(\delta)$	Dielectric loss tangent; dissipation factor
T_C	Curie (transition) temperature
TEM	Transmission electron microscopy
THALD	Thermal atomic layer deposition
TID	Total ionization dose
V	Electrical bias

x	Percent composition
x_{ij}	Mechanical strain matrix
XPS	X-ray photoelectron spectroscopy
XRD	X-ray diffraction
α	Irreversible Rayleigh parameter
α'	Real component of irreversible Rayleigh parameter
ε	Dielectric permittivity
ε'	Real component of the dielectric permittivity
ε''	Imaginary component of the dielectric permittivity
ε_0	Permittivity of free space
ε_{init}	Reversible Rayleigh parameter
$\varepsilon_{paraelectric}$	Paraelectric contribution to the dielectric response
ε_r	Relative dielectric permittivity
θ	Diffraction angle
λ	Wavelength
σ_i	Mechanical stress matrix (reduced engineering notation)
σ_{ij}	Mechanical stress matrix
τ	Shear stress
χ_{ij}	Dielectric susceptibility

SUMMARY

Ferroelectric materials have switchable, spontaneous polarization. Additionally, they exhibit large dielectric, pyroelectric and piezoelectric properties, making them ideal for numerous microelectronic devices, including mechanical logic elements, optical sensors and transducers, precision positioners, energy harvesting units, nonvolatile memory storage, and microelectromechanical systems (MEMS) sensors and actuators. Due to their radiation tolerance, ferroelectric materials have also become attractive for use in devices for radiation-hostile environments such as in aerospace, medical physics, x-ray/high energy source measurement tools, and nuclear monitoring systems.

A common ferroelectric material for many microelectronic applications, including piezoelectric MEMS devices and ferroelectric memory devices, due to its high functional properties is lead zirconate titanate (PZT). However increasing demand for smaller device footprint has pushed research efforts on PZT towards its limitations, creating a need for new material systems to exceed the current standards. Of particular interest among these for piezoelectric MEMS applications is $(1\text{-}x)Pb(Mg_{1/3}Nb_{2/3})O_3\text{-}xPbTiO_3$, PMN-PT, a relaxor-ferroelectric solid solution, which in bulk crystalline form exhibits even larger electromechanical response than ceramic PZT. Furthermore, PMN-PT's increased chemical heterogeneity promises even greater radiation hardness with respect to PZT films. In this work, PMN-PT thin films are defect engineered through the variation of processing parameters via chemical solution deposition. Total ionization dose (TID) studies are performed by irradiating films with a ^{60}Co source to explore PMN-PT's radiation tolerance. The role of grain morphology, porosity, and crystallization interfaces on the radiation tolerance of PMN-PT are also studied. The PMN-PT thin films exhibited equivalent to superior radiation tolerance than PZT while maintaining higher functional response. While the microstructure has a strong effect on the overall functional response of the material, it has little to no effect on the radiation tolerance of PMN-PT, suggesting that the radiation tolerance of PMN-PT is largely due to its inherent properties.

$HfZrO_2$ (HZO) is another alternative ferroelectric material of particular interest for use in non-volatile memory applications, where their nanometer thin films as well as CMOS compatibility allows for fabrication of small and complex 3D structures to optimize for both device size and efficiency. In this work, TID studies are performed on plasma-enhanced atomic layer deposited (PEALD) films and thermal atomic layer deposited (THALD) films to identify which has greater radiation tolerance, and to further identify the differences in defects which dictate the ferroelectricity of the films. While both showed significant degradation from aging, the PEALD films exhibited more stable functional response after gamma-radiation doses up to 5 Mrad(Si).

Radiation studies on these alternative material systems in relation to processing-structure-property provides a better understanding of the mechanisms responsible for both functional response and radiation tolerance. The studies illustrate different pathways for concomitant enhanced functionality and higher radiation tolerance in ferroelectric thin films.

CHAPTER 1. INTRODUCTION

This chapter outlines the motivation for the research and work undertaken, including the main objectives for this thesis. A basic overview of ferroelectrics, the selected material systems for this study, as well as radiation effects on materials is presented.

1.1 Introduction

With the development of advanced technologies, a constant move towards more efficient devices with smaller footprints has led to an increased interest in ferroelectric materials for their superior functional properties. Their large dielectric, piezoelectric, pyroelectric, and polarization properties have led to their use in various applications including multi-layer ceramic capacitors (MLCC), non-volatile logic and memory elements (FeRAM), microelectromechanical system (MEMS) sensor and actuators, and energy harvesting systems. The strong functional properties of ferroelectric materials is largely due to the formation of ferroelectric domains and motion of domain walls within the material. Additionally, there has been increased interest in utilizing these devices in radiation-hostile environments, such as in aerospace, medical physics tools, and nuclear facilities. Studies on common ferroelectric material lead zirconate titanate (PZT) have shown promisingly high radiation tolerance, however attempts to further optimize this radiation tolerance often leads to a degradation of the overall functional response. Therefore, it is necessary to explore other material systems which may provide equivalent or greater functional response in addition to high radiation tolerance.

This work presents two material systems which can be leveraged for use in MEMS and/or memory devices, especially in radiation-hostile environments. The first material system presented is the relaxor-ferroelectric solid solution $Pb(Mg_{1/3}Nb_{2/3})O_3$-$PbTiO_3$ (PMN-PT). While this material system can exhibit heightened response in comparison to PZT, it is also subject to extreme processing challenges in thin film form, namely the formation of pores and cracks. The general inconsistencies within the literature on processing of PMN-PT thin films presents additional challenges to moving the science forward. This work aims to shed light on the challenges and inconsistencies associated with fabrication of PMN-PT thin films through exploration of various processing parameters via chemical solution deposition (CSD), including precursor solution concentration and content, seed layer composition, spin-coating speeds and durations, drying and pyrolysis temperatures and durations, as well as crystallization temperatures and durations. General trends are observed in the optimization of both the microstructure and the functional response of the material, such as the utilization of greater excess Pb content in the PMN-PT/seed layer precursor solutions and increased crystallization temperatures for highly (001)-oriented films with large, columnar grain growth and ultimately maximal functional response.

A comparison study is conducted between the radiation tolerances of PMN-PT thin films and PZT thin films in order to confirm PMN-PT's viability as an alternative material system. The study further expands knowledge in how defect-defect interactions can dictate both the functional properties and the radiation tolerance in different materials. Across all functional responses, PMN-PT showed equivalent or superior radiation tolerance than the

PZT thin films under gamma-radiation doses up to 10 Mrad(Si). In PZT films, the generation of more mobile oxygen vacancies ultimately leads to the degradation in response after irradiation. The collection of these oxygen vacancies at particular interfaces leads to a substantial reduction in the dielectric, ferroelectric, and piezoelectric properties. The chemical heterogeneity as well as domain wall concentration in PMN-PT may have contributed to the decreased generation of oxygen vacancies as well as increased resilience against those introduced.

The various processing parameters are leveraged to engineer specific microstructural defects within the PMN-PT thin films to gain further understanding of the underlying mechanisms to the material's radiation tolerance. The increased interfacial regions due to the grain structure and porosity of the PMN-PT films could potentially act as defect sinks, improving the radiation tolerance of the PMN-PT thin films. Therefore, studies were conducted on PMN-PT thin films processed with varying microstructures with marked differences in the porosity and grain boundary structure and concentration. While the higher presence of interfacial regions led to decreased overall functional response, these interfacial regions showed little to no effect on radiation tolerance, confirming that the radiation tolerance of PMN-PT is due to its inherent properties mentioned previously.

The second material system studied in this thesis is $Hf_xZr_{(1-x)}O_2$ (HZO). Ferroelectric HZO films are able to exhibit high polarization properties at just a few nanometers thick, making them an attractive candidate for memory devices. Traditionally these materials are fabrication via thermal atomic layer deposition (THALD), an ideal method for processing of small and complex structures for microelectronic devices.

However recent efforts in the optimization in fabrication of the ferroelectric phase in HZO thin films has led to the use of a new technique, plasma-enhanced atomic layer deposition (PEALD), which allows for even lower processing thermal budgets. In this work, PEALD and THALD processed ferroelectric HZO thin films are irradiated to both understand how the materials behave under radiation exposure and also elucidate the differences in their defect landscapes and subsequent functional response. It is found that while both films are greatly affected by aging, the PEALD films exhibit much more stable properties after gamma-radiation doses up to 5 Mrad(Si).

The study of new material systems for radiation tolerant ferroelectric materials leverages an increased understanding of the inherent material properties as well as processing procedures which can provide both high functional properties as well as high radiation tolerance. This work presents alternative materials which have not yet been fully understood in the context of processing optimization or radiation tolerance in an effort to gain a better understanding of the underlying mechanisms responsible for these specific properties. Thus, the overarching goal of this research is to understand the physical phenomena responsible for both high functioning and high radiation tolerant material systems through uncovering the material characteristics which promote radiation tolerance.

1.2 Thesis Organization

Literature Review (Chapter 2)

Background information is provided on ferroelectricity, defects, radiation, as well as the materials presented in this work. Methods to measure the dielectric, polarization, and piezoelectric response are reviewed, including the Rayleigh law analysis for quantify intrinsic and extrinsic contributions. Defects in ferroelectric thin films from processing and radiation exposure and their subsequent effects on functional response are discussed. Recent techniques on chemical solution deposition of PMN-PT thin films and atomic layer deposition of ferroelectric HZO thin films are also reviewed.

Experimental Procedures (CHAPTER 3)

This chapter details the processing and characterization of PMN-PT and HZO thin films as investigated in this work. This includes synthesis of precursor solutions, substrate stack/bottom electrode, film deposition, top electrode deposition, in addition to procedures for microstructural, dielectric, piezoelectric, and polarization characterization. The details of the radiation exposure experiments will also be presented.

Defect Engineering PMN-PT Thin Films (CHAPTER 4)

This chapter focuses on the relations between processing and microstructure in PMN-PT thin films. Microstructural differences such as orientation, porosity, grain size, and grain growth were controlled by varying parameters of the chemical solution deposition process. The impact of microstructure on dielectric, polarization, and piezoelectric response is also studied. Increased Pb content in precursor solutions, decreased solution molarity, and increased crystallization temperatures are found to lead to large, columnar grains and maximal response.

Radiation Tolerance of PMN-PT Thin Films vs PZT Thin Films (CHAPTER 5)

This chapter examines the radiation tolerance of PMN-PT thin films after gamma-radiation exposure. The results are compared with similar studies previously conducted on PZT thin films. It is revealed that the PMN-PT films show equivalent or superior radiation tolerance than PZT films in dielectric, polarization, and piezoelectric responses, attributed to its inherent properties such as chemical heterogeneities or greater domain wall movements.

Processing-Structure-Property Relations on Radiation Tolerance of PMN-PT Thin Films (CHAPTER 6)

Further radiation studies are conducted on defect-engineered PMN-PT thin films to elucidate the role of microstructure on the thin films' radiation tolerance. While the microstructure was found to have strong effects on the functional response of the films, it exhibited little to no effect on the radiation tolerance, further confirming that PMN-PT's radiation tolerance is due to its inherent properties.

Processing-Structure-Property Relations on Radiation Tolerance of HZO Thin Films (CHAPTER 7)

This chapter explores the radiation tolerance of ferroelectric HZO thin films processed with different techniques. Gamma radiation studies are conducted on ferroelectric HZO thin films fabricated via either plasma-enhanced atomic layer deposition or thermal atomic layer deposition, and the defects responsible for their radiation tolerance are discussed. While both films showed large degradation through aging, the films still showed strong radiation tolerance. The PEALD films showed more stable polarization response across all doses studied, possibly related to the stability of the ferroelectric phase in its pristine state.

Conclusions and Future Work (CHAPTER 8)

The overall results and findings of this work are summarized in this chapter, and suggestions for future work is provided.

CHAPTER 2. BACKGROUND AND LITERATURE REVIEW

This chapter aims to give background information on the literature relevant to the current investigation. Information regarding ferroelectricity and ferroelectric materials is discussed, including the origins of ferroelectricity, ferroelectric domains, hysteretic behavior, and contributions to dielectric and piezoelectric response. Relevant materials (PMN-PT and HZO) pertinent to this work are introduced, and processing techniques used to optimize their functional response are discussed. Furthermore, defects created by radiation exposure are discussed, and put into context of ferroelectric materials.

2.1 Piezoelectricity

Piezoelectricity is the development of polarization from the application of a stress or strain. The converse also holds true wherein the material develops a stress or strain under an applied field. Piezoelectric materials exist with asymmetric electrical dipoles caused by ions in the crystal lattice with asymmetric charge surroundings. Within the 32 crystallographic point groups, the 20 non-centrosymmetric point groups are able to exhibit piezoelectricity (point group 432, although non-centrosymmetric, also contains symmetry elements which does not allow piezoelectricity).

For the piezoelectric effect, the electrical charge density, D_i, and the stress, σ_{jk}, or strain, x_{jk}, are related by the following equations:

$$D_i = d_{ijk}\sigma_{jk} \text{ or } D_i = e_{ijk}x_{jk} \qquad 1\text{-}1$$

where d_{ijk} and e_{ijk} are third rank tensor piezoelectric coefficients, related by the appropriate stiffness tensor.[1] For the converse piezoelectric effect, the applied electric field, E_k, and the stress or strain are related by the following equations:

$$x_{ij} = d_{kij}E_k \ or \ \sigma_{ij} = e_{kij}E_k \qquad 1\text{-}2$$

These equations can also be reduced into the following forms for practical use and reference:

$$D_i = d_{ij}\sigma_j \ or \ D_i = e_{ij}x_j \qquad 1\text{-}3$$

$$x_i = d_{ij}E_j \ or \ \sigma_i = e_{ij}E_j \qquad 1\text{-}4$$

The coupling coefficients are then noted as d_{ij} or e_{ij}, where i is the electric displacement field component, D_i, and σ_{ij} and x_{ij} reduce to σ_j and x_j, respectively.[2] The index j is a reduction of the mechanical stress or strain: j = 1, 2, or 3 describe the normal stresses along the x_1, x_2, and x_3 directions respectively. The shear stresses τ_{12}, τ_{13}, and τ_{23} are replaced by σ_4, σ_5, and σ_6, and similar reductions are made for the shear strains.[2] When a field is applied across the thickness of a material, x_3, the relevant piezoelectric coefficient is d_{33}, also known as the longitudinal piezoelectric coefficient.

2.2 Ferroelectricity

A subset of piezoelectric materials can also exhibit ferroelectricity, described as a switchable, spontaneous polarization.[3,4] Ferroelectric materials exhibit at least two equivalent spontaneous polarization directions for a given temperature range. In addition to this spontaneous polarization, ferroelectric materials can also exhibit strong pyroelectric, piezoelectric, and dielectric response.[3] These materials are formed when cooled to below the Curie temperature, T_C, at which point the material undergoes a phase change from the paraelectric to the ferroelectric phase. In this process, domains are formed to minimize elastic and electrostatic energy in the system. A domain is a volume of material with uniform dipole direction. Domain walls are formed between domains, and are identified based on the angle between the dipole directions of the adjacent domains, as depicted in Figure 2-1.[3,5]

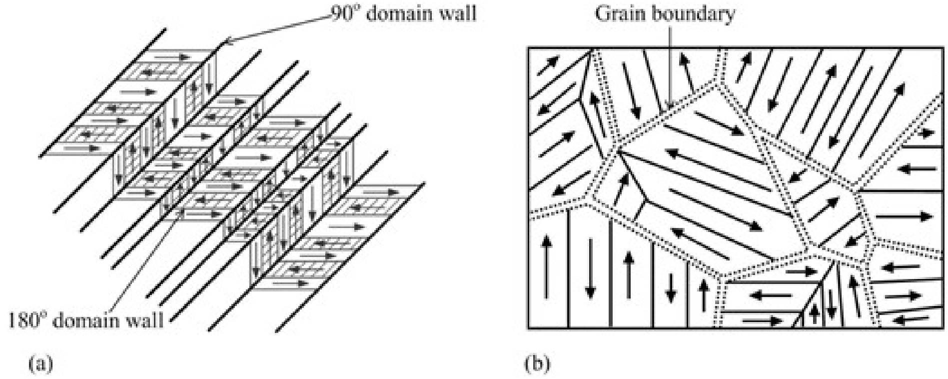

Figure 2-1 Domains and domain walls which form from cooling paraelectric materials to the ferroelectric phase.[5]

Unique to ferroelectric materials is the hysteretic behavior in polarization response. The hysteresis in polarization-electric field loop appears due to the domain nucleation and domain wall motion. Polarization saturation occurs when the domains grow and merge into an ideally single domain at large enough electric fields. The electrical polarization vector P is related to the dielectric susceptibility, χ_{ij}, and electric field vector E as follows:

$$P_i = \chi_{ij} E_j \tag{1-1}$$

In the virgin state of a polycrystalline ferroelectric material (point O), applying an electric field initially linearly increases the polarization (constant dielectric susceptibility). With increasing electric fields, the polarization becomes nonlinear due to domain wall motion. As depicted in Figure 2-2, electric field is increased, the domains switch to increase alignment with the applied electric field until polarization saturation (P_{sat+}) is eventually reached (point A).[6] Some of these domains will switch back as the electric field decreases, however a portion of the spontaneous polarization will remain at zero field (point B), called the positive remanent polarization (P_{rem+}). As the electric field is reversed into the negative direction, small domain nucleation begins as the domains switch to the opposite direction, until reaching a net zero polarization (point C), called the negative coercive field (E_{c-}). Again, the domains will continue to switch and increase alignment with the increasing

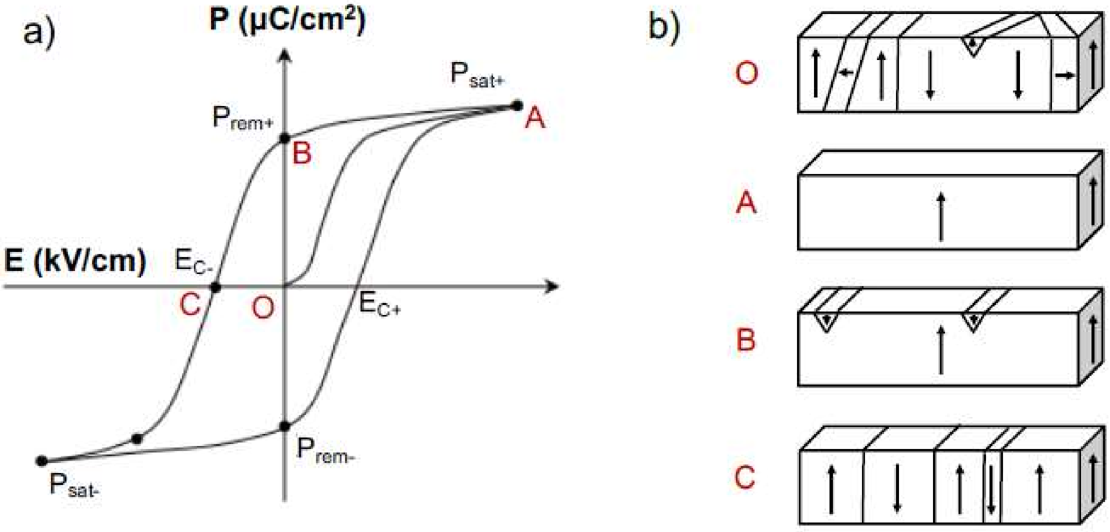

Figure 2-2 Schematic representation of (a) polarization-electric field loop and (b) domain states at particular points along the hysteresis loop. Adapted from Ref. 6.

magnitude in applied electric field until negative polarization saturation (P_{sat-}) is reached. Decreasing the magnitude of the electric field will repeat the process in the opposite direction, reaching the negative remanent polarization (P_{rem-}) at zero field followed by the positive coercive field (E_{c+}) at zero polarization until reaching P_{sat+} once more.

This hysteretic behavior is also observed when measuring the strain vs. AC electric field, referred as the "butterfly loops" (Figure 2-3a).[7] Applying a DC field to a ferroelectric material will also result in a hysteretic behavior in the effective converse piezoelectric coefficient, d_{33} (Figure 2-3b).[8] A small AC electric field signal is typically superimposed on the DC bias to perform this measurement, and piezoelectric response is measured in DC bias intervals.

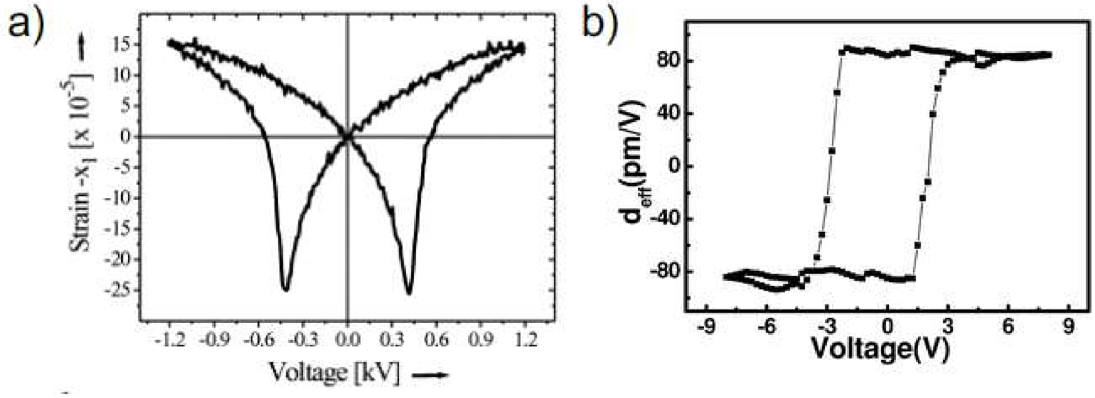

Figure 2-3 Representative (a) strain-electric field and (b) effective converse piezoelectric coefficient-DC hysteresis loops in polycrystalline ferroelectric materials.[7,8]

2.3 Perovskite Structure

The most commonly studied crystal structure in ferroelectrics is the perovskite structure. The typical perovskite structure follows the chemical formula ABO_3, where A and B are typically two different cations, and O is the anion to the two cations. In general, the A-site cations form a body-centered cubic type structure surrounding a B-site cation body center with oxygen atoms occupying the octahedral sites. Due to the instability of the cubic phase at low temperatures, the crystal structure will distort and lead to complex structural phase diagrams, giving rise to ferroelectricity.[9] Figure 2-4 depicts one of the crystallographic phase changes the perovskite structure of a ferroelectric material can undergo when cooled to below T_C. The material shifts from the paraelectric cubic phase to the ferroelectric tetragonal phase, where the center B-site cation is shifted, inducing a spontaneous polarization. Common ferroelectric materials include $BaTiO_3$ for multi-layered ceramic capacitors, $PbTiO_3$ for transducers and optoelectronics.

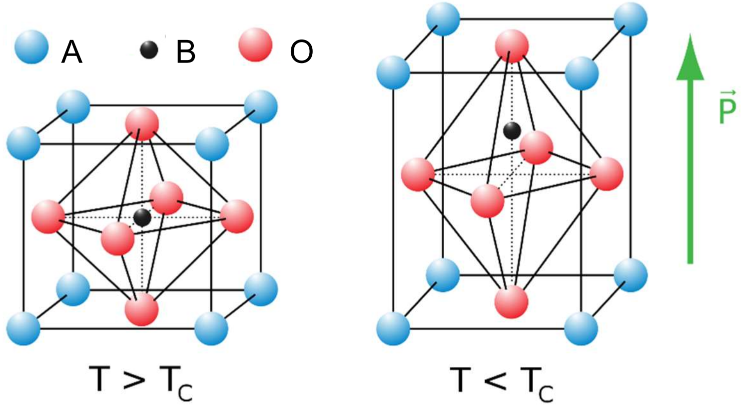

Figure 2-4 Perovskite structure of many commonly studied ferroelectric materials. The left depicts the crystal structure in the paraeletric phase and the right depicts the crystal structure in the ferroelectric phase.

2.4 Ferroelectric Poling

As discussed previously, domains and domain walls are formed to minimize the

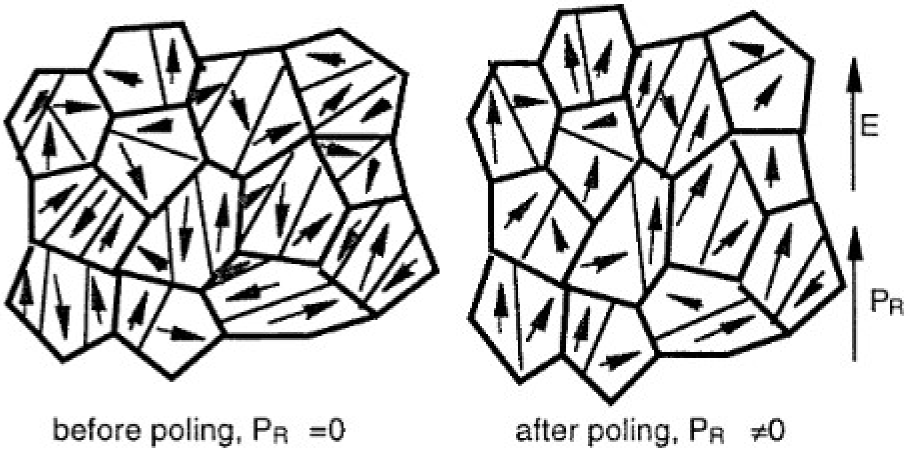

Figure 2-5 Schematic of domain poliarzation orientations within grains (a) before and (b) after poling.[3]

energy within the system during cooling from the paraelectric phase to the ferroelectric phase. These domains will initially have randomly distributed dipole directions, and will typically result in an almost net zero polarization. This cumulative effect renders the material non-polar and non-piezoelectric in the virgin state.[3] “Poling” the material through the application of an electric field essentially activates the ferroelectric phase. The dipole direction of the domains will switch to reorient with the applied field. In this process, the domains will change in size and the domain walls will move to accommodate. When the applied field is removed, some of the domains will reorient back to their original positions, while others will remain in this “poled” state, giving rise to the remanent polarization.

2.5 Intrinsic and Extrinsic Contributions

The functional response in ferroelectrics is highly dependent on the domain structure and defect landscape of the material. The domain wall movements induced by electric fields can be classified into two contributions: intrinsic or extrinsic.[3] Intrinsic contributions are smaller, reversible motions within the unit cell, i.e. domain wall vibration. Extrinsic contributions are larger, irreversible motions across the material, i.e. domain wall motion. Motion of all domain walls will influence polarization and dielectric responses in ferroelectric materials since only the polarization direction vector is changed. However, only the motion of non-180 domain walls influence the piezoelectric response due to the ferroelastically-active nature (Figure 2-6).[3,10] Notably, up to 40 to 80% of the dielectric and piezoelectric response in ferroelectric materials comes from the extrinsic contributions.[3]

In ideal polycrystalline, polydomain ferroelectric materials, the intrinsic and extrinsic both contribute to the real components of the dielectric and piezoelectric responses, while the extrinsic mechanisms can also contribute to the imaginary components, or the loss components, of the responses. Numerous studies have been conducted to separate these intrinsic and extrinsic contributions, including those involving temperature[11,12], excitation frequency[13–16], and aging time[17–19] dependence. However, these

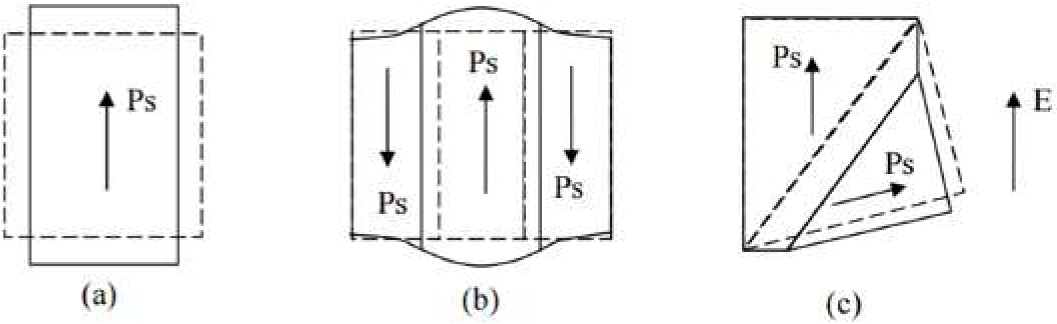

Figure 2-6 Schematic representation of (a) intrinsic contribution from a single domain, (b) extrinsic contribution to the dielectric response from 180° domain wall motion, and (c) extrinsic contributions to the dielectric and piezoelectric response from non-180° domain wall motion, all with application of an electric field.[10]

techniques are primarily qualitative, and thus do not provide a clear quantitative measure of the intrinsic and extrinsic contributions.

A method to quantify the intrinsic and extrinsic contributions involves studying the nonlinear field dependence of the dielectric and piezoelectric response with Rayleigh law analysis.[20] The Rayleigh law was initially developed to describe the behavior of ferromagnetics at low electric fields.[21] Further studies led to the demonstration of the motion of ferromagnetic walls between potential energy wells with application of electric field.[10] This was then correlated to defect concentrations in ferromagnetic materials.[22] The Rayleigh law has then been applied to describe the motion of domain walls in ferroelectric materials.

The dielectric permittivity-AC electric field plot can be divided into three main regions (Figure 2-7).[23] The first region, at low field, shows a constant dielectric permittivity. As the field increases the dielectric permittivity moves into a second region known as the Rayleigh region. Here the permittivity begins to increase linearly with the AC field. It is this region where the Rayleigh law analysis is used to quantify the intrinsic and extrinsic contributions of the material. At a certain E_{th} field, the permittivity begins to rapidly increase nonlinearly with the applied field, as the domains within the ferroelectric material begin to switch. In this region the Rayleigh law no longer applies.

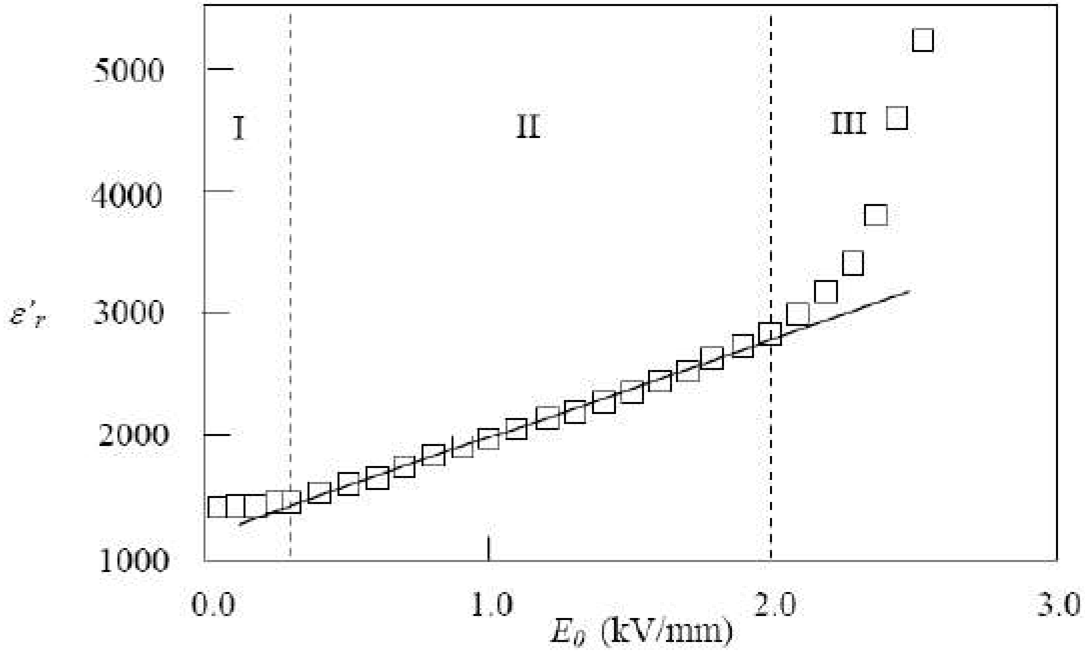

Figure 2-7 Schematic representation of the AC field dependence of the real dielectric permittivity in bulk Pb(Zr,Ti)O3 ceramics. The low field region with relatively constant dielectric permittivity, the Rayleigh region where the dielectric permittivity increases linearly with the electric field, and the high field region where a super-linear field-dependence of the dielectric permittivity if observed.[23]

For ferroelectrics, the Rayleigh law describes the hysteretic response of domain wall motion from one energy potential well to another. The Rayleigh law also assumes a random distribution of pinning centers which make up the domain wall energy profile. It describes the response in sub-switching conditions where the dielectric (Equation 1-2) and piezoelectric (Equation 1-3) coefficients depend linearly on the applied electric field's amplitude.

$$\varepsilon' = \varepsilon'_{init} + \alpha' E_o \qquad \text{1-2}$$

$$d = d_{init} + \alpha_d E_o \qquad \text{1-3}$$

The field-independent terms, ε'_{init} and d_{init}, represent the intrinsic responses related to the reversible domain wall motion and vibrations, and are labeled the reversible Rayleigh parameters. The constants α' and α_d represent the extrinsic responses related to the irreversible domain wall motion, and are labeled the irreversible Rayleigh parameters. The ratio of irreversible to reversible Rayleigh parameters is a quantitative measure of the extrinsic contributions to the dielectric and piezoelectric response. What ultimately determines the degree to which the domain walls can move are the defects present within the material. It is imperative to understand these defects and their role within the material, especially in the context of radiation exposure which can introduce new defects into the material system, as will be discussed in later sections of this chapter.

2.6 Ferroelectric Compositions

The ever increasing need for microelectronic devices with greater functionality and smaller footprints has led to the development of new ferroelectric thin films for various applications, including ferroelectric random access memory (FeRAM), multilayer ceramic capacitors (MLCC), and microelectromechanical systems (MEMS) devices. One of the most heavily studied materials for a multitude of these applications is the ferroelectric solid solution lead zirconate titanate (PZT) due to its large dielectric, ferroelectric, and piezoelectric properties and the tunability of its properties through processing variation.

The heightened functional response of PZT is largely due to the existence of a morphotropic phase boundary (MPB) in the $xPbZrO_3$–$(1\text{-}x)PbTiO_3$ system between the rhombohedral and tetragonal phase at x~0.52. As shown in Figure 2-8, fabrication of PZT near this morphotropic phase boundary leads to maximal functional response from the material shift between rhombohedral and tetragonal distortion in the perovskite unit cell.[1,24] The result of heightened functional response from material fabrication at or near the MPB has held true for a multitude of solid solution systems, including those used in this study as will be discussed later in this chapter. First, defects and radiation interactions with materials will be discussed to illustrate the need for new material systems for these applications.

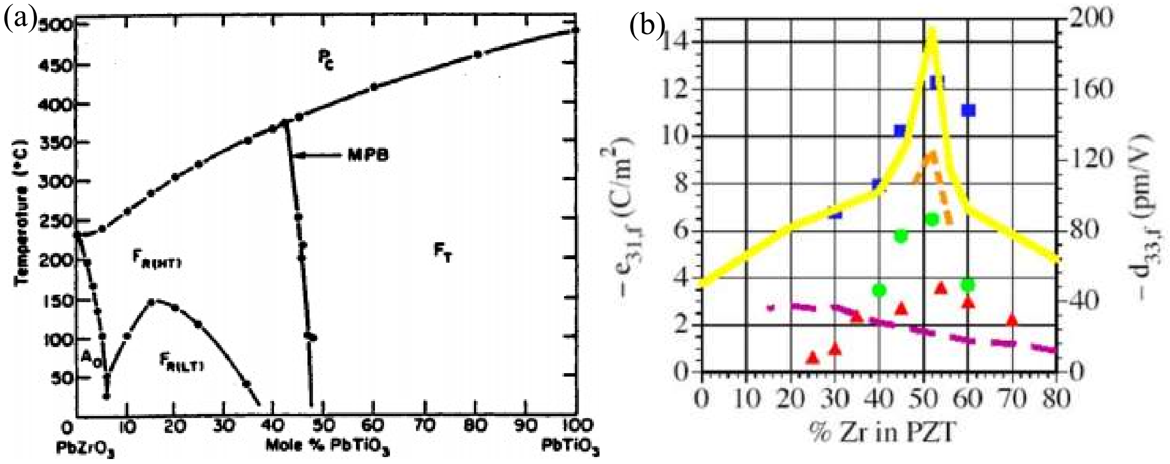

Figure 2-8 (a) Phase diagram of PZT, indicating the morphotropic phase boundary between the rhombohedral and tetragonal phases. (b) Dependence of electromechanical response of PZT with respect to composition, showing heightened response at the morphotropic phase boundary.[1,24]

2.7 Defects in Ferroelectric Thin Films

Crystallographic defects are present in almost all solid materials. The various point, line, planar, and bulk defects within a solid will greatly determine the material's properties, and these defects are often purposefully engineered to produce desirable properties to fit specific applications. In polycrystalline ferroelectric materials, defect-defect interactions between defects such as domain walls, grain boundaries, and point defects will greatly determine the dielectric, polarization, and piezoelectric responses. Most commonly discussed defects in ferroelectric materials include point defects, such as atomic vacancies (oxygen vacancies or Pb-vacancies in lead-based materials) or atomic substitutions (acceptor ion at the B-site), and the defect dipoles which can form between cationic defects and oxygen vacancies. Pinning and unpinning of domain walls to and from other defects via application of electric field contributes to the dielectric and piezoelectric response.[3]

However, the accumulation of higher concentrations of defects or the development of more strongly pinned defects will ultimately prevent the motion of domain walls and drastically degrade the functional response. Additionally, the defect landscape of the material can change through electrical loading (fatigue) or over time even in absence of loading (aging).[3,25]

Ferroelectric fatigue is defined as the loss of the spontaneous, switchable polarization with an increasing number of bipolar switching cycles. Defect concentrations, electrode material, temperature, electric field strength, surface treatment, porosity, and grain size have all been shown to contribute to ferroelectric fatigue. Numerous studies have been conducted on the interaction of mobile oxygen vacancies, both within the ferroelectric material itself and at interfacial regions (e.g. grain boundaries, layer interfaces, electrode interfaces, etc.), and their effects on ferroelectric fatigue.[3,25–31] The mobilization and accumulation of the oxygen vacancies towards the ferroelectric-electrode interface can lead to the screening of the ferroelectric film from the applied electric field, subsequently reducing the polarization switching. These oxygen vacancies may also increase pinning of domain walls, further reducing the response of the material. Other than oxygen vacancies, electronic defects can also decrease domain wall motion and suppress polarization. Free electronic charge carriers attracted to the domain walls can become trapped in the domain walls and pin them. These charge carriers can be introduced into the material through electric field cycling at the electrodes, during fabrication, and with exposure to radiation. Some of these pinning defects can be overcome by an application of an electric field. It is also important to note that these defects may also become more mobile or recombine with other defects and decrease pinning of domain walls, leading to increased response.

Ferroelectric aging describes the pinching of the hysteresis loop overtime at low fields. It is the reorientation of defects within the material which typically causes this aging behavior. During fabrication of ferroelectric materials, randomly distributed elastic and/or electronic defects are formed within domains. Over time, these defects will reorient into more energetically favored orientations, thus increasing the energy necessary to switch their polarization. Additionally, the existence of residual mechanical stresses or uncompensated electrical charges from fabrication can lead to accumulation of defects at and pinning of domain walls over time. Finally, space charges often accumulate at regions such as grain boundaries due to phase separation at these locations. Uncompensated space charges can lead to a preferential bias within the grain and stabilize local domains, further

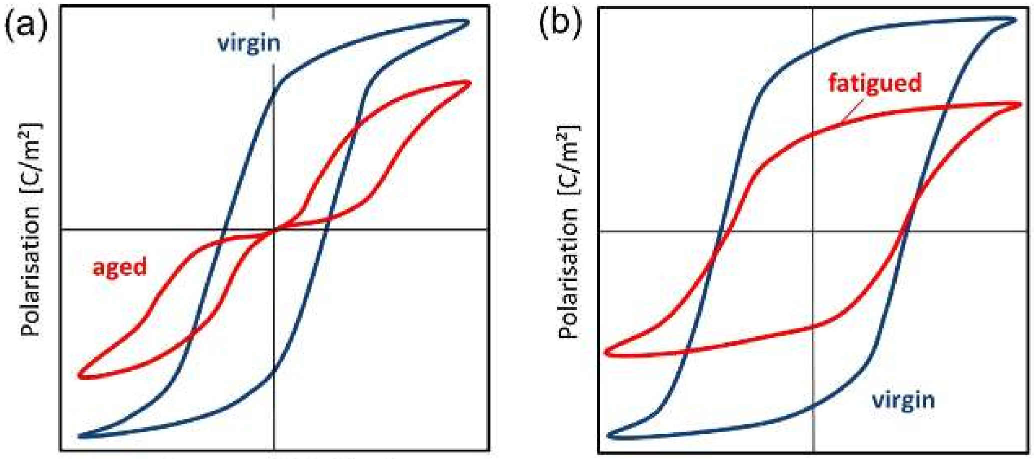

Figure 2-9 (a) Characteristic pinching of ferroelectric hysteresis loop due to aging effects, as well as degradation of polarization response. (b) Degradation of polarization response in ferroelectric materials due to fatigue.[25]

reducing domain wall motion. These effects can also lead to an overall internal bias within the material, further degrading the response of the film to an external electric field.

Terms used to describe effects due to ferroelectric fatigue and aging, especially in memory device applications, include endurance, retention, and imprint. Endurance and retention are the resistance of the material to ferroelectric fatigue and aging, respectively. Imprint is often used to describe a preferential bias found within the material.

2.8 Radiation-Material Interactions

The interaction between radiation exposure and functional materials is imperative to understanding how devices will behave when placed in high radiative environments, such as aerospace equipment, medical physics tools, and nuclear monitoring systems. Radiation damage in materials can occur in two events: ionization and displacement. Ionization events involve the interaction of radiation particles with electrons in the material. The excitation of electrons can lead to electron-hole pair generation, and potentially lead to the trapping of electrons at defect centers within the material.[32] Radiation particles with sufficient enough energies will interact with atomic nuclei, leading to displacement events and the formation of Frenkel defects.[33] These high energy interactions can also lead to cascade events, creating additional defects within the material which have the potential to cluster or even amorphize the material.[34] In general, low-energy photons such as X-rays, gamma rays, and electrons only have sufficient enough energy to cause ionization damage. Higher-energy particles such as protons, neutrons, and heavy ions can cause both ionization and displacement events. Their greater mass and reduced velocities also increases their interaction time within the material, potentially leading to greater damage than low-energy photons at similar doses.

2.8.1 Radiation-Ferroelectric Interactions

In ferroelectric materials, radiation exposure has the potential to drastically change the defect landscape through introduction of new defects or modification of pre-existing defects. Changes in the defect landscape will lead to changes in the domain wall motion, oftentimes suppressing domain wall motion and subsequently reducing functional response. Previous studies on ferroelectric thin films have shown degradation in dielectric and polarization responses upon radiation exposure.[35–39] In PZT thin films, some of the earliest works showed that the pinching characteristics in the polarization loop after x-ray or gamma irradiation was greatly influenced by the bias applied before irradiation.[40–42] The results suggested that the radiation-induced degradation was due to charge trapping near the electrodes, heavily influenced by the direction in which the samples were biased prior to irradiation. Furthermore, samples which were biased during radiation exposure also showed less radiation damage than those that were not biased, in agreement that radiation-induced degradation is primarily caused by the accumulation of trapped charges at interfaces within the material.[41] Studies on neutron irradiation PZT materials also showed decreases in polarization response, pinching of hysteresis loops, decreases in capacitance and electromechanical coupling, as well as decreases in current density, pointed towards the increase of trapped charges within the materials.[43–46] The degradation in functional response was found to be due to suppression of domain wall motion and subsequently the extrinsic contributions to functional response by radiation-induced defects such as defect-dipoles and other charged defects which can pin domain walls.[47] In addition to the degradation in functional response, Miclea *et al.* noted a change in microstructure, pointing towards an increase in unit cell volume as well as a decrease in lattice aspect ratio (c/a). Evidence of crystallographic changes in PZT thin films were also found after neutron radiation. Henriques et al. in agreement with those found in Miclea et al. They detected increased Pb and O vacancies, and even detected evidence of phase separation in the PZT films.[48]

Another interesting phenomenon found in a few studies was the increase in ferroelectric properties after gamma irradiation. Gao *et al.* showed that with their Pt/PZT/Pt samples, the polarization properties actually increased.[35] Brewer et al. also showed evidence of increasing piezoelectric properties in PZT thin films.[49] While this phenomenon is still not well understood, it is possible that the radiation-induced defects act to heal the pre-existing defects within the materials, allowing for greater domain wall motion and subsequently enhanced functional response.

Recent studies continue to show degradation to the functional response of PZT thin films after exposure to X-rays, protons, and gamma irradiation.[50,51] While ferroelectric thin films such as PZT have considerable radiation tolerance compared to semiconductor devices, total ionization dose (TID) studies conducted by Brewer *et al.* have shown significant degradation in response at doses at or over 5 Mrad(Si).[49] Many studies have been conducted to improve the radiation tolerance of PZT films, including optimizing microstructure and material stack to eliminate interfacial regions which may act as collection areas for radiation-induced defects (e.g. grain boundaries or use of metal-oxide electrodes).[26,49,52] The most successful approach to increase PZT's radiation hardness was through Mn-doping.[49] The creation of $Mn''_{Zr/Ti} - V_O^{\cdot\cdot}$ defect dipoles results from the increase in oxygen vacancies in the film which are stabilized by the acceptor ion, thereby preventing radiation-induced electrons from mobilizing these oxygen vacancies. However in doing so, the virgin dielectric and piezoelectric properties of the Mn-doped PZT were significantly lower than undoped PZT. Challenges with optimization of commonly known ferroelectric materials has led to a need for new material systems with equivalent or greater properties as well as greater radiation tolerance that PZT. In this work, two material systems will be studied as alternative materials to PZT in both MEMS devices and memory access devices.

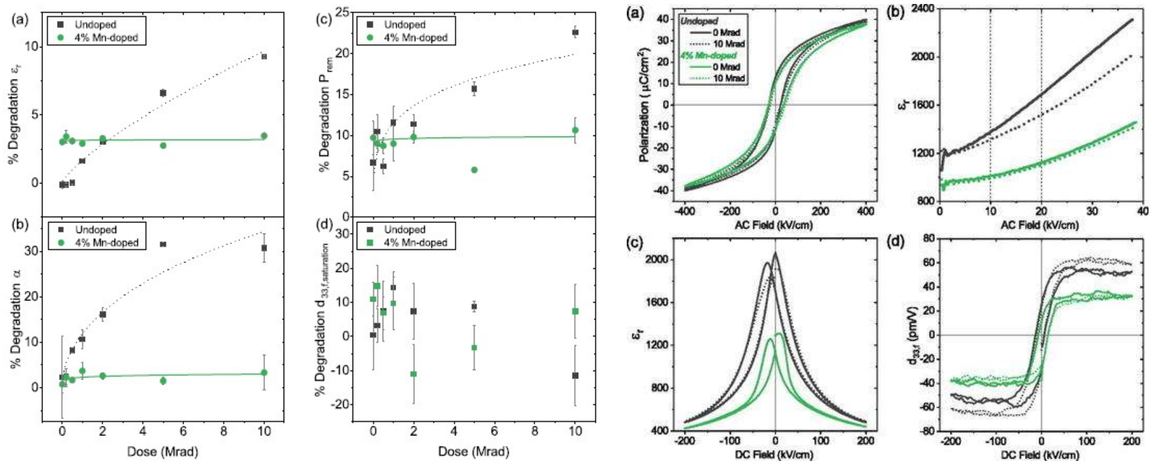

Figure 2-10 Left (a-d) Trends in TID study of undoped PZT and Mn-doped PZT showing greater radiation hardness in Mn-doped PZT. Right (a-d) Polarization, nonlinear permittivity, permittivity-field, and piezoelectric curves showing degraded response in Mn-doped PZT compared to undoped PZT.[49]

2.9 Pb(Mg$_{1/3}$Nb$_{2/3}$)O$_3$-PbTiO$_3$

PMN-PT is a relaxor-ferroelectric solid solution between two end members, lead magnesium niobate ($Pb(Mg_{1/3}Nb_{2/3})O_3$, PMN) which is anti-ferroelectric, and lead titanate (PbTiO3) which is ferroelectric. While the morphotropic phase boundary between the tetragonal and rhombohedral phases exists has been thought to exist at x~0.33, other phases have since been observed in this region as well (Figure 2-11).[3,53] In bulk single crystal form, it can exhibit electromechanical response three times greater than that of bulk PZT in [001] cut and poled crystals fabricated near the morphotropic phase boundary (0.7PMN-0.3PT).[54] Since polycrystalline thin films are influenced by far more defects than single crystalline samples, it is crucial to also fabricate (001)-oriented films in order to maximize the functional response.

Table 2-1 Piezoelectric properties for selected PT-solid solutions.[54]

Form	Materials	d_{33} (pm/V)
Ceramic (poly-crystalline)	PZT (53/47)	220
	0.7PMN-0.3PT	670
Single Crystal	70PMN-30PT	~1500
	0.58PSN-0.42PT	450
	0.5PNN-0.5PZT(35/65)	370

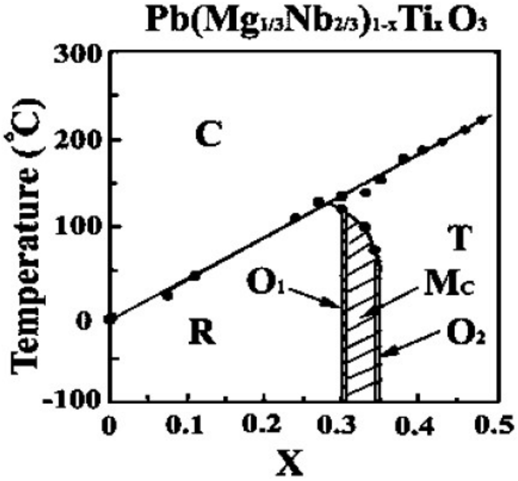

Figure 2-11 Phase diagram of (1-x)Pb($Mg_{1/3}Nb_{2/3}$)O_3-xPbTiO_3.[53]

While the specific mechanisms involved in the heightened functional response of relaxor-ferroelectrics are not well understood, properties such as the existence of chemical and polar nanoregions as well as increased domain wall anisotropy are suspected to be contributors.[55] These same properties may also lead to increased radiation tolerance: First, PMN-PT has increased chemical heterogeneity with respect to PZT, and this inherent disorder on B-site cations may result in increased resiliency to displacement effects on the functional response of the material. Second, presence of random fields due to the B-site cations' multi-valence states can offer multiple sites for annihilation of electrons, i.e. local charge variations are inherently embedded in virgin material. Third, the high domain wall concentration and mobility of PMN-PT may be partially retained, even at increased number of defects generated through irradiation.

2.9.1 PMN-PT Processing Challenges

While PMN-PT exhibits properties which are extremely attractive for next generation of radiation-tolerant MEMS devices, it is also notoriously difficult to process reliably. The higher processing temperatures necessary to crystallize niobates leads to much higher Pb losses because of its high volatility. Hence processing PMN-PT thin films is challenging, including (1) intensifying differences in the coefficient of thermal expansion between the material and the substrate which thus leads to cracking in the films, (2) creation of pores due to volatization of lead oxide pockets, and (3) secondary phase

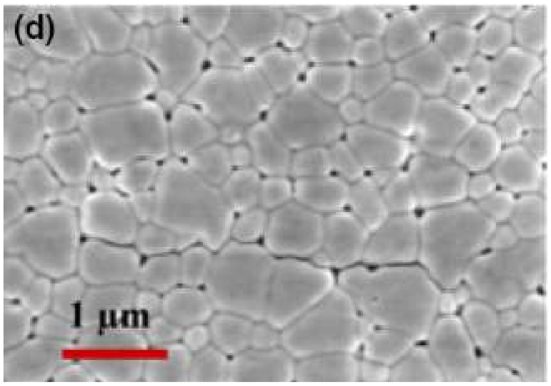

Figure 2-12 Scanning electron microscopy (SEM) image of PMN-PT thin film surface. Porosity and cracks between grains can be observed.[56]

creation due to local lead deficiency.[56] These issues become exacerbated when the films increase with thickness, showing extreme signs of cracking along grain boundaries with film thicknesses above 600 μm. Although the high electromechanical response could warrant the utilization of thinner films, the standard for MEMS devices is approximately 1000-2000 μm in thickness, so adapting the material to the current devices is difficult. While porosity has been shown to improve electromechanical response to some extent, air pockets within electromechanical devices will often lead to device failure.[57] Inconsistencies with processing makes it difficult to reproduce films with the same characteristics, even within the same research groups.

Chemical solution deposition (CSD) is the ideal method for processing ferroelectric thin films because of its relatively low cost, simple processing procedure, and ability to scale production of films onto Si substrates. Deposition of ferroelectric oxide thin films via CSD involves the following steps: (1) synthesis of the precursor solution; (2) deposition of the precursor solution onto the substrate by spin-coating or dip-coating; (3) low temperature heat treatment (200-400 °C) for removal of excess solvent and other organic components; and (4) high temperature heat treatment (600-850 °C) to crystallize the material. Several parameters need to be optimized within this process including the precursor solution molarity, the excess Pb content of the precursor solution, the spin coating speed and duration, the temperature and duration of the pyrolysis step or steps, the temperature and duration of the crystallization step, possible overcoat or undercoat layers to compensate for Pb diffusion or loss, and seed layers for optimal film orientation. In addition to these parameters, other factors such as hydration level of the solution, ambient humidity, and chemistry during the crystallization process may also influence the microstructure and subsequent functional characteristics of the PMN-PT thin films.

(001)-oriented PZT thin films have been reliably obtained by utilizing either an extremely thin PZT seed layer with high Pb excess content, or alternatively $PbTiO_3$ or PbO_x, ~20 nm in thickness, directly onto a (111)-oriented platinum surface. However, obtaining (001)-oriented PMN-PT is much more difficult. Although various studies have used seed layers such as PbO, PTO, and even PZT with various Pb excess concentrations to successfully induce (001)-orientation, this orientation is not guaranteed.

To date, no reliable processing recipe has been determined for crack-free, pore-free PMN-PT thin films, and studies on PMN-PT thin films within the past two decades have shown a wide range of processing parameters (Table 2-2).[56,58–61] Even parameters published by the same author within the last five years have continuously changed, illustrating the difficulties in optimizing and reproducing consistent PMN-PT thin films. Notable in the evolution of processing parameters is the use of higher crystallization temperatures. In Park *et al.* and Bastani *et al.,* even with the two different processing parameters, it was confirmed that the higher crystallization temperatures led to higher quality films. Both an increase in grain size and density were found in films with crystallization temperatures at 800 °C, allowing for greater functional response from these films. However, it was also found that possible Pb-deficiencies due to the high crystallization temperature led to secondary phases in the films, overall decreasing the quality of the films. To combat this issue, excess Pb in solution as well as PbO overcoats and/or undercoats are used, however varying results are found in the amount of excess Pb or in the molarity of the PbO solutions that is necessary to alleviate the issue of secondary phases. Furthermore, different parameters for the addition of overcoats and/or undercoats of either PbO or PTO layers have been used with varying results in alleviating porosity or cracking. Thus, the initial portion of this work concentrates on exploration of processing parameters to control thin film orientation, grain morphology, porosity, secondary phases, and functional response before moving forward with radiation studies.

Table 2-2 Processing parameters used in various studies on PMN-PT thin films

Spincoating	Drying	Pyrolysis	Crystallization	excess Pb, %	Ref.
2500 rpm/30 s	N/A	360 °C/3 min	650-800 °C/1 min	15	56
3000 rpm/30 s	N/A	360 °C/1-3 min	750-850 °C/2 min every four layers	15	58
2500 rpm/45 s	250C/2 min	430 °C/5 min	Layer 1: 740 °C/1 min Layer 2: 700 °C/1 min	10	59
N/A	250C/1 min	400 °C/5 min	Layer 1: 740 °C/1 min Layer 2: 720 °C/1 min	10-20	60
3000 rpm/45 s	300C/2 min	410 °C/5 min	740 °C/1 min	10	61

2.10 $Hf_{0.5}Zr_{0.5}O_2$

Nonvolatile memories use ferroelectric materials for low power, high density future memory technologies. However, the utilization of typical ferroelectrics in these devices also calls for buffer layers, (lead zirconate titanate, strontium bismuth tantalate) to protect from hydrogen damage during back end of line (BEOL) processing.[62,63] Thus, research interests have shifted towards new material systems which do not require buffer layers, including hafnia-based ferroelectric thin films.

Ferroelectricity in hafnia-based films was first discovered in SiO_2-doped HfO_2 thin films with strong orthorhombic phase.[64] However, a disadvantage to this material is the high crystallization temperatures required to achieve the ferroelectric phase. Alternatively, zirconium oxide has already been utilized in microelectronic devices as high-k dielectrics for dynamic random access memory and high-k metal gate applications, making it a possible dopant for HfO_2 based materials. Processing of HfO_2-ZrO_2 (HZO) systems has thus proven to be more compatible with device manufacturing. Since these films are fabricated via atomic layer deposition (ALD), they can be scaled down to nanometers in size, from planar capacitors to three-dimensional capacitors, while maintaining low leakage current and electrical breakdown, attributed to the relatively large bandgap in comparison to traditional ferroelectric materials.

Unlike the ferroelectric materials that have been discussed thus far, these materials have a fluorite structure, where the ferroelectricity appears in the orthorhombic phase. The orthorhombic phase is induced by crystallizing the material under mechanical encapsulation (Figure 2-13).[64] $Hf_xZr_{(1-x)}O_2$ exhibits the highest ferroelectric properties at x~0.5, where a morphotropic phase boundary exists between the tetragonal (t-phase) to orthorhombic (o-phase) phase.[65–69]

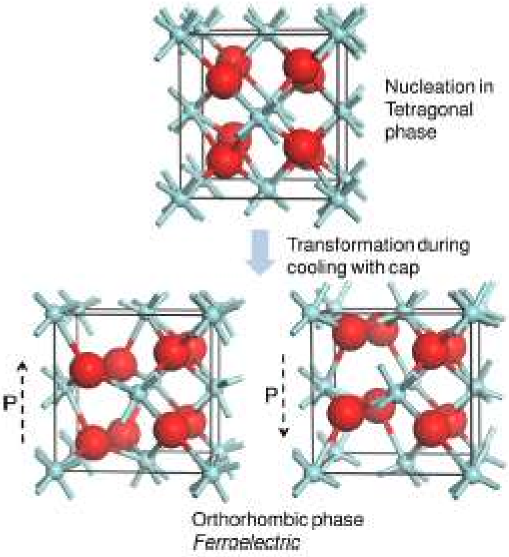

Figure 2-13 Formation of ferroelectric orthorhombic phase in hafnia-based oxides.[64]

The mechanisms behind the ferroelectricity of these films are not well understood. Typically, in the pristine state the films will exhibit anti-ferroelectric behavior. The films undergo a “wake-up” effect with electrical cycling, which induces the ferroelectric phase (Figure 2-14).[70] Further cycling will result in slight increases in polarization response before suffering from fatigue. Some proposed mechanisms include the migration of oxygen vacancies under a few MV/cm, leading to the redistribution of oxygen vacancies to enable ferroelectricity.[71] STEM imaging has shown the shift in the bulk crystal structure from monoclinic to orthorhombic phase with increasing cycles, along with a decrease in a defect-rich tetragonal phase near the electrodes.[72] Others point out that further cycling can lead to electron trapping in deep states of oxygen vacancies, pinning domains and causing both imprint and fatigue.[73]

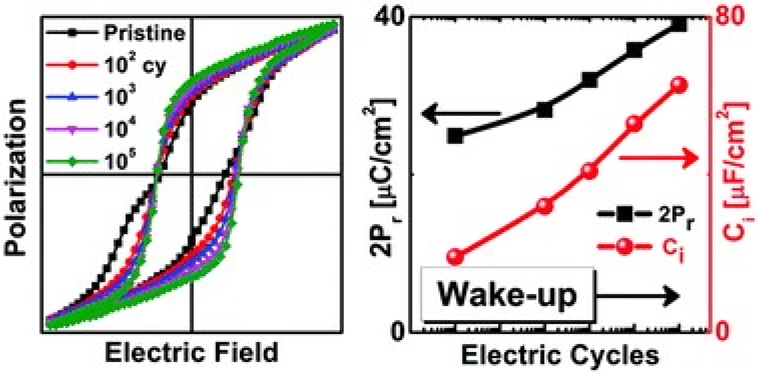

Figure 2-14 Wake-up effect in HZO thin films with increasing cycles.[70]

Despite the unknowns surrounding the origins of ferroelectricity in hafnia-based thin films, extensive research has continued to optimize fabrication techniques for ferroelectric Zr-doped HfO_2 films. A majority of research has focused on thermal atomic layer deposition (THALD), which allows for post-annealing temperatures as low as 400 °C to induce ferroelectricity in the films.[74] However, these films contain a strong wake-up effect, requiring cycling in order to induce the ferroelectric phase within the material.[75] This wake-up effect has been observed in prior studies on SiO_2-doped films as well, as Zhou et al. attributed the wake-up effect originating from the elimination of an internal field near the ferroelectric/electrode interface through redistribution of oxygen vacancies in the Si-doped HfO_2 films.[76] A study by Martin et al. showed the transition from m-phase to o-phase during electric field cycling through TEM analysis in Si-doped HfO_2 thin films.[77] A new and improved process involving plasma-enhanced atomic layer deposition has led to ferroelectric Zr-doped HfO_2 films processed with post-annealing temperatures as low as 300 °C, already induced into the o-phase even before cycling.[78] It is suspected that PEALD has higher oxidizing power than THALD, and leads to a redistribution of oxygen vacancies through the thickness of the material to induce the o-phase. These low temperatures enable fabrication of next generation devices through achieving conformal coverage on complicated three-dimensional structures with well-controlled thin films.

2.10.1 Radiation effects on ferroelectric HZO films

The few studies that have been conducted on the radiation tolerance of HfO_2-based ferroelectric thin films have shown promising results in the retention of remanent polarization.[31,79] $Hf0_{.5}Zr_{0.5}O_2$ thin films deposited on flexible substrates showed a degradation of ~6% in remanent polarization after gamma-radiation dose of 1 Mrad(Si).[80] A more recent study on HZO thin films on Si substrates irradiated by gamma irradiation doses up to 10 Mrad(Si) showed significant radiation tolerance, with a decrease in remanent polarization of only 5%.[81] However, these studies were only conducted on HZO thin films processed via THALD. In this work, PEALD and THALD ferroelectric HZO thin films are directly compared to determine the differences in their radiation tolerance, and also illuminate material characteristics which may lead to greater ferroelectricity in HZO thin films.

CHAPTER 3. EXPERIMENTAL PROCEDURES

This chapter details the processing and characterization procedure of alternative ferroelectric oxide thin films studied in this work. This includes lead magnesium niobate-lead titanate, $0.7Pb(Mg_{1/3}Nb_{2/3})O_3$-$0.3PbTiO_3$ (PMN-PT), and hafnia-zirconia, $Hf_{0.5}Zr_{0.5}O_2$ (HZO) thin films. In this work, PMN-PT thin films were fabricated on platinized silicon wafers via chemical solution deposition (CSD). The hafnia-zirconia films provided for this study were fabricated onto silicon wafers via atomic layer deposition (ALD). Characterization of the film's properties including film thickness, crystallographic phase, microstructure, and dielectric, polarization, and piezoelectric responses will be discussed.

3.1 Chemical Solution Deposition of PMN-PT Thin Films

Chemical solution deposition has many distinct advantages over other fabrication techniques such as low cost, ease of access of precursor chemicals, good uniformity over a large area, as well as strong compositional control.[82,83]

The fabrication of ferroelectric oxide films via CSD is a multi-step process involving: (1) synthesis of a precursor solution; (2) deposition onto the substrate; (3) low temperature heat treatment; and (4) high temperature heat treatment (Figure 3-1).[84] Step (3) is typically referred to as "pyrolysis", due to it resulting in thermal (pyro) decomposition (lysis) and largely the removal of organic components in the film. As will be discussed later, this low temperature heat treatment step may also include a "drying" step, a substantially lower temperature to help improve removal of organics. Control of deposition and heat treatment conditions is necessary to obtain high quality thin films (orientation, density, grain morphology) as will be discussed in detail in the next chapter.

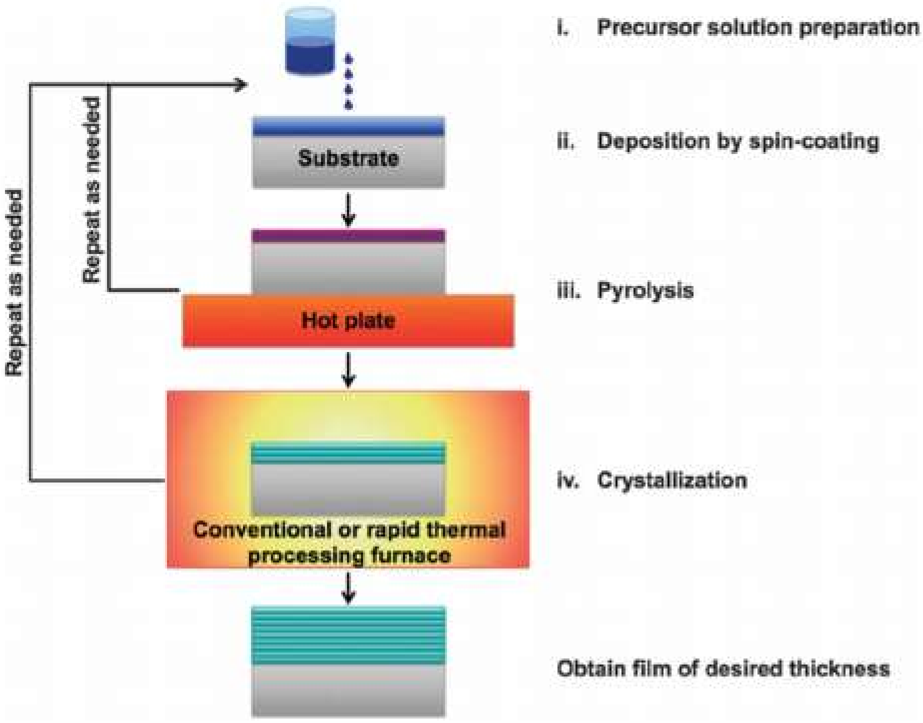

Figure 3-1 Schematic of basic steps of chemical solution deposition of thin films. For PMN-PT, an additional drying step can be added before pyrolysis.[84]

3.1.1 Precursor Solution Processing

A 2-methoxyethanol route was used for synthesizing the precursor solution for the PMN-PT solutions under dry Ar environment, adapted from Park et al. and Bastani et al.[56,58] Magnesium ethoxide is refluxed at 130 °C for 24 hours. Niobium ethoxide and titanium isopropoxide are then added to the magnesium ethoxide solution and refluxed at 120 °C for 3 hours. Meanwhile, lead acetate trihydrate is separately distilled at 120 °C for 3 hours. Afterwards both the Mg/Nb/Ti and the Pb precursor solutions are combined and refluxed for 120 °C for 3 hours, then distilled to the final volume amount. The PMN-PT solutions were prepared with concentrations of 0.3M and 0.4M, and with excess Pb content from 10 to 40%.

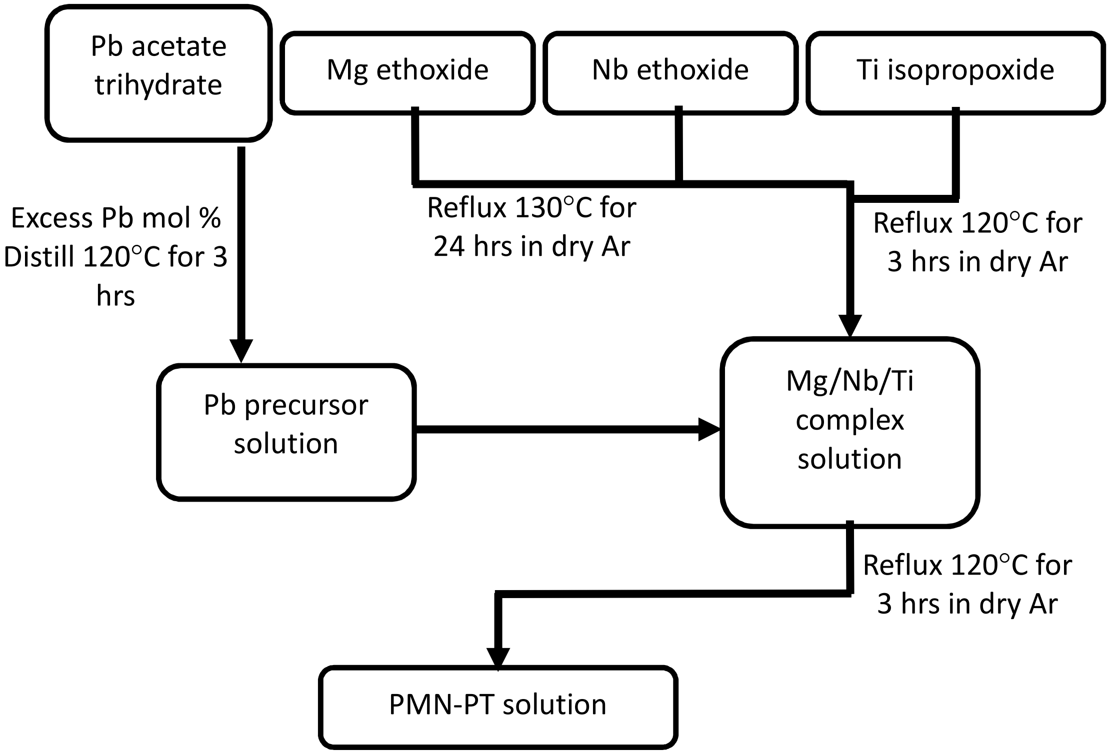

Figure 3-2 Route for synthesis of PMN-PT precursor solution via the 2-methoxyethanol route.

Similar 2-MOE methods were used to prepare precursor solutions for seed layers. For the PbO precursor solution, lead acetate trihydrate was distilled at 120 °C for 30 minutes then mixed into 2-MOE at 120 °C until dissolved. 0.8M PbO stock solutions were prepared, and diluted using 2-MOE for the desired final concentration. For the $PbTiO_3$ precursor solutions prepared at Georgia Tech, lead acetate trihydrate was distilled at 120 °C for 30 minutes while titanium isopropoxide was separately refluxed at 120 °C for 30 minutes. The two solutions were then combined and mixed 120 °C for 30 minutes, then distilled to the final volume. The PTO solutions were prepared with a concentration of 0.2M, and with excess Pb content from 5 to 30%.

3.1.2 Substrate/Bottom Electrode Preparation

PMN-PT thin films were deposited onto platinized Si wafers provided by the US Army Research Laboratory (ARL) with 100 nm Pt // 35 TiO_2 // 750-2000 nm SiO_2 // Si. TiO_2 is used as an adhesive layer between the Si wafer and the Pt bottom electrode. Pt is commonly used as a bottom electrode as it is able to withstand the crystallization temperatures necessary for ferroelectric thin film fabrication, and can also facilitate in (001)-orientation of seed layers and subsequent ferroelectric layers.

Some tests were also conducted on silicon wafers platinized at Georgia Tech. For these wafers, the Unifilm Sputterer was used to sputter on 20 nm TiO_2 at a rate of 100 Å/min followed by 80 nm Pt at a rate of 200 Å/min without break of vacuum.

3.1.3 Thin Film Deposition

Platinized silicon wafers prepared in-house or provided by ARL were used in this work, as described in the previous section. Wafers were snapped into approximately 1 inch by 1 inch squares using a diamond scribe. Precursor solutions were loaded into a ~5 mL syringe and bubbles were removed from the syringe. The solution then passed through a 0.1 μm PTFE filter and needle before being dispensed to the corner of the wafer and allowing the solution to slowly propagate across the wafer, being careful to prevent formation of bubbles. The wafers were previously positioned onto the spin coater (Laurell

Technologies, or Ossila). The chip was then spun at speeds dependent on processing recipe with ramp rate of approximately 500 rpm/s. With PMN-PT solutions of 0.4M concentration, this process results in layer thicknesses of 50 - 60 nm. Drying and pyrolysis steps involved placing the as-deposited films onto hot plates set at the desired temperatures. The samples were then crystallized in a Rapid Thermal Annealer (RTA) at the desired temperatures and durations, with a heating rate of 60 °C/s. Cooling starts by shut off of the radiation lamps and the chamber is allowed to cool without further control.

For PTO seed layers, 0.2M solutions were deposited and spun at 3000 rpm for 30 seconds. The as-deposited films were then pyrolyzed at 400 °C for 1 minute, and

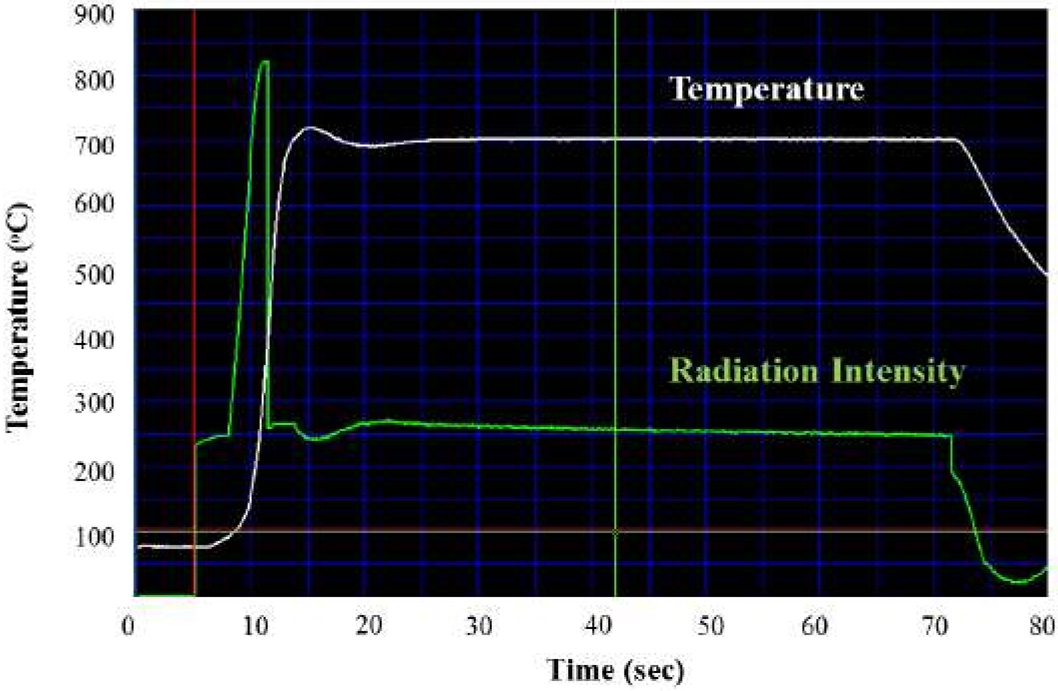

Figure 3-3 Temperature profile of rapid thermal annealer for crystallization of ferroelectric thin films. The white line profiles the temperature of the carrier wafer over time. The green line profiles the intensity of the radiation lamps used to increase the temperature in the chamber.

crystallized at 700 °C for 1 minute. For PbO seed layers, 0.08M or 0.02M solutions were deposited and spun at 4000 rpm for 30 seconds. The films were then dried at 400 °C for 10 minutes, and subsequent layers of PMN-PT were deposited on top before annealing according to the PMN-PT recipe used.

3.1.4 Top/bottom electrode contacts

Pt top electrodes were deposited via lift-off on PMN-PT thin films for macroscopic dielectric, ferroelectric, and piezoelectric characterization. NR9-1500PY negative photoresist was spun onto the film at 2000 rpm for 40 seconds with a ramp time of 2 seconds (SCS G3 spin coater), and baked on a hot plate at 150 °C for 1 minute. The photoresist was then covered with a light-field mask consisting of 100 μm, 500 μm, and 1 mm diameter circular electrodes in a grid pattern, and exposed to Ultra violet light (365 nm) using a Karl Suss MA6 mask aligner. The exposure time was calculated to result in a dose of 300 mJ/cm^2 using the formula $\frac{dos}{intensity} = time$. The film was then post-exposure baked at 100 °C for 1 minute on a hotplate. The resist was developed using RD6 resist developer before rinsing with deionized water. Approximately 80 nm of Pt was sputter-deposited with the Unifilm Sputterer at a rate of 200 Å/min. The samples were then submerged in acetone to remove the remaining photoresist and excess Pt in an ultrasonic bath (VWR).

Bottom electrodes were achieved in one of three ways: etching, Pt sputtering, or silver paste contact. In etching, a corner of the sample is etched with alternating buffered oxide etch (BOE), a 1:6 ratio of 49% HF buffered with ammonium fluoride, and HCl. A small piece of Kapton polyimide adhesive tape is laid over the corner to prevent the etchants from reaching the center of the material. A small cleanroom swab is used to apply a small amount of BOE to the corner, rubbing the ferroelectric material to remove it. Then a small amount of HCl is used, and the two etchants are continually alternated until the bottom electrode is exposed. This is the preferred method to reach the bottom electrode, as this also enables measurement of the film thickness using profilometry, as will be discussed later in this section.

In Pt sputtering, at the step before sputtering Pt for the top electrodes, a small amount of acetone is dipped onto a cleanroom swab, and a corner of photoresist is removed. The corner is then scratched with a diamond scribe to reach the bottom electrode, and brushed with air to remove particles. The sample is then sputtered with Pt as before, creating a top contact with the bottom electrode at the exposed corner.

In silver paste contact, after top electrode processing, a corner of the ferroelectric thin film is scratched with a diamond scribe, and silver paste is applied to the corner. This method is specifically used to create a bottom electrode contact in the HZO thin films.

3.2 Microstructural Characterization

3.2.1 X-Ray Diffraction

X-ray diffraction is a rapid, non-destructive analysis technique used for phase identification of crystalline materials, and can quantify unit cell dimensions and material strain. A monochromatic x-ray beam is directed onto the sample and scanned over several incident angles so that diffraction occurs at some specific angles. In θ-2θ scans, the diffracted beam intensity is collected at a position twice the incident beam. The Bragg condition describes the angles in which high intensity peaks will result, corresponding to specific crystallographic planes (Figure 3-4[85]). The position of the peaks collected represent the incident angle corresponding to a specific family of atomic planes in the sampled crystal. Bragg's law can be used to determine the interatomic spacing based on the x-ray wavelength and angle of the diffracted beam:

$$n\lambda = 2dsin\theta \qquad 3\text{-}1$$

where n is an integer, λ is the wavelength of the incident beam, d is the interplanar spacing, and θ is the angle of incidence.

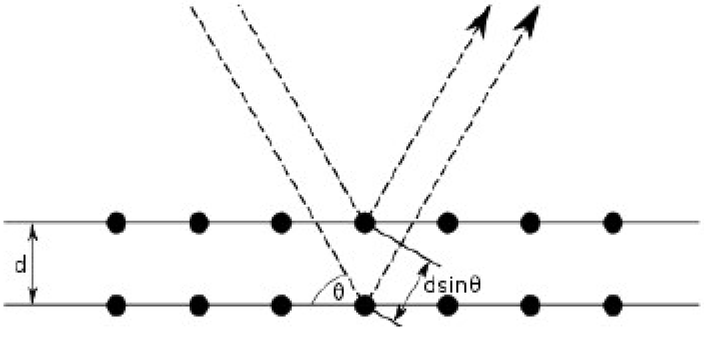

Figure 3-4 Schematic representation of Bragg diffraction with the lattice of an arbitrary material. Incident X-rays are scattered when in contact with atoms, and the diffracted rays are collected and counted for plotting and later phase indentification. Image ref. [85].

Standard θ-2θ scans with x-ray diffraction, XRD, were performed to identify crystallographic phase and texture of the films. A PANalytical Alpha-1 with Cu-Kα radiation was used. The x-ray generator was set at 45 kV and 40 mA. The PMN-PT films were scanned in 2θ from 20 to 70 dgrees, with a step size of 0.02° at a rate of 10 s/deg. The incident beam optics were a 10 mm mask and anti-scatter slit fixed at 1°. The diffractive beam optics were a 5.5 mm antiscatter slit, and 0.04 radian soller slits were used to control lateral divergence.

Lotgering factor was calculated to determine the degree of texture in the films.[86,87] Measured peak intensities are compared to powder diffraction data from corresponding PDF cards, as shown in Table 3-1.

Table 3-1 Powder diffraction file numbers used for XRD scan analysis (from ICDD PDF-4)

Material	PDF #
0.7Pb(Mg1/3Nb2/3)O3-0.3PbTiO3	01-076-9082
PbTiO3	00-040-0099
Pt	01-087-0640

Lotgering factor was calculated for (001)-orientation using the following equation:

$$LF = \frac{P_{LF} - P_{LF,0}}{1 - P_{LF,0}} \qquad 3\text{-}2$$

where

$$P_{LF} = \frac{I_{(100)} + I_{(200)}}{\sum I_{(hkl)}} \qquad 3\text{-}3$$

$I_{(100)}$ and $I_{(200)}$ are the intensities of the PMN-PT 100- and 200-peaks, and $\sum I_{(hkl)}$ is the summation of the intensities of all peaks present in that XRD scan. P_{LF} is calculated from the textured PMN-PT thin film samples as measured in the XRD scans, and $P_{LF,0}$ is measured from the powder diffraction files (PDF) for PMN-PT.

3.2.2 Thickness Measurements

The thickness of the films were measured two different ways. The first was using the Tencor P15 Profilometer. A step was created via etching, as described in previous section, to expose the bottom electrode. Profilometry was then performed across this step to determine film thickness.

Scanning electron microscopy (SEM) was also used to determine thickness. The films were snapped using a diamond scribe. The cross section of the film was then imaged using the Hitachi 8230 field emission SEM utilizing a novel cold field emission gun was used to scan images of the cross section. Continuous scanning images were taken to ensure that drifting would not distort the images.

3.2.3 Grain Structure Characterization

The cross sectional grain morphology was examined using SEM imaging on a Hitachi 8230 FE-SEM. Plain view SEM images were used to characterize the average grain size and observe grain growth and porosity. SEM imaging was performed at an accelerating voltage of 5 kV and current of 10 μA.

Atomic force microscopy (AFM) was used to observe surface grain morphology using an Alysum Research MFP-3D or Asylum Research Cypher. Contact and tapping mode was used to examine grain size, porosity, and crack formation on PMN-PT films. Scan sizes from 5 to 20 μm with scan rates from 0.5 to 2 Hz were made. 1 V was used as the contact set point. Pt- or Ir-coated tips from Budget Sensors, Olympus, and NanoSensors were used.

3.3 Functional Response Characterization

3.3.1 Low-field Dielectric Response

Low-field dielectric response was measured using an Agilent 4284A Precision LCR meter. Low field measurements were performed at 100 mV and 1 kHz. The LCR meter measures the capacitance of an electrode-ferroelectric-electrode sandwich, which can then be converted to relative dielectric permittivity (ε_r) following the formula:

$$C = \frac{\varepsilon_r \varepsilon_0 A}{d} \tag{3-4}$$

where C is the measured capacitance, ε_0 is the vacuum permittivity, A is the cross-sectional area of the ferroelectric capacitor being measured, and d is the thickness of the ferroelectric material.

The dielectric loss tangent describes a material's intrinsic dissipation of electromagnetic energy. δ is the loss angle, and tan(δ) is the dissipation factor. Measurements of tan(δ) are performed simultaneously with the capacitance measurements.

3.3.2 Polarization-Electric Field and Switching Current Loops

Polarization-AC electric field (P-E) hysteresis loops are measured using a Radiation Technologies P-PM2 ferroelectric test system, with a bipolar sine wave at 1 kHz, with fields ranging from 100 to 3000 kV/cm. The P-E loops were analysed to determine the remanent polarization (P_{rem}), saturated polarization (P_{sat}), coercive fields (E_C), and loop areas. The internal bias of the samples could also be calculated from the coercive fields with the following formula:

$$E_{internal\ bias} = \frac{E_{C+} + E_{C-}}{2} \tag{3-5}$$

Switching current-AC electric field loops show the change in polarization with electric field, which can help identify changes in the P-E loop that are otherwise unrecognizable. These are measured on the same tool as the P-E loops, with similar bipolar sine wave at 1 kHz and fields ranging from 100 to 3000 kV/cm.

3.3.3 Nonlinear AC Electric Field-Dependent Dielectric Permittivity

The AC electric field dependence of the dielectric permittivity gives information on the intrinsic and extrinsic contributions to the ferroelectric response, as discussed previously. The capacitance and dissipation factor of the films were measured at AC electric fields from ~1 kV/cm and up to the coercive field at 1 kHz on an aixACCT tool. The capacitance was converted to dielectric permittivity using Equation 3-4, and the real part of the dielectric permittivity was extracted using the dissipation factor. The real permittivity-field dependence is then linearly fit according to Rayleigh's law, and the slope and y-intercept extracted as the Rayleigh parameters: extrinsic (α') and intrinsic ($\varepsilon'_{\mathrm{init}}$) contributions to the response.

3.3.4 DC Electric Field-Dependent Dielectric Permittivity

Dielectric permittivity as a function of DC electric field allows for further investigation of domain wall motion and extrinsic contributions to dielectric response. These measurements were performed up to maximum fields of 200-400 kV/cm with an overlapping small-signal 100 mV at 1 kHz on an aixACCT tool. The dielectric tenability is calculated with the following formula:

$$dielectric\ tunability = \frac{\varepsilon_{DC,max} - \varepsilon_{DC,min}}{\varepsilon_{DC,max}} \qquad 3\text{-}6$$

where $\varepsilon_{DC,max}$ and $\varepsilon_{DC,min}$ are the maximum and minimum dielectric permittivity values of the measured curve, respectively. The dielectric tunability is often reported as a percent to report its efficiency for filter applications. In the literature, these curves will often be called C-V loops, from the raw capacitance-voltage curves typically measured.

3.3.5 Piezoelectric Response

Measurements of piezoelectric response in ferroelectric thin films can be achieved by quantifying the direct or converse piezoelectric effects, through charge measuremetns or strain/displacement measurements, respectively. In this work, the converse piezeoelectric effect is measured on the aixACCT double beam laser interferometry

(DBLI). Specifically, the effective displacement of the film in the z-direction (through the thickness of the film) is measured as a function of an applied DC electric field in the same direction ($d_{33,f}$). A DC field with maximum of 200-400 kV/cm is applied with an overlapping small-signal of 1 V. A laser is split and directed towards the bottom of the wafer and the top of the electrode being measured, taking into account bending of the substrate induced by the piezoelectric thin film. The use of lasers requires highly reflective surfaces for the detector to detect the laser deflections. The Pt top electrodes provide sufficient enough reflection for this. The underside of the substrate must be polished to be reflective enough. This is done by masking the top side of the film with SPR-220 photoresist, spread across the film and baked for ~4 min or until hardened when cooled. The samples were then polished manually on a rotary polishing wheel with 1 μm, 0.3 μm, and 0.05 μm Al_2O_3 powders until mirror polished. The photoresist was removed with acetone and rinsed with IPA followed by DI water.

3.4 Gamma Radiation Exposure

Total ionization dose experiments were conducted in collaboration with the U.S. Naval Research Laboratory. The films were exposed to gamma rays via a ^{60}Co source, producing radiation energies of approximately 1.17 or 1.33 MeV. The geometry of the ^{60}Co gamma source surrounds the sample, resulting in isotropic exposure and eliminating any effects of directionality. Doses were chosen with a logarithmic spacing, at 0.1, 0.2, 0.5, 1.0, 2.0, 5.0, and 10.0, at a dose rate of ~400 or ~600 rad(Si)/s. All electrodes were left floating during radiation exposure. In order to mitigate electrode variation, 5 to 10 electrodes were measured on each sample and remeasured after irradiation to make direct comparisons in changes in functional response. All samples were characterized within 1 week of radiation exposure to reduce effects of aging. A control sample was sent to account for changes in the functional response due to either aging or transportation.

Figure 3-5 Image of the ^{60}Co source used to irradiate the samples. Photo courtesy of Cory D. Cress, U.S. Naval Research Laboratory.

CHAPTER 4. MICROSTRUCTURE ENGINEERING PMN-PT THIN FILMS

4.1 Introduction

PMN-PT thin films can exhibit higher piezoelectric response than the current standard, PZT. However, the challenges associated with processing niobate materials, such as the need for higher crystallization temperatures, has made it difficult to reliably fabricate high quality PMN-PT thin films. The microstructure of these films will often contain large pores and show eventual cracking at thicknesses greater than 600 nm. One of the largest issues is control of Pb content, as PbO can easily volatilize out of the films during the annealing process, especially at the elevated crystallization temperatures. Preferential volatization of PbO at grain boundaries, the formation of organics or PbO pockets, and Pb-deficient secondary phases can all lead to unideal thin film microstructures. While the effects of different processing parameters in chemical solution deposition on the microstructure are unavoidably intertwined, this work attempts to draw attention to areas which can help improve PMN-PT thin film quality. Seed layers, precursor solutions, and drying, pyrolysis, and annealing temperatures will be varied to understand their role in both the microstructure and the functional response of PMN-PT thin films.

4.2 Experimental Procedures

$0.7Pb(Mg_{1/3}Nb_{2/3})O_3$-$0.3PbTiO_3$ (0.7PMN-0.3PT) thin films were processed via chemical solution deposition (CSD). Thin films were deposited onto (001) Si substrates with one of two substrate stacks: (a) substrates sputtered at Georgia Tech (GT) with 80 nm Pt // 20 nm TiO_2 // 1000 nm SiO_2 // Si, or (b) provided by the US Army Research Laboratory (ARL) with 100 nm Pt // 35 nm TiO_2 // 750-2000 nm SiO_2 // Si. Seed layers of PTO were tested with excess Pb concentrations between 5 and 30% for control of PMN-PT films' orientation. PMN-PT precursor solutions were made with solution molarity of 0.3M and 0.4M, and with excess Pb concentrations between 5 and 40%. Solution deposition was tested with or without a drying step at 250 °C for 1 to 5 minutes, pyrolysis temperatures ranged from 360 °C to 430 °C for 3 to 5 minutes, annealing temperatures from 700 °C to 800 °C for 1 to 2 minutes, and film stacks were annealed after every 1 and 3 layers of deposition and pyrolysis. Films were processed in sets to equivalent thicknesses of 300 - 600 nm.

X-ray diffraction (XRD), scanning electron microscopy (SEM), and atomic force microscopy (AFM) were used to identify crystallographic orientation and phase, grain morphology, porosity, and cracking in the films. Functional response of the films were measured and correlated to microstructure of films: including, in order, low-field permittivity, polarization response, nonlinear dielectric response, DC field-dependent permittivity response, and DC electric field-dependent electromechanical response.

4.3 Results and Discussion

4.3.1 Orientation control and seed layers

In order to obtain (001)-oriented films, PbO and PTO seed layers with various amounts of excess Pb were tested. The seed layers and subsequent PMN-PT layers were deposited onto both in house Pt sputtered Si wafers and on ARL Pt sputtered wafers to test reproducibility. X-ray diffraction imaging was used to determine the orientation of the films. As shown in Figure 4-1, none of the seed layers provided good (001)-orientation, despite reports by both Keech et al. and Bastani et al. showing success in utilizing these seed layers for good (001)-orientation of PMN-PT thin films.[56,60] Possibility of hillocking of films from Pb penetration through the Pt layer due to excessive Pb content in the seed layers was of concern while using the GT substrates.[88] However, further testing of seed layers with increasing Pb content was needed to obtain the desired orientation. Using the ARL substrates, it was found that 30% excess Pb content in the PTO precursor solution was necessary to ensure (001)-orientation for the PMN-PT films. The higher quality and density of the sputtered Pt layer from ARL in comparison to that sputtered at GT likely prevented the issue of excess Pb penetrating through and potentially causing hillocking of the films. Subsequently, this prevented the surface of the PTO seed layer from becoming Pb-deficient, allowing the layer to act as a proper seed for (001)-oriented PMN-PT layers.

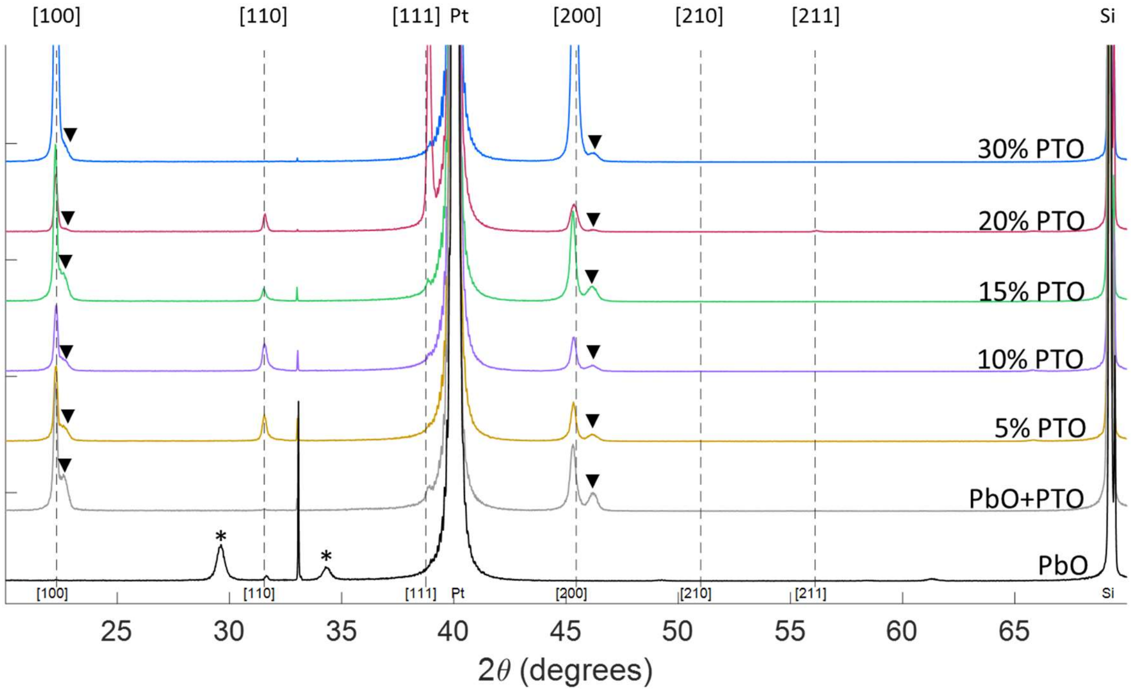

Figure 4-1 X-ray diffraction of PMN-PT thin films with various seed layers.

4.3.2 CSD Processing Parameters

Processing parameters including drying, pyrolysis, and crystallization temperatures and durations were then tested for microstructural control. The specific parameters tested are detailed in Table 4-1. Samples *A* and *B* were processed with parameters from literature approaches to test the reproducibility of the results, while sample *C* was specifically modified to combine aspects of the previous two recipes. A precursor solution of 0.4M 0.7PMN-0.3PT with 15% excess Pb was used for this test. SEM cross-sectional images reveal large differences between the grain size, grain morphology, pore size, and pore location (Figure 4-2). Samples *B* and *C* have much larger grain sizes than sample *A*, likely due to the high crystallization temperatures, in agreement with studies as discussed earlier.

Larger pores were found in sample *B* in comparison to samples *A* and *C*. It is possible that the lack of drying step and low pyrolysis step led to pockets of organics or PbO, leading to larger volumes which volatize into pores during the annealing step. Since previous studies have shown that larger grain sizes lead to better functional response, samples *B* and *C* were determined to have better grain structure than sample *A*.[56,89] Sample *B* was selected for further studies of effects of excess Pb content in the precursor solution on film microstructure and functional response due to the location of pores. Pores between grains would lead to fewer interfacial regions as opposed to the pores found within the grains in sample *C*.

Table 4-1 Processing parameters used to defect-engineer PMN-PT thin films.

	Spincoating	Drying	Pyrolysis	Crystallization	Layers Crystallized Together	Ref.
A	2500 rpm x 45 s	250°C x 2 min	430°C x 5 min	700°C x 1 min	1	58
B	3000 rpm x 30 s	--	360°C x 2 min	800°C x 2 min	3	56
C	3000 rpm x 30 s	250°C x 1 min	400°C x 5 min	800°C x 1 min	1	--
D	3000 rpm x 30 s	250°C x 1 min	400°C x 5 min	800°C x 2 min	3	--

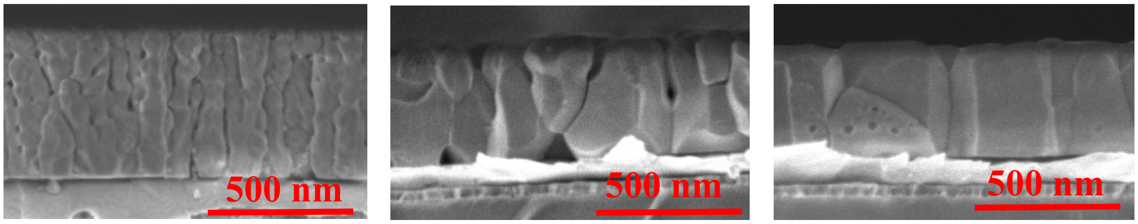

Figure 4-2 Cross-sectional SEM of PMN-PT thin films using recipes A (left), B (middle), and C (right).

4.3.3 *Precursor Solution Pb Content*

To understand the role of excess Pb in pore formation and functional response, films were fabricated using *B* processing parameters found in Table 4-1, with Pb excess concentrations in precursor solution from 10 to 25%. Cross-sectional SEM images (Figure 4-3) revealed a decrease in pore size and amount with increasing Pb content, which can be attributed to two different mechanisms. First, because of excess Pb content in solution, a larger amount of Pb is still left in the films after some amount diffuses through the substrate stack, preventing issues of pockets between deposited layers. Second, the excess Pb could also be compensating for lead loss during the crystallization step, preventing the formation of pockets. The trend in functional response of the films with increasing Pb content is shown in Figure 4-5. In dielectric permittivity, a general increase was found with increasing Pb content used, likely correlated with the decrease in porosity and Pb-deficient phases in the material. While dielectric loss is lowest in the 25% excess Pb sample, the difference in losses is minimal across the four samples. The Rayleigh law analysis revealed increasing

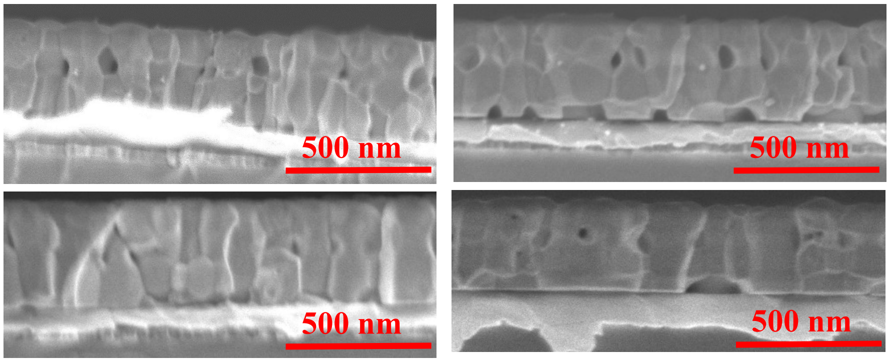

Figure 4-3 Cross-sectional SEM images of PMN-PT films fabricated with precursor solutions with excess Pb content of 10% (top left), 15% (top right), 20% (bottom left), and 25% (bottom right).

intrinsic response (ε'$_{init}$) with increasing Pb content, however the 20% excess Pb film showed the highest extrinsic contribution (α'). In polarization response, a general increase in saturated polarization was found with increasing Pb content. Differences in the internal bias can be seen in the polarization-field loops (Figure 4-4), indicating a difference in distribution of defects which lead to internal bias. In piezoelectric response, while the values were not substantially different, the largest saturated piezoelectric coefficient was found in the film with 25% excess Pb content in precursor solution. In general, it was found that increased Pb content in the precursor solution led to less porosity and higher functional response. However, large amounts of porosity were still found in the films, possibly from trapped PbO pockets or organic solvent which then volatize quickly and leave pores behind during the annealing process. In an attempt to reduce these effects, the solution molarity was decreased to create thinner films to promote more uniform pyrolysis and annealing.

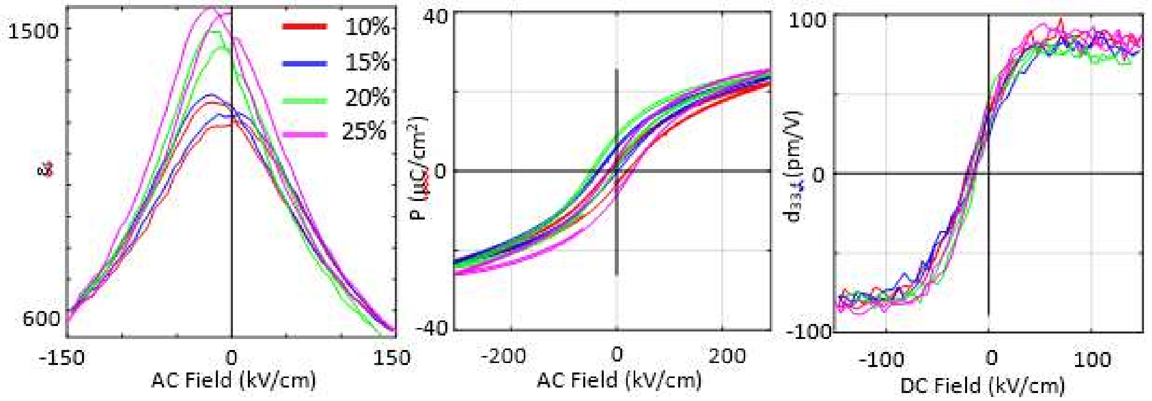

Figure 4-4 Dielectric permittivity-field, polarization-field, and piezoelectric-field curves of PMN-PT thin films processed with precursor solutions of varying excess Pb content.

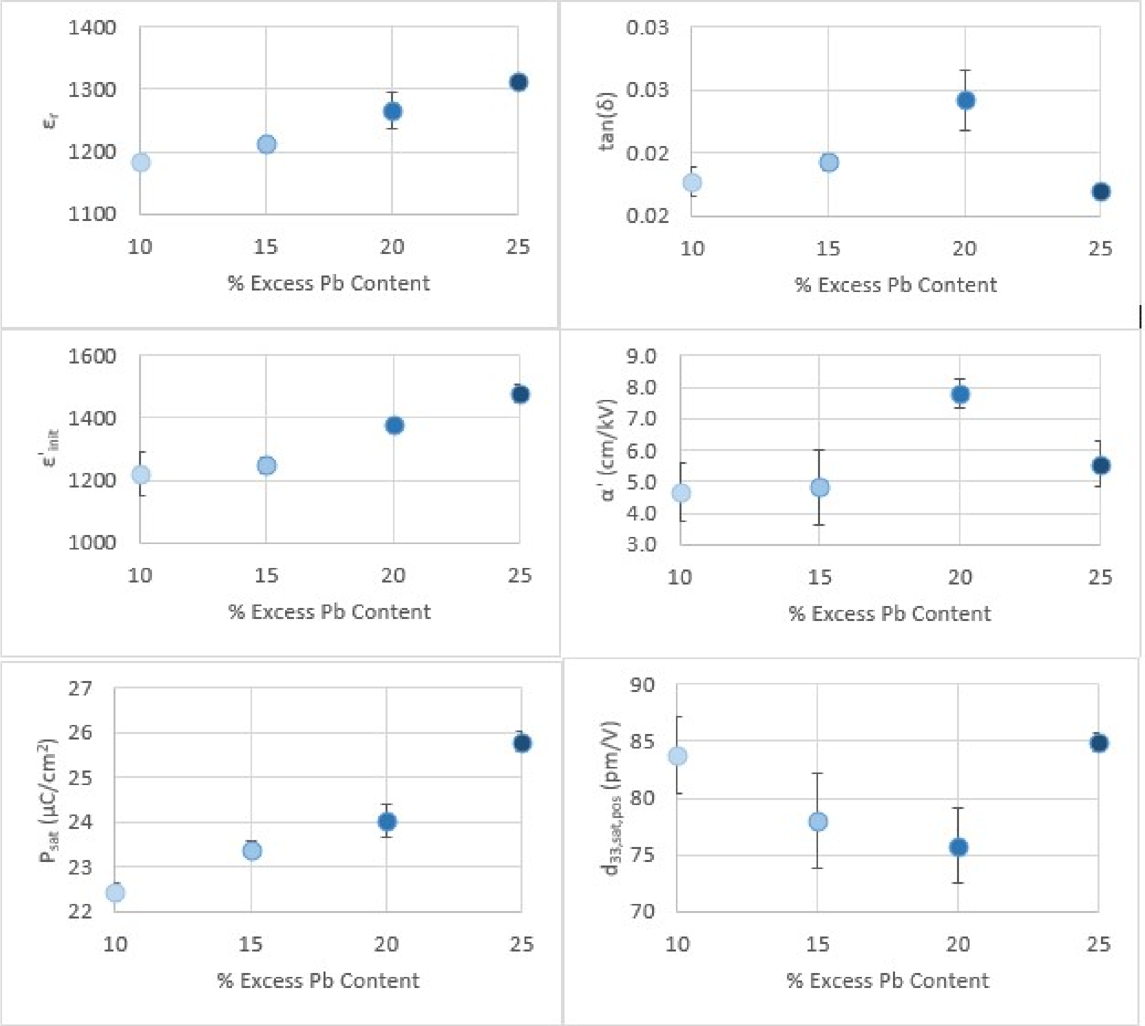

Figure 4-5 Trends in functional response of films fabricated with precursor solutions with increasing excess Pb content.

4.3.4 *Precursor Solution Molarity*

Films were fabricated with a 0.3M precursor solution of 0.7PMN-0.3PT with 40% excess Pb, and processing parameters *A*, *B*, and *C* were used. Films were processed to 300 nm thick as a preliminary test before attempting to fabricate thicker films for comparison studies. An extremely high Pb excess content was used in order to compensate for any excess Pb loss that could occur with processing thinner layers than compared with 0.4M solutions. SEM imaging (Figure 4-6) confirmed that the films contained smaller amounts of porosity, but also showed significant changes in the morphology of the grains compared to the previous set. While sample *A* showed no indication of porosity, it showed unusual grain morphology with much smaller grains, similar to results found in the previous set of samples. Sample *B* showed indication of pores as well as unusual grain morphology, however seemingly larger grains than in sample *A*. Sample *C* showed better quality grain morphology than either of the other two, with large grain sizes and high density, attesting to the necessity of high drying/pyrolysis steps as well as high annealing temperatures. While attempting to obtain functional measurements, sample *B* showed extremely high losses, while sample *A* showed significantly lower functional response than sample *C*. This is consistent with previous reports of films where larger grain sizes and more dense films had higher functional response than other films. By minimizing defects in the films with a lower concentration of grain boundaries as well as pore interfaces, the domain wall motion is higher and can contribute to higher functional response.

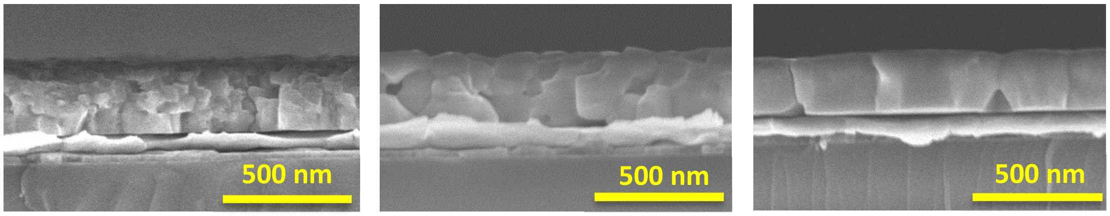

Figure 4-6 Cross-section SEM images of PMN-PT thin films processed with 0.3M precursor solution and recipes A (left), B (middle), and C (right).

The polarization response was then tested in these three films to understand how the grain structure affected the response (Figure 4-7). Recipe C has a higher polarization response than sample *A*, likely due to the more columnar grain structure of sample *C*. Grain boundaries can act as barriers to domain wall motion, decreasing the polarization response, as well as other responses, in the film. Measurements were unobtainable for sample *B*, due to extremely high losses. These losses are possibly due to pinhole defects, as these samples are only ~300 nm thick.[90] To further analyze the effects of molarity and processing parameters on these thin films, thicker samples were processed.

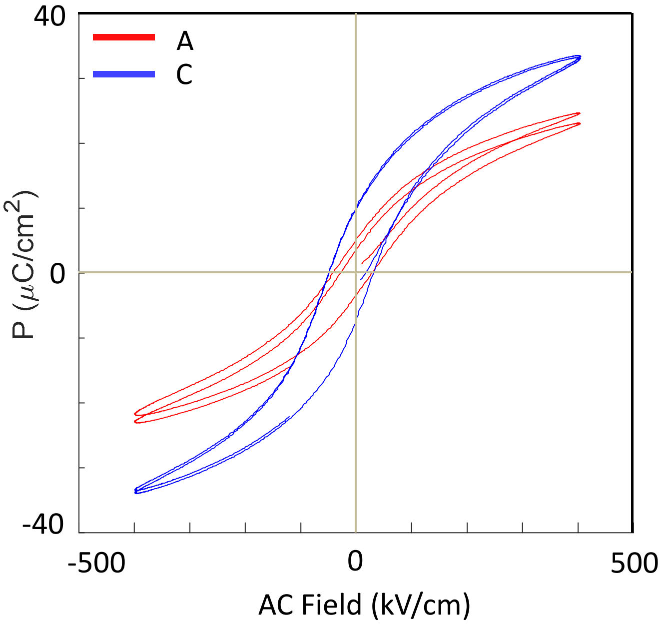

Figure 4-7 Polarization response of films fabricated with 0.3M precursor solution and 40% excess Pb.

4.3.5 Microstructural effects on functional response

In order to study the effects of grain morphology and porosity on both functional response and radiation tolerance, discussed further in chapter 6, films were fabricated to ~500 nm in thickness using the 0.3M solution with 40% excess Pb content and the recipes A and C. An additional sample *D* was added to test the feasibility of crystallizing several layers at once, which would greatly minimize the time necessary to process the thin films.

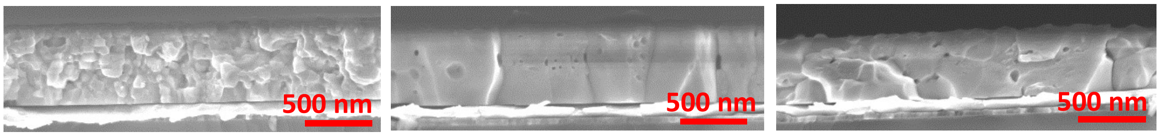

Figure 4-8 Cross-sectional SEM images of PMN-PT thin films using 0.3M solution and recipes A (left), C (middle), and D (right).

SEM images shown in Figure 4-8 reveal similar morphology to the previous set in recipes A and C. The morphology of sample *D* was similar to sample *B* with a mixture of stacked and columnar grains.

Dielectric permittivity, polarization, and piezoelectric responses, shown in Figure 4-9, reveal that sample *A* has the lowest functional response of the three films. Sample *C* shows the highest response in permittivity, and both samples *C* and *D* have similarly high polarization and piezoelectric response. Although sample *A* revealed minimal porosity, the large concentration of grain boundaries led to an increase in domain pinning, subsequently decreasing its overall functional response. Despite the presence of porosity, the films with

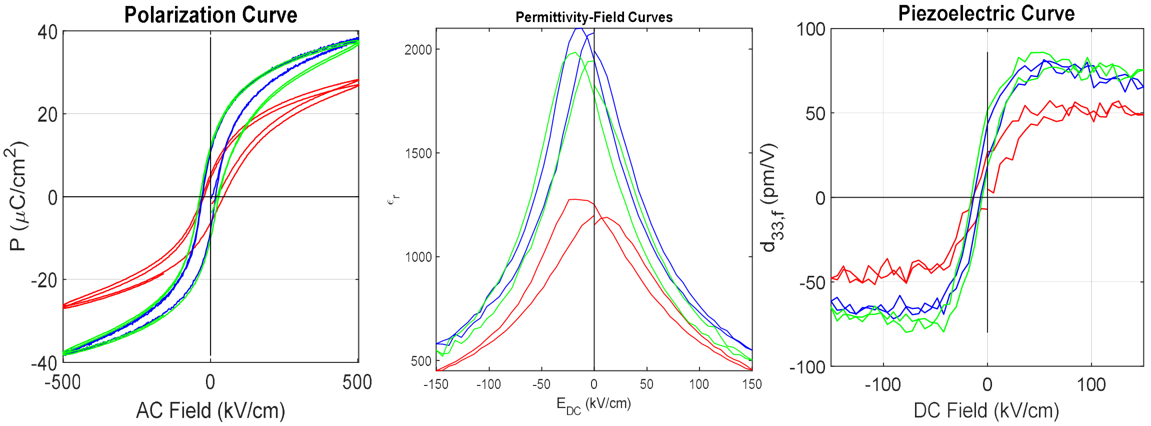

Figure 4-9 Polarization-field (left), permittivity-field (middle), and piezoelectric-field curves of PMN-PT films processed with 0.3M precursor solution and recipes A (red), C (blue), and D (green).

large, columnar grains maintained higher overall functional response than the film with minimal porosity but small, stacked grains.

4.4 Conclusions

Various processing parameters for chemical solution deposition of PMN-PT thin films were explored in this work. Pb content is crucial as it can influence the formation of secondary phases and pores throughout the film. Increased Pb content in PTO seed layers were shown to give increased (001)-oriented PMN-PT thin films, possibly due to the elimination of lead-deficient phases at the surface of the seed layer. Increased Pb content in the PMN-PT precursor solution appeared to decrease the size of pores in PMN-PT thin films. This also increased the dielectric, polarization, and piezoelectric responses, likely due to elimination of pores and non-ferroelectric phases. Decreasing the molarity of the solution increased the density of films, possibly through reduction of trapping of organics or PbO pockets which can potential volatilize and leave behind pores during the crystallization process. Higher crystallization temperatures (~800 °C) promoted the formation of large, columnar grains. While porosity was eliminated using higher drying and pyrolysis temperatures in combination with lower crystallization temperatures, the functional response was compromised due to the increase in grain boundaries which often act to reduce domain wall motion in ferroelectric materials.

CHAPTER 5. RADIATION TOLERANCE OF PMN-PT THIN FILMS VS PZT THIN FILMS

The content in this chapter has been published in *IEEE Transactions on Ultrasonics, Ferroelectrics, and Frequency Control.*[91]

Effects of Gamma Irradiation on Functional Response of Relaxor-Ferroelectric Thin Films

Evelyn S. Chin, Cory D. Cress, Ryan Q. Rudy, Nazanin Bassiri-Gharb

IEEE Transactions on Ultrasonics, Ferroelectrics, and Frequency Control, vol. 67, no. 5, (2020), doi: 10.1109/TUFFC.2019.2963194

5.1 Summary

This work investigates the radiation response of relaxor-ferroelectric, lead magnesium niobate-lead titanate thin films, as an alternative material for micro-electro-mechanical systems (MEMS) devices in harsh environments. PMN-PT ($0.7Pb[Mg_{1/3}Nb_{2/3}]O_3$-$0.3PbTiO_3$) thin films were fabricated via chemical solution deposition onto platinized Si wafers and exposed to gamma radiation doses up to 10 Mrad(Si). The functional response of the thin films was measured before and after irradiation, and the resulting changes reported. Within the radiation dose range studied, dielectric permittivity, tunability, and saturated polarization showed <5% change, and saturated piezoelectric coefficient <10% change. Additionally, PMN-PT thin films showed equivalent or superior radiation tolerance compared to lead zirconate titanate thin films previously studied. Higher chemical heterogeneity and greater domain wall mobility are expected to contribute to overall greater radiation tolerance in PMN-PT thin films. Nonlinear trends were found in dielectric and piezoelectric response with increasing dose, showing enhanced response at low doses of radiation before degradation at high doses. However, such variations were also within the experimentally observed dispersion of the data. The results are expected to impact systems to be deployed in areas of high radiation exposure, including systems used in aerospace, medical physics, x-ray/high energy source measurement tools, and continuous monitoring of nuclear power applications.

5.2 Introduction

Ferroelectric perovskites exhibit large dielectric, pyroelectric, and piezoelectric properties, making them ideal for many microelectronics applications such as multi-layer ceramic capacitors (MLCCs), ferroelectric logics and memories, microelectromechanical systems (MEMS) sensors and actuators, and energy harvesting units for self-powered devices.[1,92] Of increasing interest is the use of MEMS devices in increasingly demanding environments, such as for aerospace, medical physics tools, and continuous monitoring systems for nuclear facilities or disaster areas. Ferroelectric materials have shown superior radiation tolerance compared to many other functional materials[93]; however, these materials still exhibit degradation in functional response with increased radiation doses. The industry standard, lead zirconate titanate (PZT), shows as high as 30% degradation in piezoelectric response at or above 5 Mrad(Si) gamma-ray irradiation.[40,47,50,51] Radiation exposure leads to ionization of atoms (X-rays and γ-rays), and with massive particles (protons, neutrons, >~1 MeV electrons, etc.) displacement of atoms. In general, degradation of both the dielectric and piezoelectric response is observed in ferroelectric materials and both correlate with the total ionizing dose, making it the primary radiation sensitivity of the material.[47,50]

Ionization leads to the generation of electron-hole pairs, and subsequent trapping of these charges results in changes in the defect landscape which hinder domain wall motion and degrade the material’s functional response. Bombardment with higher energy particles additionally amorphize the material, further degrading the response.[34,94] While different approaches have been attempted to increase radiation tolerance of ferroelectrics, including varying microstructure and material stacks, the best results were obtained through chemical doping.[26,49,52] Brewer et al. have shown that Mn-doped PZT thin films were largely unaffected by gamma-radiation exposure up to 10 Mrad(Si), as compared to their un-doped counterpart. The difference was attributed to the creation of $Mn''_{Ti} - V_{O}^{\cdot\cdot}$ defect-dipoles in doped samples, which reduced the mobility of oxygen vacancies, even those singly charged by trapping of radiation-induced free electrons.[49] However, these defect-dipoles also act as pinning centers and hinder domain wall motion, reducing the overall dielectric and electromechanical response of the films. This study aims to explore lead magnesium niobate-lead titanate (PMN-PT) as an alternative to PZT, potentially providing higher radiation tolerance without compromising high functional response.

Specifically, (001)-cut and poled single crystal relaxor-ferroelectric solid solutions on the rhombohedral side of the morphotropic phase boundary offer very large piezoelectric response, superior to PZT ceramics.[54] 0.7PMN-0.3PT thin films have been successfully deposited for thicknesses up to 2 μm, with piezoelectric coefficients ranging between 100 and 210 pm/V.[56,58] The high functional response is often correlated to large chemical and structural heterogeneities as well as large domain wall concentration and mobility, characteristics which may prove to be beneficial for radiation tolerance.[55,95] In this work, total ionization dose (TID) studies by γ-rays are conducted on PMN-PT thin films to evaluate their radiation response, and to compare their viability against PZT thin films

5.3 Experimental Procedure

$0.7Pb(Mg_{1/3}Nb_{2/3})O_3$-$0.3PbTiO_3$ thin films were fabricated via chemical solution deposition and spin coating onto platinized silicon wafers: Si / SiO_2 (2000 nm) / TiO_2 (35 nm) / Pt (100 nm). A 20 nm thick $PbTiO_3$ film with 30% excess Pb in the precursor was deposited first by spin coating onto the substrate to aid in 001-orientation of the PMN-PT films.[96] A 0.4M precursor solution with 25% excess Pb was prepared following a 2-methoxyethanol route, described by Park *et al.*.[58] The solution was spin coated onto the substrate at 3000 rpm for 30 seconds. Each deposited layer was pyrolyzed on a hot plate at 360 °C for 2 minutes, and every three layers were crystallized using a rapid thermal annealer (Solaris 75; Surface Science Integration, El Mirage, AZ) at 800 °C for 2 minutes.[56] The process was repeated to reach an overall PMN-PT film thickness of ~500 nm. X-ray diffraction (XRD) was performed using a PANalytical Alpha-1. Scanning electron microscopy (SEM) (Hitachi SU8230 FE-SEM) and atomic force microscopy (AFM) (Asylum Research MFP-3D) were used to explore the film microstructure.

Circular Pt top electrodes of 500 μm diameter and 70 nm thickness were deposited by sputtering and patterned via lift off for functional characterization. All but one film were exposed to gamma radiation with doses ranging from 0.2 to 10 Mrad(Si) at a rate of ~600 rad(Si)/s using a ^{60}Co source at the U.S. Naval Research Laboratory. The unexposed film was used as a control sample to account for external factors such as aging and exposure to radiation during shipments. The functional response of the samples were characterized before and after irradiation using the same electrodes per sample. The characterization was performed in the following order: 1) low-field dielectric permittivity and loss (100 mV, 1 kHz, Agilent 4284A LCR meter); 2) polarization-electric field (P-E) hysteresis loops (300 kV/cm, 100 Hz sine wave, Radiant P-PM2); 3) nonlinear dielectric permittivity (up to 30 kV/cm AC, 1 kHz, aixACCT double beam laser interferometer); 4) DC electric field-dependent permittivity, i.e. dielectric tunability (up to 150 kV/cm DC, with overlapping 100 mV AC signal, aixACCT double beam laser interferometer); and 5) electric field-dependent converse, effective longitudinal piezoelectric response (up to 150 kV/cm DC, with overlapping 1 V AC signal, aixACCT double beam laser interferometer). The order of the experiments was chosen from low to high field to minimize influence of additional applied fields to each measurement. All measurements were performed on a minimum of five electrodes per sample, and are subject to 3%-5% experimental error due to sample variability and measurement error. The Rayleigh approach was used to analyze the nonlinear dielectric response and quantify changes in intrinsic (lattice and domain wall vibrations) and extrinsic (irreversible domain wall motion) contributions to the dielectric response. These parameters were extracted from the linear region of the nonlinear dielectric response up to 10 kV/cm as to not exceed the coercive field of the films.

5.4 Results and Discussion

XRD revealed (100) Lotgering factors of over 95% for all films, as shown by the representative XRD scan in Figure 5-1. The films had dense, columnar grains of 100 to 300 nm in diameter, with some amount of porosity observed at the grain boundaries.

The virgin films showed dielectric permittivity up to ~1800, dielectric losses of 0.02 - 0.03, and dielectric tunability of ~75%. Saturated polarization was ~30 $\mu C/cm^2$ at electric fields of 400 kV/cm. Saturated effective piezoelectric coefficients were ~80 pV/m at electric fields of 150 kV/cm. These properties were comparable to that of PMN-PT thin films found within the literature.[56,59] Polarization-field, permittivity-field, and piezoelectric-field curves all show good saturation in the response, as shown in Figure 5-2.

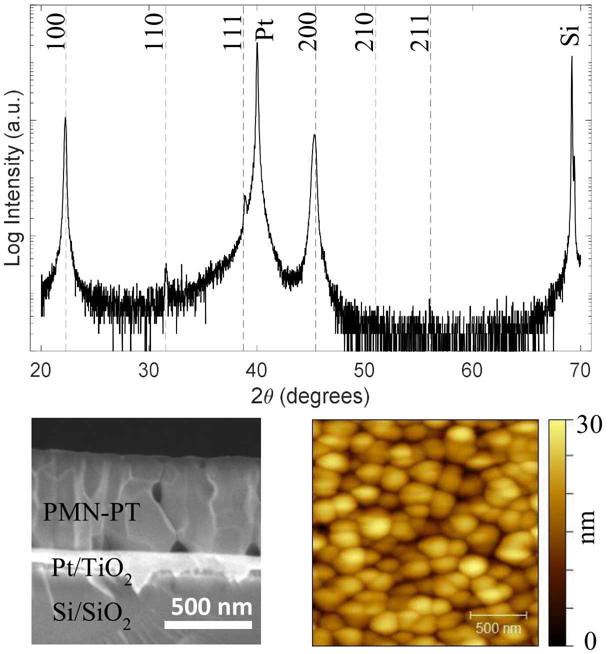

Figure 5-1 Microstructure characterization of PMN-PT thin films. Representative X-ray diffraction (top), cross-sectional SEM (bottom left), and surface morphology by AFM (bottom right).

Table 5-1 shows functional response values of virgin and irradiated PMN-PT thin films, wherein the control sample is labeled as 0 Mrad. PMN-PT films showed degradation of less than 5% for both dielectric permittivity, ε_r, and dielectric tunability up to a dose of 10 Mrad, within experimental error. Dielectric loss, tan(δ), remained within the 0.02 to 0.03 range. The reversible Rayleigh parameter, ε_{init}, showed up to 6% degradation at higher radiation doses. However the control sample showed ~4% change within the same

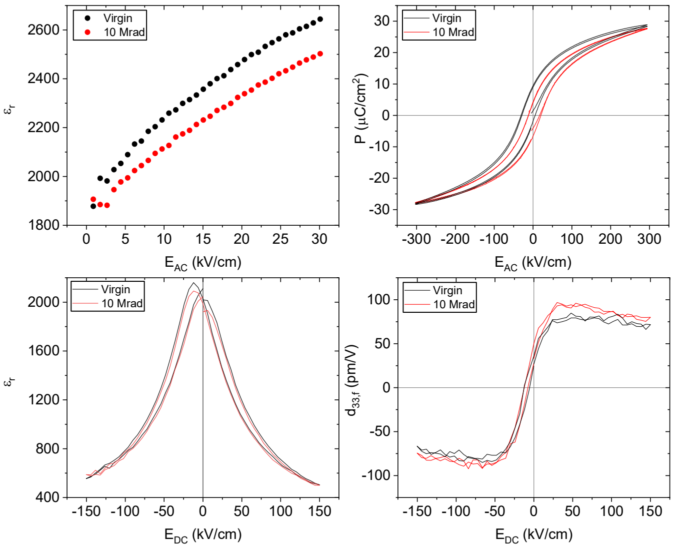

Figure 5-2 Comparison of nonlinear dielectric response (top left), polarization-electric field (P-E_{AC}) hysteresis (top right), dielectric tunability as measured by dielectric permittivity, ε_r, as a function of DC electric field, E_{DC} (bottom left), and effective piezoelectric coefficient, $d_{33,f}$, as a function of E_{DC} (bottom right), for virgin samples and after exposure to 10 Mrad(Si) γ-rays.

experiment, indicating that radiation effects were only partial contributors to the observed changes. Similarly, while the irreversible Rayleigh parameter, α, showed up to ~15% change at higher doses, the control sample also showed ~17% change, indicating that the changes observed were minimally influenced by radiation effects. Negligible changes were found in saturated polarization, P_{sat}, across all doses. Larger decreases were found in the positive remanent polarization values, $P_{\mathrm{rem,pos}}$; however, in most cases a corresponding decrease (increase in magnitude) was found in the negative remanent polarization values, $P_{\mathrm{rem,neg}}$. As seen in Figure 5-2, these shifts are indicative of a change in the internal bias. A similar magnitude of internal bias shift is found in the control sample, indicating strong influence by other factors besides irradiation. Negligible changes were also found in the saturated effective piezoelectric coefficient, $d_{33,f,sat}$, as all doses showed less than 5% change with the exception of an 8% enhancement after irradiation at 5 Mrad. Nonetheless, this change is still within standard deviation of the control sample.

Table 5-1 Functional response of PMN-PT thin films before and after irradiation by γ-rays as a function of dose, up to 10 Mrad(Si). The errors shown are one standard deviation.

		0 Mrad	0.2	0.5	2.0	5.0	10.0
ε_r	Virgin	1830 ± 13	1770 ± 40	1810 ± 33	1760 ± 27	1770 ± 26	1830 ± 45
	Irradiated	1870 ± 12	1770 ± 40	1870 ± 26	1830 ± 30	1800 ± 30	1810 ± 51
ε_{init}	Virgin	1980 ± 50	1890 ± 49	2010 ± 40	1950 ± 34	1950 ± 35	1960 ± 56
	Irradiated	1900 ± 33	1772 ± 60	1880 ± 35	1860 ± 40	1850 ± 26	1860 ± 48
α (cm/kV)	Virgin	26 ± 2	21 ± 3	23 ± 1	25 ± 2	25 ± 3	27 ± 2
	Irradiated	23 ± 2	21 ± 2	21 ± 2	22 ± 2	21 ± 1	24 ± 2
P_{sat} (μC/cm^2)	Virgin	30 ± 0.4	28 ± 0.6	29 ± 0.5	29 ± 0.7	29 ± 0.3	29 ± 0.7
	Irradiated	28 ± 0.2	27 ± 0.6	29 ± 0.4	28 ± 0.7	28 ± 0.2	28 ± 0.7
$P_{rem,pos}$ (μC/cm^2)	Virgin	9.4 ± 0.5	8.7 ± 0.5	9.7 ± 0.5	6 ± 2	8.9 ± 0.4	8 ± 1
	Irradiated	4.5 ± 0.2	4.3 ± 1.9	4.5 ± 0.3	4.4 ± 0.3	4.0 ± 0.3	6.0 ± 2.0
$P_{rem,neg}$ (μC/cm^2)	Virgin	-4.2 ± 0.3	-4 ± 1	-4.2 ± 0.4	-6 ± 2	-3.5 ± 0.4	-6 ± 2
	Irradiated	-7.2 ± 0.3	-6 ± 2	-7.6 ± 0.5	-6.6 ± 0.3	-7.0 ± 0.4	-6 ± 3
Dielectric tunability (%)	Virgin	76 ± 0.5	75 ± 0.4	76 ± 0.6	76 ± 0.4	76 ± 0.4	76 ± 0.7
	Irradiated	76 ± 0.3	75 ± 0.6	76 ± 0.5	75 ± 0.1	75 ± 0.6	76 ± 0.6
$d_{33,f,sat}$ (pm/V)	Virgin	82 ± 4	78 ± 1	82 ± 2	81 ± 4	76 ± 3	78 ± 1
	Irradiated	81 ± 5	79 ± 1	80 ± 3	84 ± 4	82 ± 1	79 ± 1
$d_{33,f,rem,pos}$ (pm/V)	Virgin	45 ± 4	41 ± 7	49 ± 4	45 ± 4	44 ± 4	41 ± 7
	Irradiated	41 ± 6	44 ± 1	47 ± 4	39 ± 5	45 ± 2	44 ± 1
$d_{33,f,rem,neg}$ (pm/V)	Virgin	25 ± 6	26 ± 2	28 ± 2	22 ± 3	22 ± 2	26 ± 2
	Irradiated	22 ± 6	28 ± 3	25 ± 4	20 ± 5	24 ± 3	28 ± 3

Figure 5-3 overlays the TID studies for PMN-PT films with (100)-oriented, polycrystalline PZT films of similar thicknesses, grown on similar substrates by chemical solution deposition (previously reported by Brewer *et al.*[49]). PMN-PT films show either equal or superior radiation tolerance to PZT films. Specifically, $\varepsilon_{\text{init}}$ and α of PMN-PT are substantially unaltered by irradiation compared to PZT films. This suggests that PMN-PT is able to retain its high domain wall contribution to the functional response. It is possible that because PMN-PT has a high density of domain walls, the same number of defects will affect the mobility of an overall smaller percentage of the domain walls.[97,98] Hence, the extrinsic contributions to functional response are retained to a larger degree than in PZT at the same radiation dose. However, the types of defects introduced by irradiation might also be different in the two materials. In previous studies on PZT, it was found that free-electrons, liberated via ionizing radiation exposure, are subsequently trapped in pre-existing oxygen vacancies, modifying them into singly charged vacancies. Singly charged oxygen vacancies have higher mobility than doubly charged ones.[26,52] These vacancies, driven by an externally applied or built electric field, drift, accumulate, and self-order at interfaces thereby pinning domain walls and their motion, ultimately inducing fatigue-like effects on ferroelectric properties.[25] The multi-valence B-site cations in PMN-PT, Mg^{2+}, Ti^{4+}, and Nb^{5+}, could offer additional sites for trapping irradiation-generated free electrons. While the defect landscape of PMN-PT is still not well understood due to its chemical complexity, electron paramagnetic resonance studies predict that these cations can exist in various valence states (e.g., Nb^{4+}, Nb^{3+}).[99,100] Trapping of electrons at the B-site cations would result in a smaller number of singly charged oxygen vacancies generated through irradiation, thereby preventing the deleterious effects caused by accumulation of such vacancies at interfaces. Once an electron is trapped, the B-sites would become more attractive to radiation-generated holes suggesting that such sites could function as fast-recombination centers. We note that changes in ionic state of the B-site cations may also lead to changes in defect complexes, such as point defect clusters or defect-dipoles, which can influence domain wall motion.[101]

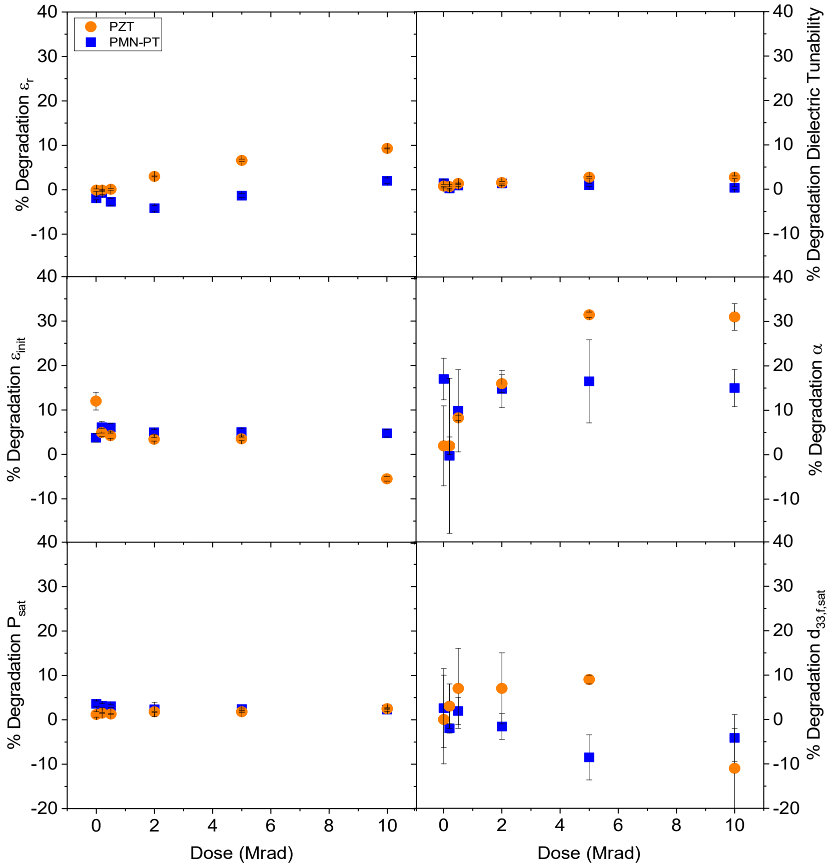

Figure 5-3 Percent degradation of functional response as a function of radiation dose of PZT thin films (orange circles) vs. PMN-PT thin films (blue squares). All films are polycrystalline and grown on platinized silicon substrates by chemical solution deposition

Two more factors should be taken into consideration when comparing the TID studies for PMN-PT and PZT films. First, with respect to microstructure, PZT films showed dense, columnar grains, while PMN-PT showed possible pores trapped between columnar grains. Increased porosity results in increased concentration of interfacial regions and grain boundary density, which can act as defect sinks, thereby increasing the radiation tolerance of the PMN-PT thin films.[102] In addition, previous studies on PMN-PT and PZT thin films have shown increased extrinsic contributions to the dielectric and piezoelectric response with a small amount of porosity, due to partial decoupling from the substrate.[57,103,104] Secondly, the previous PZT study utilized IrO_2 top electrodes instead of Pt used in this study. However, use of oxide electrodes results in increased radiation tolerance compared to metallic electrodes.[26] This is due to the oxygen conductivity of the former, which reduces oxygen vacancy accumulation and ordering at the ferroelectric-electrode interface. Hence, it is further remarkable that PMN-PT films show equivalent or superior radiation tolerance in all functional responses compared to PZT films.

Possible non-monotonic trends were observed for dielectric permittivity and piezoelectric coefficient TID studies: these properties showed slight enhancement (negative degradation) at lower doses before degrading at higher doses. While all changes are within experimental error, previous studies on various electronic materials have shown that the functional response of oxide materials can be enhanced with low radiation doses. For example, Saremi *et al.* have reported that He^+ ion bombardment of $PbTiO_3$ films increases the ferroelectricity.[105] Similarly, ion bombardment has been used to increase the critical current density of superconductors.[106,107] In these materials, the current density is dependent on ion mobility, which is influenced by the defects within the material. The ion bombardment introduces defects which allow for higher ionic mobility at lower doses of radiation, enhancing the material's superconducting properties. At higher doses, the accumulation of these radiation-induced defects eventually leads to degradation of the material. Thus, it is a possibility that this is also occurring in the PMN-PT films, but is due to a slightly different mechanism since ^{60}Co exposure does not always create an appreciable amount of displacement defects. Instead, the PMN-PT films may be comprised of a population of native defects. Those that become highly mobile upon ionizing radiation exposure could drift to domain walls, charging them in the process.[26,108,109] It has been theorized that a higher density of charged domain walls can lead to increased dielectric and piezoelectric response in ferroelectric materials. Thus radiation exposure initially heals the PMN-PT films.[110] Concomitantly, those defects that act as pinning centers upon trapping electrons gradually build-up overtime, eventually counter acting the initial healing and ultimately leading to degraded functional response. Since PMN-PT has a more complex and higher density network of domain walls, it is able to show greater radiation tolerance than PZT.

5.5 Conclusions

In summary, PMN-PT thin films were investigated as a radiation tolerant alternative material to the current industry standard PZT. PMN-PT showed higher dielectric and piezoelectric functionality, while also offering greater radiation tolerance in dielectric and piezoelectric responses at doses up to 10 Mrad. The higher domain wall mobility and concentration as well as higher degree of chemical heterogeneity are suspected to be contributing factors to both PMN-PT's higher functional response and greater radiation tolerance compared to PZT. Possible enhancement of response was also evident at low radiation doses, suggesting that radiation-induced defects may be able to improve functional response of these materials. The high functional response as well as high radiation tolerance makes PMN-PT an attractive option for designing next generation radiation-hard devices.

5.6 Acknowledgements

This work was supported by the Defense Threat Reduction Agency, Basic Research Award No. HDTRA 1-15-1-0035 to Georgia Institute of Technology. The contents do not necessarily reflect the position or the policy of the federal government, and no official endorsement should be inferred. The authors gratefully acknowledge Joel Martin of the Army Research Laboratory and Steven Isaacson of General Technical Services for providing platinized Si substrates for this work.

CHAPTER 6. PROCESSING-STRUCTURE-PROPERTY RELATIONS OF RADIATION TOLERANCE OF PMN-PT THIN FILMS

At the time of this publication, the content in this chapter has been accepted and is awaiting publication at *IEEE Transactions on Ultrasonics, Ferroelectrics, and Frequency Control.*

Processing-Structure-Property Relations for Radiation Tolerance of Relaxor-Ferroelectric Thin Films

Evelyn S. Chin, Cory D. Cress, Ryan Q. Rudy, Nazanin Bassiri-Gharb

IEEE Transactions on Ultrasonics, Ferroelectrics, and Frequency Control, (awaiting publication), (2020), doi: 10.1109/TUFFC.2020.2991647

6.1 Summary

This work investigates the role of microstructure on the radiation tolerance of relaxor-ferroelectric, lead magnesium niobate-lead titanate, thin films for piezoelectric micro-electro-mechanical system (MEMS) applications. Thin films comprised of $0.7Pb[Mg_{1/3}Nb_{2/3}]O_3$-$0.3PbTiO_3$ were fabricated via chemical solution deposition on platinized silicon wafers. Processing parameters, i.e. pyrolysis and annealing temperatures and durations, were varied to change the microstructure of the films. The functional response of the films was characterized before and after exposure to gamma-radiation (up to 10 Mrad(Si)). Within the total ionization dose studied, all films showed <5% change in dielectric response and polarization, and <15% change in piezoelectric response, after irradiation. While all films showed substantial radiation tolerance, those with large, columnar grains showed the highest dielectric and piezoelectric response, and therefore, might offer the best approach for enabling piezoelectric MEMS devices for applications in radiative environments.

6.2 Introduction

Ferroelectric perovskites exhibit, in addition to a switchable polarization under an applied electric field, high dielectric, pyroelectric and piezoelectric properties. The high electromechanical response makes them ideal for use in micro-electro-mechanical system (MEMS) devices that require long actuating strokes, or high sensing capabilities.[1,92] The demand for devices with smaller footprints and higher functional capabilities has increased over the last couple of decades. Similarly, there is growing interest in utilizing MEMS sensors and actuators in more demanding environments - e.g., aerospace, medical physics tools, monitoring systems for nuclear facilities or disaster areas - requiring materials with good radiation tolerance. Lead zirconate titanate (PZT) thin films are currently one of the most studied ferroelectrics with a relatively high radiation tolerance compared to many electronic materials, including many semiconductors. However, PZT still suffers large degradation when exposed to ionizing radiation at or above 5 Mrad(Si), showing up to 30% degradation in dielectric and piezoelectric response after irradiation.[40,50,51] In this work, relaxor-ferroelectric $0.7Pb(Mg_{1/3}Nb_{2/3})O_3$-$0.3PbTiO_3$ (PMN-PT) is explored as an alternative material for radiation tolerant piezoelectric MEMS devices.

Radiation exposure can generate defects in materials through two primary events: ionization and displacement. In ionization events, the incident radiation interacts with the electrons of the material, generating electron-hole pairs and, subsequently, trapped charges. This type of interaction occurs with all charged particles and high-energy photons, and is the primary interaction of gamma irradiation.[111] Additionally, massive particles (electrons, ions, and neutrons) also interact with the atomic nuclei of the material which can lead to displacement of the atom from the lattice creating vacancy-interstitial pairs and eventually amorphization.[34,94] Hence, radiation exposure can greatly affect the defect landscape of a material, and therefore its properties. In ferroelectric materials, defects can affect functional response not only through intrinsic changes, but also by modifying the domain wall mobility. Domain wall motion is indeed a major contributor to the dielectric and piezoelectric response of ferroelectric materials.[3] Previous gamma irradiation studies on ferroelectrics such as PZT have shown that mobile electrons generated by ionizing radiation can combine with pre-existing oxygen vacancies, $V_O^{\cdot\cdot} + e^- \rightarrow V_O^{\cdot}$, generating more mobile, singly charged oxygen vacancies. In the presence of an electric field, either built-in or externally applied, oxygen vacancies can accumulate and self-order within the material, often at electrode-ferroelectric and eventual internal interfaces, leading to fatigue-like degradation in the functional response.[26,52] It has been reported that chemical doping can increase the radiation tolerance of PZT through creation of defect-dipoles. However, defect dipoles can reduce the functional response by pinning domain walls and suppressing domain wall mobility.[49] PMN-PT has been recently reported as an alternative ferroelectric solid solution with high functional response and high radiation tolerance.[91] Specifically, PMN-PT thin films were found to have < 5% degradation in dielectric and polarization response, and <10% degradation in piezoelectric response after gamma-radiation exposure up to 10 Mrad(Si). However, microstructural features of the PMN-PT thin films, might have a major influence on the radiation tolerance of the films. On one hand, grain boundaries can act as regions which increase the number of radiation-induced defects through cascade events.[112] On the other hand, grain boundaries can also act as defect sinks, as has been found in various ferroelectric studies, and hence a greater grain boundary density could also potentially increase radiation tolerance.[108,113,114] Here we study in more detail the effects of changes in the processing parameters, and hence the resulting microstructural features (e.g., grain size and porosity), on the ionizing radiation tolerance of PMN-PT films.

6.3 Experimental Procedure

0.7PMN-0.3PT thin films were processed via chemical solution deposition (CSD).

A 0.3 M solution with 40% excess Pb content was prepared using a 2-methoxyethanol route similar to those described by Park *et al*. and Bastani *et al.*.[56,58] The films were deposited by spin coating onto platinized silicon wafers: Si / SiO_2 (2000 nm) / TiO_2 (35 nm) / Pt (100 nm). A 20 nm-thick seed layer of $PbTiO_3$ was deposited by CSD to induce (001) orientation in the PMN-PT thin films.[96] Three different processing parameter sets were used to obtain films of varying microstructure, using a hotplate for drying and pyrolysis steps, and a rapid thermal annealer for crystallization. Samples *A* were processed using a recipe described by Keech et al. with a higher thermal budget allocated for the drying and pyrolysis steps: the solution was spin-coated onto the substrates at 2500 rpm for 45 seconds, dried at 250 °C for 2 minutes, pyrolyzed at 430 °C for 5 minutes, and crystallized at 700 °C for 1 minute.[59] In contrast, Samples *B* were processed with a higher thermal budget for the annealing step: they were spin-coated at 3000 rpm for 30 seconds, dried at 250 °C for 1 minute, pyrolyzed at 400 °C for 5 minutes, and crystallized at 800 °C for 1 minute. Samples *C* were processed with an adjusted recipe of Samples *B* to test a multi-layer annealing process: these samples were spin-coated at 3000 rpm for 30 seconds, dried at 250 °C for 1 minute, pyrolyzed at 400 °C for 5 minutes, and crystallized at 800 °C for 2 minutes. However, while drying and pyrolysis steps were performed for every deposited layer of film, the crystallization was performed only every three layers. The processes described above were repeated until all samples reached a thickness of ~500 nm.

Cross-sectional scanning electron microscopy (SEM) (Hitachi SU8230 FE-SEM) imaging was used to characterize the microstructure of the films. X-ray diffraction (XRD) (PANalytical Alpha-1) scans were used to confirm the crystallographic phase and orientation of the films. Circular Pt top electrodes (500 μm diameter and 80 nm thick) were deposited onto the surface by sputtering and patterned via lift-off. Seven samples for each set were irradiated at different doses between 0.1 Mrad(Si) and 10 Mrad(Si) using a ^{60}Co source at a rate of ~400 rad(Si)/s in the US Naval Research Laboratory (NRL). One additional sample for each set was sent to NRL but not irradiated, and used as control for factors including sample shipment and aging. The functional response of the samples was characterized on the same electrodes before and after irradiation, with five to eight electrodes tested on each sample, and the change was recorded as a measure of radiation tolerance. The measurements were taken in the following order, approximately from the lowest to the highest field: low-field dielectric permittivity and loss (100 mV, 1 kHz, Agilent 4284A LCR meter); polarization-electric field hysteresis loops (300 kV/cm, 100 Hz sine wave, Radiant P-PM2); nonlinear dielectric permittivity (up to 10 kV/cm AC, 1 kHz, aixACCT); DC electric field-dependent permittivity, i.e. dielectric tunability (up to 150 kV/cm DC, with overlapping 100 mV AC signal; aixACCT double beam laser interferometer); and electric field-dependent converse, effective longitudinal piezoelectric response (up to 150 kV/cm DC, with overlapping 1 V AC signal, aixACCT DBLI). This characterization order was chosen consistently with previous reports, for ease of comparison of the results, as well as to have minimal exposure of the films to higher electric fields.[26,49,114]

6.4 Results and Discussion

X-ray diffraction (Figure 6-1a) revealed preferential 001-crystallographic orientation in all films with Lotgering factors >95%.[86] Cross-sectional SEM (Figure 6-1b) showed significant microstructural differences between the three samples. Samples *A*, with a relatively larger thermal budget allocated to drying and pyrolysis, had small, densely stacked grains about 100 to 300 nm in size. Samples *B* and *C*, with higher crystallization temperatures, showed larger and more columnar grains than samples *A*. Samples *B* had grain sizes from 500 nm to 1 μm, columnar grain growth, and showed some amount of porosity within the grains. Samples *C* had grain sizes from 300 nm to 1 μm, mixed columnar and stacked grain growth, and appeared to show limited pores within the grains.

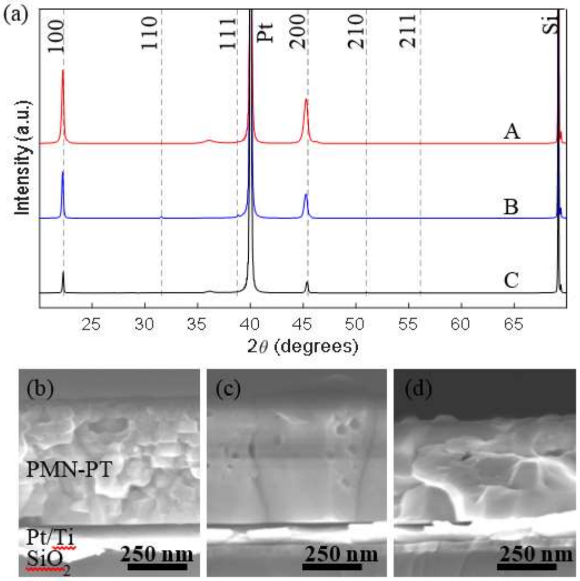

Figure 6-1 (a) Representative XRD scans of samples *A* (red), *B* (blue), and *C* (black), (b) cross-sectional SEM image of samples *A*, (c) cross-sectional SEM image of samples *B*, (d) cross-sectional SEM image of samples *C*.

Table 6-1, Table 6-2, and Table 6-3 report the virgin and post irradiation functional response for all samples. The error bars represent the standard deviation in measurements found across the electrodes studied for each sample. Samples *A* had an average low-field dielectric permittivity (ε_r)of ~1100 and dielectric loss, tan(δ), of 2% at 1 kHz; dielectric tunability, calculated as the percent difference of the maximum and minimum permittivities of the permittivity-field curves, of 65%; saturated polarization (P_{sat}) of ~27 μC/cm^2; and saturated effective longitudinal piezoelectric coefficient ($d_{33,f,sat}$) of ~55 pm/V. In contrast, samples *B* showed overall higher responses than samples *A* across the board, with ε_r of ~1800; tan(δ) of 3%; dielectric tunability of ~75%, P_{sat} of ~38 μC/cm^2; and $d_{33,f,sat}$ of ~80 pm/V. Samples *C* showed intermediate values of the same parameters, between samples A and B, with ε_r of ~1400; tan(δ) of 1%; dielectric tunability of ~75%; P_{sat} of ~37 μC/cm^2; and $d_{33,f,sat}$ of ~75 pm/V. Overall, samples *B* showed the highest functional response, samples *A* showed the lowest, and samples *C* showed responses in between these two. It is possible that the larger grain size of samples *B* is what enables the higher functional response: a larger grain size often allows for greater domain wall mobility and thus leads to greater functional response, as has been observed in the literature on other ferroelectric thin films.[89,115] This correlation is indeed consistent with the observed dielectric extrinsic contributions from domain walls, i.e. the irreversible Rayleigh parameter (α). Samples *A*, with the smallest grains, had the lowest α at ~11 cm/kV, while samples *B*, with the largest grains, had the highest value at ~23 cm/kV.

Table 6-1 Functional response of samples *A* before and after gamma-ray irradiation. 0 Mrad(Si) represents the control sample.

Samples *A*		0 Mrad	0.1	0.2	0.5	1.0	2.0	5.0	10.0
ε_r	Virgin	1071 ± 10	1056 ± 20	1074 ± 20	1056 ± 10	1091 ± 10	1091 ± 8	1073 ± 10	1073 ± 10
	Irradiated	1057 ± 10	1049 ± 20	1073 ± 10	1073 ± 10	1096 ± 10	1105 ± 20	1073 ± 10	1072 ± 10
ε_{init}	Virgin	1124 ± 5	1127 ± 10	1131 ± 5	1114 ± 20	1141 ± 10	1152 ± 4	1123 ± 10	1122 ± 5
	Irradiated	1100 ± 5	1111 ± 20	1085 ± 20	1098 ± 10	1124 ± 10	1130 ± 20	1090 ± 20	1100 ± 30
α (cm/kV)	Virgin	10 ± 1	11 ± 1	11 ± 1	12 ± 1	11 ± 1	12 ± 1	10 ± 1	12 ± 1
	Irradiated	11 ± 1	10 ± 1	12 ± 1	11 ± 1	11 ± 1	11 ± 1	10 ± 1	11 ± 1
$\alpha/\varepsilon_{init}$ (cm/kV) (E-3)	Virgin	9.1 ± 0.1	9.3 ± 0.1	9.5 ± 0.2	10.9 ± 0.8	9.8 ± 0.2	10.5 ± 0.4	9.2 ± 0.2	10.3 ± 0.2
	Irradiated	9.9 ± 0.2	9.4 ± 0.1	10.7 ± 0.9	9.8 ± 0.2	9.9 ± 0.4	9.5 ± 0.4	9.4 ± 0.6	9.8 ± 0.6
P_{sat} ($\mu C/cm^2$)	Virgin	27 ± 0.1	27 ± 0.2	27 ± 0.3	27 ± 0.1	27 ± 0.1	27 ± 0.1	27 ± 0.2	27 ± 0.2
	Irradiated	27 ± 0.1	27 ± 0.2	27 ± 0.3	27 ± 0.1	27 ± 0.1	27 ± 0.1	27 ± 0.2	27 ± 0.2
$P_{rem,pos}$ ($\mu C/cm^2$)	Virgin	4.6 ± 0.2	4.2 ± 0.1	4.5 ± 0.2	3.9 ± 0.1	4.3 ± 0.2	4.4 ± 0.2	4.4 ± 0.1	4.4 ± 0.3
	Irradiated	4.6 ± 0.2	4.2 ± 0.1	4.5 ± 0.2	3.8 ± 0.1	4.3 ± 0.2	4.3 ± 0.2	4.4 ± 0.1	4.4 ± 0.3
$P_{rem,neg}$ ($\mu C/cm^2$)	Virgin	-7.9 ± 0.2	-7.5 ± 0.1	-7.6 ± 0.3	-7.2 ± 0.1	-7.5 ± 0.2	-7.6 ± 0.1	-7.6 ± 0.3	-7.6 ± 0.2
	Irradiated	-7.9 ± 0.2	-7.5 ± 0.1	-7.6 ± 0.3	-7.4 ± 0.1	-7.5 ± 0.2	-7.7 ± 0.1	-7.6 ± 0.3	-7.7 ± 0.1
Dielectric tunability	Virgin	65 ± 0.2	65 ± 0.3	65 ± 0.1	65 ± 0.2	65 ± 0.5	65 ± 0.2	65 ± 0.2	65 ± 0.2
	Irradiated	67 ± 1	65 ± 0.2	68 ± 2	65 ± 0.3	65 ± 0.6	68 ± 3	64 ± 0.4	72 ± 10
$d_{33,f,sat}$ (pm/V)	Virgin	56 ± 3	55 ± 2	53 ± 2	55 ± 2	57 ± 4	55 ± 3	51 ± 4	54 ± 5
	Irradiated	54 ± 2	51 ± 3	53 ± 2	53 ± 2	52 ± 3	56 ± 3	53 ± 2	51 ± 3
$d_{33,f,rem,pos}$ (pm/V)	Virgin	26 ± 8	22 ± 4	22 ± 1	20 ± 3	21 ± 3	22 ± 2	21 ± 3	20 ± 5
	Irradiated	19 ± 6	15 ± 5	16 ± 2	18 ± 2	18 ± 3	20 ± 3	17 ± 1	16 ± 1
$d_{33,f,rem,neg}$ (pm/V)	Virgin	2 ± 5	-3 ± 5	2 ± 2	-1 ± 5	2 ± 4	2 ± 3	-2 ± 4	-1 ± 4
	Irradiated	2 ± 3	-3 ± 1	1 ± 2	-2 ± 4	-1 ± 2	2 ± 1	2 ± 2	0 ± 2

Table 6-2 Functional response of samples *B* before and after gamma-ray irradiation. 0 Mrad(Si) represents the control sample.

Samples *B*		0 Mrad	0.1	0.2	0.5	1.0	2.0	5.0	10.0
ε_r	Virgin	1815 ± 70	1734 ± 30	1796 ± 30	1908 ± 40	1826 ± 20	1787 ± 50	1756 ± 10	1764 ± 20
	Irradiated	1816 ± 74	1740 ± 30	1797 ± 20	1808 ± 10	1832 ± 10	1732 ± 30	1721 ± 10	1717 ± 20
ε_{init}	Virgin	1955 ± 60	1872 ± 20	1933 ± 20	1941 ± 10	1957 ± 10	1896 ± 20	1891 ± 10	1895 ± 10
	Irradiated	1914 ± 60	1832 ± 30	1890 ± 30	1896 ± 10	1922 ± 10	1829 ± 40	1827 ± 10	1799 ± 40
α (cm/kV)	Virgin	23 ± 4	23 ± 3	26 ± 1	24 ± 2	27 ± 2	20 ± 1	24 ± 1	24 ± 1
	Irradiated	24 ± 3	23 ± 2	26 ± 1	24 ± 1	26 ± 2	21 ± 1	24 ± 1	24 ± 1
$\alpha/\varepsilon_{init}$ (cm/kV) (E-3)	Virgin	11.9 ± 1	12.3 ± 1	13.3 ± 0.3	12.2 ± 0.9	13.8 ± 1	10.5 ± 0.3	12.8 ± 0.5	12.8 ± 0.6
	Irradiated	12.3 ± 1	12.5 ± 0.9	13.5 ± 0.5	12.6 ± 0.7	13.5 ± 0.9	11.5 ± 0.7	12.9 ± 0.4	13.2 ± 0.7
P_{sat} ($\mu C/cm^2$)	Virgin	38 ± 0.9	38 ± 0.3	38 ± 0.1	38 ± 0.2	38 ± 0.2	38 ± 0.2	37 ± 0.2	37 ± 0.2
	Irradiated	38 ± 1	37 ± 0.4	36 ± 1	36 ± 2	37 ± 3	35 ± 2	36 ± 2	37 ± 0.3
$P_{rem,pos}$ ($\mu C/cm^2$)	Virgin	11 ± 0.4	11 ± 0.5	11 ± 0.2	11 ± 0.2	11 ± 0.2	11 ± 0.1	11 ± 0.3	11 ± 0.1
	Irradiated	11 ± 0.6	10 ± 0.4	10 ± 1	10 ± 0.2	11 ± 0.4	10 ± 0.7	10 ± 0.5	10 ± 0.3
$P_{rem,neg}$ ($\mu C/cm^2$)	Virgin	-10 ± 0.7	-10 ± 0.8	-10 ± 0.1	-11 ± 3	-10 ± 0.5	-10 ± 0.1	-10 ± 0.4	-10 ± 0.3
	Irradiated	-12 ± 3	-12 ± 3	-14 ± 3	-11 ± 0.2	-13 ± 3	-11 ± 3	-11 ± 3	-12 ± 3
Dielectric tunability	Virgin	73.6 ± 0.7	73.3 ± 0.4	74.4 ± 0.7	74.0 ± 0.4	74.5 ± 0.3	73.1 ± 0.6	74.1 ± 0.5	73.9 ± 20
	Irradiated	73.3 ± 0.5	73.3 ± 0.2	74.0 ± 0.3	74.3 ± 0.2	74.3 ± 0.2	73.2 ± 0.6	73.8 ± 0.1	73.9 ± 0.2
$d_{33,f,sat}$ (pm/V)	Virgin	70 ± 3	75 ± 3	70 ± 4	67 ± 5	70 ± 8	68 ± 4	71 ± 2	72 ± 2
	Irradiated	72 ± 4	72 ± 2	68 ± 3	78 ± 4	73 ± 2	69 ± 2	66 ± 7	71 ± 3
$d_{33,f,rem,pos}$ (pm/V)	Virgin	38 ± 2	40 ± 4	32 ± 6	33 ± 3	34 ± 6	38 ± 5	38 ± 1	34 ± 5
	Irradiated	40 ± 5	38 ± 4	34 ± 3	45 ± 12	36 ± 5	40 ± 2	34 ± 3	40 ± 6
$d_{33,f,rem,neg}$ (pm/V)	Virgin	15 ± 3	15 ± 1	13 ± 3	14 ± 3	15 ± 2	13 ± 3	15 ± 3	14 ± 2
	Irradiated	16 ± 3	11 ± 4	13 ± 2	13 ± 5	15 ± 7	14 ± 4	15 ± 2	11 ± 2

Table 6-3 Functional response of samples C before and after gamma-ray irradiation. 0 Mrad(Si) represents the control sample.

Samples *C*		0 Mrad	0.1	0.2	0.5	1.0	2.0	5.0	10.0
ε_r	Virgin	1491 ± 30	1405 ± 20	1418 ± 20	1453 ± 10	1385 ± 10	1549 ± 20	1521 ± 30	1382 ± 10
	Irradiated	1556 ± 30	1502 ± 30	1495 ± 50	1515 ± 10	1439 ± 10	1612 ± 30	1556 ± 30	1418 ± 20
ε_{init}	Virgin	1766 ± 30	1728 ± 40	1707 ± 100	1740 ± 10	1618 ± 50	1835 ± 20	1819 ± 40	1642 ± 10
	Irradiated	1761 ± 20	1677 ± 30	1695 ± 40	1705 ± 10	1628 ± 10	1819 ± 30	1792 ± 40	1570 ± 70
α (cm/kV)	Virgin	14 ± 1	13 ± 1	12 ± 3	13 ± 1	12 ± 1	15 ± 1	13 ± 1	13 ± 1
	Irradiated	14 ± 1	13 ± 1	13 ± 1	13 ± 1	12 ± 1	15 ± 1	14 ± 1	12 ± 1
$\alpha/\varepsilon_{init}$ (cm/kV) (E-3)	Virgin	8.1 ± 0.5	7.5 ± 0.2	7.2 ± 1	7.6 ± 0.1	7.7 ± 0.7	8.1 ± 0.2	7.4 ± 0.2	8.0 ± 0.3
	Irradiated	8.1 ± 0.2	7.8 ± 0.1	7.3 ± 0.4	7.7 ± 0.1	7.5 ± 0.1	8.4 ± 0.2	7.8 ± 0.3	7.9 ± 0.7
P_{sat} (μC/cm^2)	Virgin	38 ± 0.2	37 ± 0.5	37 ± 0.4	37 ± 0.2	36 ± 0.3	38 ± 0.5	38 ± 0.5	34 ± 3
	Irradiated	37 ± 0.4	36 ± 0.3	35 ± 0.3	37 ± 0.2	36 ± 0.3	37 ± 1	37 ± 3	35 ± 0.5
$P_{rem,pos}$ (μC/cm^2)	Virgin	12 ± 0.3	12 ± 0.2	12 ± 0.1	12 ± 0.2	8.6 ± 0.2	10 ± 2	12 ± 0.5	11 ± 1
	Irradiated	12 ± 0.4	11 ± 0.2	11 ± 0.2	11 ± 0.5	11 ± 0.6	12 ± 1	12 ± 2	11 ± 0.5
$P_{rem,neg}$ (μC/cm^2)	Virgin	-12 ± 3	-11 ± 0.3	-12 ± 3	-12 ± 2	-13 ± 0.3	-14 ± 2	-12 ± 2	-13 ± 3
	Irradiated	-13 ± 3	-11 ± 0.1	-12 ± 3	-13 ± 3	-12 ± 2	-13 ± 2	-11 ± 0.5	-12 ± 3
Dielectric tunability	Virgin	74.6 ± 0.3	72.5 ± 0.2	71.9 ± 2	73.9 ± 0.3	78.6 ± 3	78.2 ± 1.6	75.1 ± 1	74.2 ± 1
	Irradiated	73.8 ± 0.2	72.4 ± 0.3	72.4 ± 0.7	72.9 ± 0.2	71.9 ± 0.3	74.9 ± 0.3	74.4 ± 0.4	71.4 ± 0.2
$d_{33,f,sat}$ (pm/V)	Virgin	68 ± 4	73 ± 3	71 ± 6	68 ± 3	65 ± 9	71 ± 3	65 ± 10	73 ± 2
	Irradiated	69 ± 4	62 ± 3	70 ± 2	68 ± 5	65 ± 1	72 ± 3	62 ± 4	63 ± 6
$d_{33,f,rem,pos}$ (pm/V)	Virgin	42 ± 3	46 ± 3	47 ± 5	40 ± 2	37 ± 8	45 ± 2	38 ± 8	45 ± 4
	Irradiated	41 ± 6	39 ± 2	45 ± 2	42 ± 4	39 ± 2	45 ± 7	41 ± 2	40 ± 7
$d_{33,f,rem,neg}$ (pm/V)	Virgin	13 ± 2	12 ± 5	13 ± 4	12 ± 3	12 ± 4	15 ± 1	13 ± 1	12 ± 4
	Irradiated	13 ± 3	7 ± 4	13 ± 2	12 ± 3	12 ± 1	15 ± 4	14 ± 2	12 ± 5

Figure 6-2 shows the percent degradation of various functional parameters as a function of radiation dose: a positive value indicates degraded response and a negative value represents enhanced response. The error bars represent the standard deviation in the percent degradation found across the electrodes studied for each sample. The changes in low-field dielectric permittivity at 10 Mrad for each sample were 0%, 3%, and -2% for samples *A*, *B*, and *C*, respectively. These observed changes are small since they are comparable to one standard deviation of the measurements, indicating that the microstructure has little influence on the radiation tolerance of the dielectric permittivity of these films. As all three samples exhibit limited changes in response, the radiation tolerance of the PMN-PT films with respect to dielectric permittivity remains high regardless of the microstructure of the thin films.

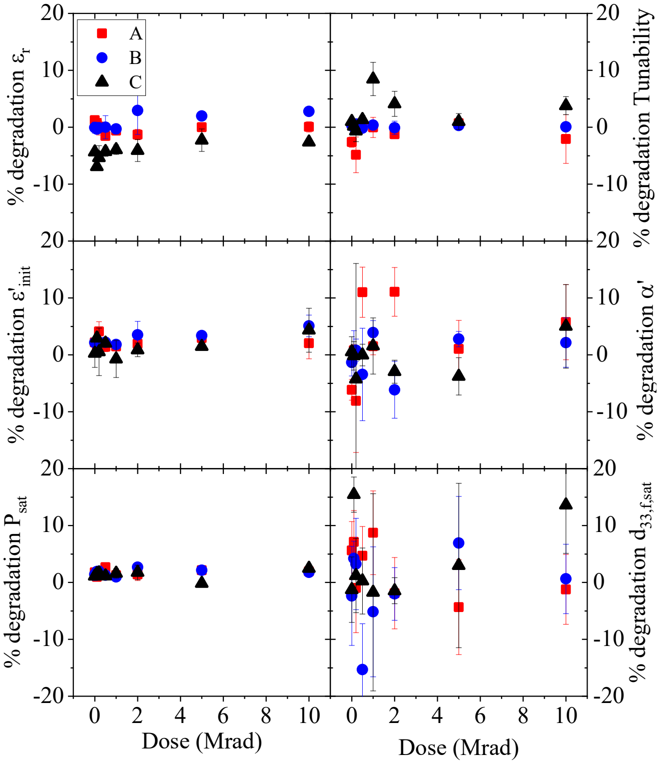

Figure 6-2 Percent degradation of functional response of samples *A* (red), *B* (blue), and *C* (black) exposed up to 10 Mrad(Si). The responses shown are dielectric permittivity (top left), dielectric tunability (top right), reversible Rayleigh parameter (middle left), irreversible Rayleigh parameter (middle right), saturated polarization (bottom left), and saturated effective piezoelectric coefficient (bottom right).

The reversible Rayleigh parameter, ε_{init}, showed relatively small changes as well, with degradation of 2%, 5%, and 4% for samples *A*, *B*, and *C*, respectively at 10 Mrad, with similar or lower degradation across all other TID values. The irreversible Rayleigh parameter, *α*, also showed small changes at 10 Mrad, with 6%, 2%, and 5% degradation for samples *A*, *B*, and *C*, respectively. However, larger changes were observed at lower doses. Samples *A* showed up to 12% degradation at doses of 0.5 Mrad and 2 Mrad. While these percent changes seem significant, upon closer inspection of the irreversible Rayleigh parameters in Tables 6-1 to 6-3, the parameter changed from 12 cm/kV before irradiation to 11 cm/kV after irradiation. With one standard deviation of 1 cm/kV in these measurements, this is not in fact a significant change. Similarly, samples *B* showed a 6% improvement after irradiation at 2 Mrad corresponding to a change in parameter from 20 cm/kV to 21 cm/kV, and samples *C* showed a 5% improvement after irradation at 5 Mrad corresponding to a change in parameter from 13 cm/kV to 14 cm/kV, both of which are within the measured standard deviation. It is possible these improvements at low doses of radiation indicate that radiation-induced electrons initially combine with pre-existing defects in the film that previously hindered domain wall motion. Such recombination can result in lower thresholds for domain wall (vibration and) motion activation. At increasing doses, radiation-induced defects will eventually accumulate beyond those accommodated by pre-existing defects, and ultimately degrade the material's response. However, the limited changes found in α' suggests that while the microstructure appears to influence the overall domain wall mobility, it does not result in any significant variation of these extrinsic contributions upon exposure to ionizing radiation. This behavior suggests that the radiation tolerance of PMN-PT is not due simply to increased domain wall mobility in this material system, given that all three samples show similar radiation tolerance, and that the irreversible Rayleigh parameter is lower in these films than in PZT thin films previously studied (with reported values between 26 and 36 cm/kV).[49,114] However, we also note that literature reports of typical α values for PZT thin films are much lower than those reported in Brewer et al., and often between 7 and 15 cm/kV, which are fully comparable to those of the PMN-PT films reported here.[20,47,116] While the PZT films of the Brewer *et al.* studies showed higher extrinsic responses than the PMN-PT films studied here, the functional response of the PMN-PT films were still either equivalent to or greater than those of the PZT films which exhibited dielectric response of ~1000 and piezoelectric responses between 50 and 68 pV/m. Since the extrinsic contributions are not a significant contributor to either the functional response or radiation tolerance of the PMN-PT films, other factors inherent to PMN-PT, such as the chemical heterogeneities present, may be of more significance.

Polarization measurements showed similarly high radiation tolerance as the dielectric permittivity, with 0%, 2%, and 2% change after 10 Mrad in P_{sat} for samples *A*, *B*, and *C*, respectively. This minimal change in P_{sat} is observed for the full range of the TID studied. The films also showed high radiation tolerance for remanent polarization, which showed changes of only up to 2 $\mu C/cm^2$ in either degradation or healing across all doses. Figure 6-3 shows the polarization-electric field hysteresis loops before and after irradiation at 10 Mrad(Si) for samples *A*, *B*, and *C*. Samples *A* showed significantly lower overall polarization response than samples *B* and *C*, consistent with the previous observation of lower domain wall mobility in the former samples. Samples C showed high polarization response similar to samples *B*, however, they also exhibited lossier behavior before irradiation. While it is difficult to pinpoint direct causes for lossy behavior, it is possible that the lossier behavior of samples *C* is due to a difference in the grain structure and how defects within the material may accumulate around grain boundaries.[117]

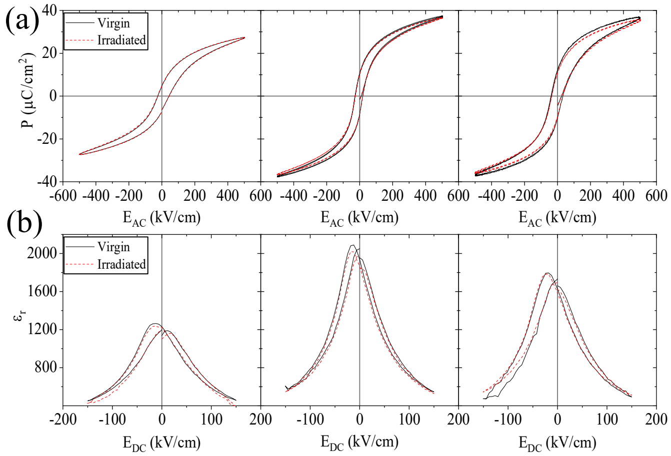

Figure 6-3 Virgin (black) and 10 Mrad irradiated (red) functional curves of samples A (left column), B (middle column), and C (right column). Functional curves shown are Rayleigh analysis (top row), polarization-field (middle row), and permittivity-field (bottom row).

Changes of -2%, 0%, and 4% were observed for dielectric tunability of the films after irradiation at 10 Mrad for samples *A*, *B*, and *C*, respectively: all values are once again within the measurement's standard deviation. Figure 6-2 shows slightly larger amounts of degradation for samples *C* at doses of 1 and 2 Mrad, i.e., up to 9%. However, these changes are within one standard deviation between doses of 1 Mrad and 10 Mrad. Overall, samples B showed the highest functional response, while maintaining similarly high radiation tolerance as the other samples at 10 Mrad (Figure 6-3). Looking closely at the tunability curves in Figure 6-3, it is evident that the most substantial reductions in the dielectric permittivity are found at low electric fields, close to the coercive values where changes to the extrinsic contributions are due not only to domain wall motion but also more prominently to the nucleation and growth of domains of polarity well aligned to the applied

DC electric field. At higher fields, deviations between the response of the irradiated and virgin films are somewhat limited. Similarly, at decreasing field amplitude, the return branch shows substantially smaller changes in the dielectric permittivity than those observed in the increasing field branches. The above features suggest that the radiation-induced defects are of relatively low pinning energy, easily overcome by the field-induced domain nucleation and growth processes, and that application of high DC fields can reduce the effects that these defects have on the material's functional response.

The effective piezoelectric response of the samples showed the highest amount of degradation in this TID study. Specifically, samples *C* exhibited 14% degradation of $\mathrm{d}_{33,\mathrm{f,sat}}$ at 10 Mrad. However, samples *A* and *B*'s observed degradation of the same parameter was limited to -1% and 1% change, respectively. While such difference in behavior would indicate that samples *A* and *B* have significantly higher radiation tolerance in $d_{33,\mathrm{f,sat}}$ than samples *C*, $d_{33,\mathrm{f,sat}}$ degradation of up to 9% and 7% were found at lower doses in samples *A* and *B*, respectively. We note that the piezoelectric measurements also showed large standard deviations in measurements, of up to 8%, 11%, and 17% for one standard deviation in the $d_{33,\mathrm{f,sat}}$ measurements for samples *A*, *B*, and *C*, respectively. This means that there is also larger variability in the measurement of $d_{33,\mathrm{f,sat}}$, which may be a cause for the larger changes observed after irradiation compared to the other measurements studied. Figure 6-4 shows a comparison of the virgin and irradiated piezoelectric curves of samples *A*, *B*, and *C* for the control, 1 Mrad, and 10 Mrad TID, showing high radiation tolerance across all three samples. Samples *B* offer the greatest piezoelectric response, while also exhibiting possible enhancement of response at low doses, as shown in the film exposed to

1 Mrad of radiation, and in the 15% increase in $d_{33,\mathrm{f,sat}}$ found at 0.5 Mrad. While the mechanisms responsible for radiation-induced healing and degradation in ferroelectrics are not yet well understood, it is possible that at smaller TID, the radiation-induced defects might annihilate pre-existing defects, thus leading to enhanced response in the irradiated films. The microstructure may also play a role in where these radiation-induced defects collect within the material. Since grain boundaries can act as defect sinks, the concentration as well as the location of these grain boundaries may influence how the material responds to radiation exposure.[118] Specifically, samples *A* with the stacked grains have a much larger concentration of grain boundaries across the film thickness. Trapped charges, accumulated at these internal interfaces, can therefore create localized in series capacitors with degraded ferroelectric properties. In samples *B*, radiation- induced charges accumulating at the grain boundary would result in parallel capacitors with degraded ferroelectric properties, based on the columnar grain structure. Since samples *B* are less likely to accumulate radiation-induced defects throughout the thickness of the film, it is subsequently able to maintain its $d_{33,\mathrm{f,sat}}$ after irradiation. In samples *C*, the columnar grain structure does not appear as well defined as in samples *B*. Similarly as with samples *A*, samples *C* may not be able to maintain its $d_{33,\mathrm{f,sat}}$ due to the location of its grain boundaries.

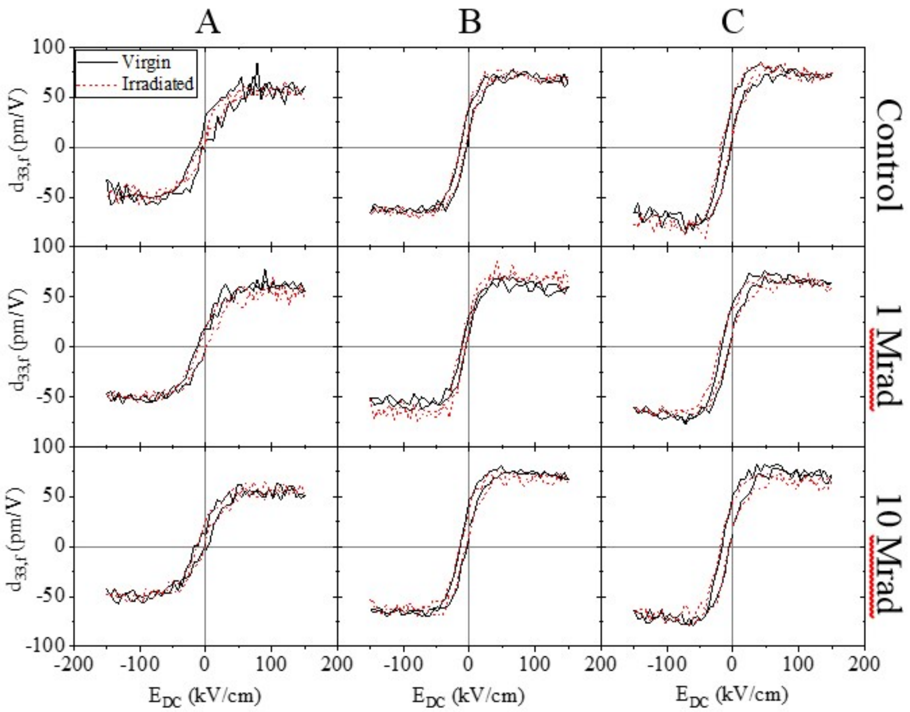

Figure 6-4 Virgin (black) and irradiated (red) effective piezoelectric curves of samples A (left column), B (middle column), and C (right column). Radiation doses shown include the control (top row), 1 Mrad (middle row), and 10 Mrad (bottom row).

6.5 Conclusions

In summary, PMN-PT thin films were investigated to determine the role of microstructure on their radiation tolerance. While it was shown that large, columnar grains led to higher overall functional response, the microstructure had very limited effect on the radiation tolerance of the dielectric and polarization responses, with changes within one standard deviation of the measurements up to 10 Mrad(Si). Larger changes were observed in piezoelectric response of the PMN-PT thin films, and the samples with large, columnar grains showed not only greater radiation tolerance but also evidence of enhancement in response. While microstructure may play a role in maintaining piezoelectric response in PMN-PT films, it is likely that many other factors also contribute to PMN-PT's radiation tolerance, such as the chemical heterogeneities present. The high functional response as well as high radiation tolerance makes PMN-PT an attractive option for designing next generation radiation-hard devices.

6.6 Acknowledgements

This work was supported by the Defense Threat Reduction Agency, Basic Research Award No. HDTRA 1-15-1-0035 to Georgia Institute of Technology. The contents do not necessarily reflect the position or the policy of the federal government, and no official endorsement should be inferred. The authors gratefully acknowledge Joel Martin of the Army Research Laboratory and Steven Isaacson of General Technical Services for providing platinized Si substrates for this work.

CHAPTER 7. PROCESSING-STRUCTURE-PROPERTY RELATIONS OF RADIATION TOLERANCE OF HZO THIN FILMS

At the time of this publication, the contents of this chapter are being prepared to be submitted to a peer-reviewed journal.

7.1 Summary

This work investigates the radiation tolerance of $Hf_{0.5}Zr_{0.5}O_2$ (HZO) thin films, processed via plasma-enhanced atomic layer deposition (PEALD) and thermal atomic layer deposition (THALD). The functional response of the films were characterized before and after exposure to gamma-radiation with total ionization dose (TID) up to 5 Mrad(Si). Both sets of films showed significant total degradation in polarization response up to 31% in the PEALD samples and up to 50% in THALD samples. Substantial changes were also seen in the aged control samples in PEALD and THALD samples, suggesting that less than 5% and 20% respectively of the overall degradation was due to the radiation effects.The PEALD samples showed less than 5% change in remanent polarization between control samples (not exposed to the radiation source) and all doses studied, while the THALD samples showed up to 30% changes between the controls and doses studies. These results suggest that aging effects remain a major concern in hafnia-based ferroelectric thin films. Additionally, the PEALD processed films show greater radiation tolerance than THALD processed ones, making them possible candidates for use in memory devices for radiation-hostile environments.

7.2 Introduction

Due to their spontaneous, switchable polarization, ferroelectric materials can be used in nonvolatile memory devices. The demand for nanoscale devices has increased the need for new material systems which can provide the same functionality at a fraction of the size. $Hf_xZr_{1-x}O_2$ thin films have been of increasing interest for these applications due to their high ferroelectric properties in thin films at only a few nanometers thick, as well as compatibility with CMOS technologies, promising full integration.

The highest ferroelectric properties in $Hf_xZr_{1-x}O_2$ thin films has been found at x ~ 0.5, near the morphotropic phase boundary between the tetragonal (t-phase) and orthorhombic (o-phase) phase of the material.[65–69] Extensive research using thermal atomic layer deposition (THALD) has enabled fabrication of ferroelectric $Hf_{0.5}Zr_{0.5}O_2$ (HZO) through post annealing temperatures as low as 370 °C.[74,119] However, these films require substantial wake-up (field cycling under applied electric field to further induce the ferroelectric phase within the material).[71] Recent studies have demonstrated an alternative fabrication technique, plasma-enhanced atomic layer deposition (PEALD), resulting into ferroelectric HZO films with post-deposition annealing temperatures of only 300 °C, while also reducing the wake-up effect, making PEALD a particularly attractive method for optimized fabrication of ferroelectric HZO thin films.[78]

The sporadic literature reports on the radiation tolerance of THALD HZO films has indicated possible radiation tolerance comparable with other ferroelectrics. The most recent study by Sun *et al.* revealed THALD processed HZO thin films post annealed at 550 °C with relatively high radiation tolerance against gamma irradiation, <5\% degradation in polarization properties up to a dose of 10 Mrad(Si), showcasing the material's promising applications for radiative environments such as aerospace or nuclear reactor monitoring.[81] This work aims to explore the radiation tolerance of HZO films fabricated via plasma enhanced compared to thermal ALD to evaluate their viability for radiation environment applications.

7.3 Experimental Procedures

PEALD and THALD processed $Hf_{0.5}Zr_{0.5}O_2$ films were fabricated as described by Hur *et al.*.[120] After atomic layer deposition, both films were post-annealed at 400 °C. The thin film stack was comprised of Si / TiN (12 nm) / HZO (10 nm) / TiN (12 nm) / Al (100 nm). Square electrodes etched to dimensions of 100 μm x 100 μm were used for electrical characterization.

A single wafer from each fabrication process was cleaved into 8 equivalent samples. The pristine PEALD and THALD films were cycled 1000 and 2000 times, respectively, with a sinusoidal wave at 1 kHz up to 2.5 V to ensure full wake up. After wake-up, the polarization-electric field (P-E) and switching current loops (I-E) were measured at 1 kHz and up to 2500 kV/cm, before and after irradiation exposure. Five to ten electrodes on each sample were specifically tested to reduce effects of local sample variability. One sample from each set labeled "control" stayed at Georgia Tech to account for effects of aging. Six samples from each set were sent to the US Naval Research Laboratory (NRL) for gamma radiation exposure. The samples were exposed to a ^{60}Co source at doses ranging from 0.1 to 5 Mrad(Si) at a dose rate of ~400 rad(Si)/s. A second control sample, labeled 0 Mrad(Si), for each set was also sent to NRL but not exposed to gamma radiation to monitor additional factors related to transportation of the samples (e.g. storage temperatures, additional radiation exposure via air transportation). Overall the before and after irradiation characterization was performed in a two weeks period.

7.4 Results and Discussion

In their pristine state (before cycling), the PEALD samples exhibit ferroelectric behavior without any evidence of strong pinning (Figure 7-1). Conversely, the THALD samples show strongly pinned ferroelectric or anti-ferroelectric-like behavior, as evidenced by pinched P-E hysteresis loops. In Hur *et al.*, consistently with the observations above, the XRD analysis revealed that the crystal structure of the PEALD films was closer to the o-phase, while that of the THALD films was closer to the t-phase (Figure 7-2).[120] Nonetheless, both sets of films required additional electrical cycling to wake-up the samples to a stable ferroelectric state (i.e. invariable with further electric-cycling).

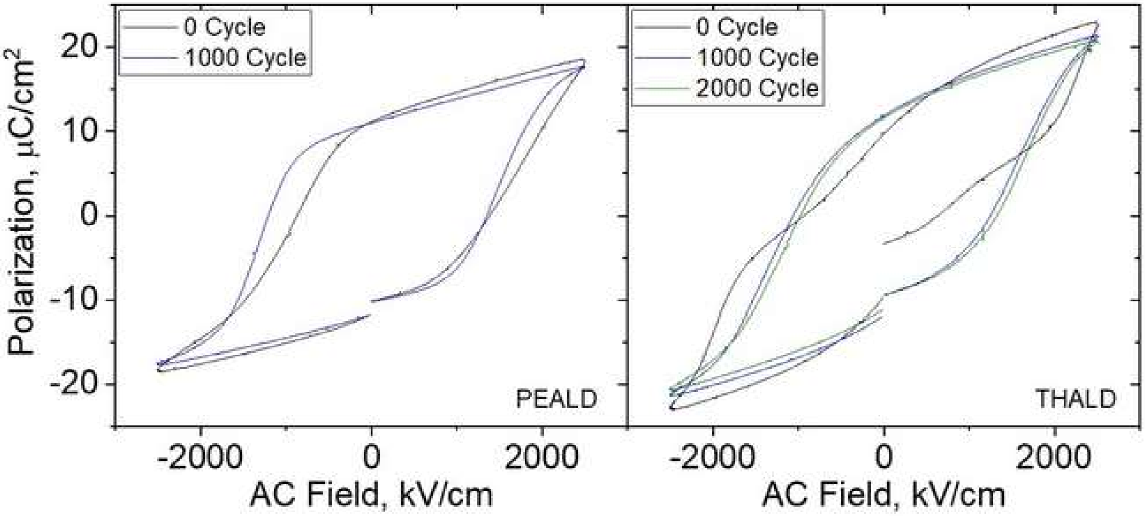

Figure 7-1 Representative polarization loops for pristine and cycled states of PEALD (left) and THALD (right) HZO thin films.

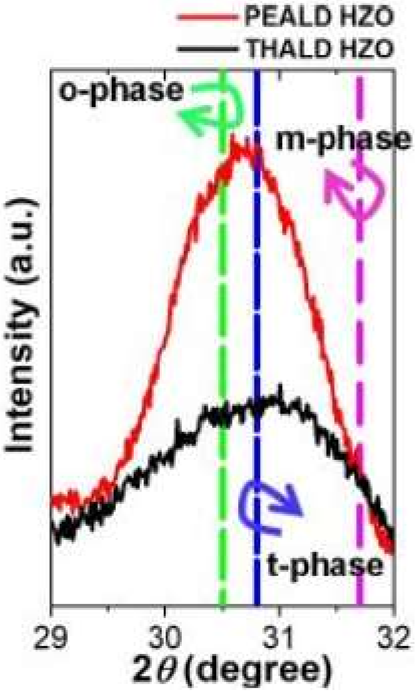

Figure 7-2 XRD of PEALD and THALD HZO thin films.[120]

Slight variations in the response were observed across the wafers (Figure 7-3), with remanent polarization, P_{rem}, varying between 10 μC/cm^2 and 13 μC/cm^2 in PEALD and THALD samples. These variations may be due to a number of factors, including the uniformity of the sample thickness across the wafer, the precision in the fabrication of the electrodes, or possible differences in defect distribution across the wafer, and should be taken into consideration with respect to the trends found in this study. For reference, PZT thin films of ~500 nm thickness have remanent polarization (P_{rem}) values of around 15 μC/cm^2. [49] Both the PEALD and THALD exhibit comparable P_{rem} (10.5 μC/cm^2 ± 0.7

μC/cm^2 and 11.4 μC/cm^2 ± 0.5 μC/cm^2, respectively) to PZT thin films at a fraction of the thickness.

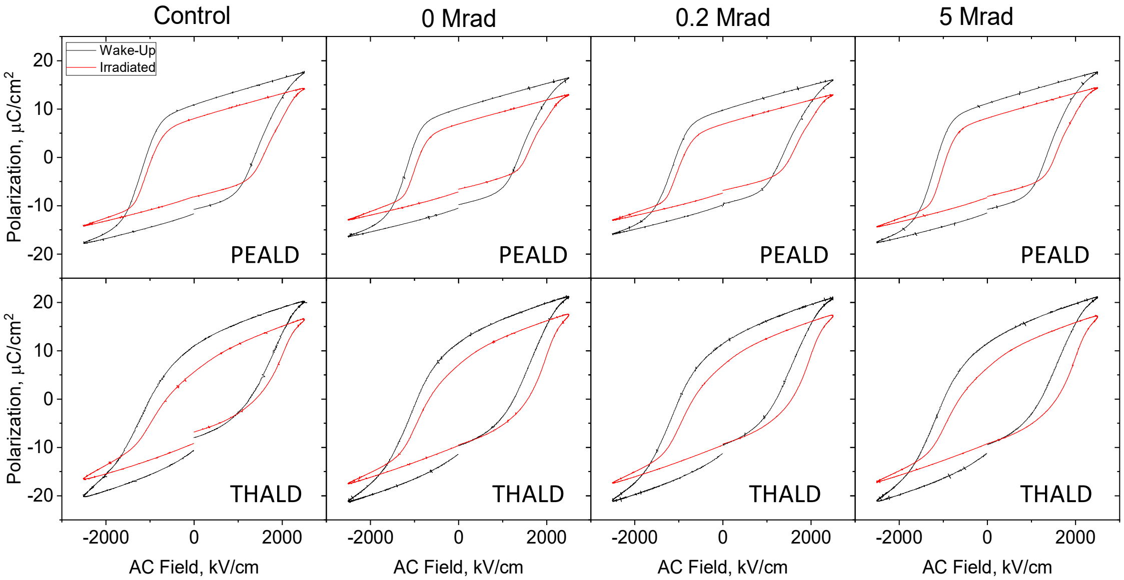

Figure 7-3 Representative polarization loops before and after irradiation for select PEALD (top) and THALD (bottom) HZO thin films. From left to right are the control, 0 Mrad(Si), 0.2 Mrad(Si), and 5 Mrad(Si).

After irradiation, significant degradation in polarization response was found in all samples, including the control and 0 Mrad(Si) samples. Such changes indicate that the films are highly susceptible to aging effects, even after only two weeks. Comparing the P-E loops of control and pristine samples (Figure 7-1 and Figure 7-3) significant degradation is observed in both the PEALD and THALD processed samples. The large change in saturated and remanent polarization values after the irradiation experiments as compared to the pristine and cycled films indicates the samples are not simply reverting back to the pristine state.

Figure 7-4 shows the degradation trends for various characteristic parameters extracted from the P-E curves. In the PEALD samples, the saturation polarization (P_{sat}) was reduced by between ~27% and ~30% for all of the doses studied. However, it also degraded by ~25% and ~30% for the control and 0 Mrad(Si) samples, respectively. This similarity in changes between aged, control and irradiated samples indicates that the degradation due to irradiation is much smaller in comparison to the degradation due to aging. Overall, similar trends were observed for many other parameters descriptive of the polarization hysteresis loops in PEALD samples: the control sample showed the least amount of variation with respect to the measured properties after wake-up, including positive and negative remanent polarization ($P_{rem,+}$ and $P_{rem,-}$), positive and negative coercive fields ($E_{C,+}$ and $E_{C,-}$), and overall area under the curve (A). All other samples, including the control (non-irradiated sample) showed higher changes with respect to their post wake-up state. However, no substantial differences were observed in any of the above characteristic parameters as a function of radiation dose. It is also noticeable that there is slightly less degradation in the irradiated PEALD samples compared to the 0 Mrad(Si).

In comparison, the THALD samples display a wider range of variability with respect to the PEALD samples. P_{sat} values degraded by ~33% and ~25% for the control and 0 Mrad(Si) samples, respectively, while the changes in the TID studies ranged within

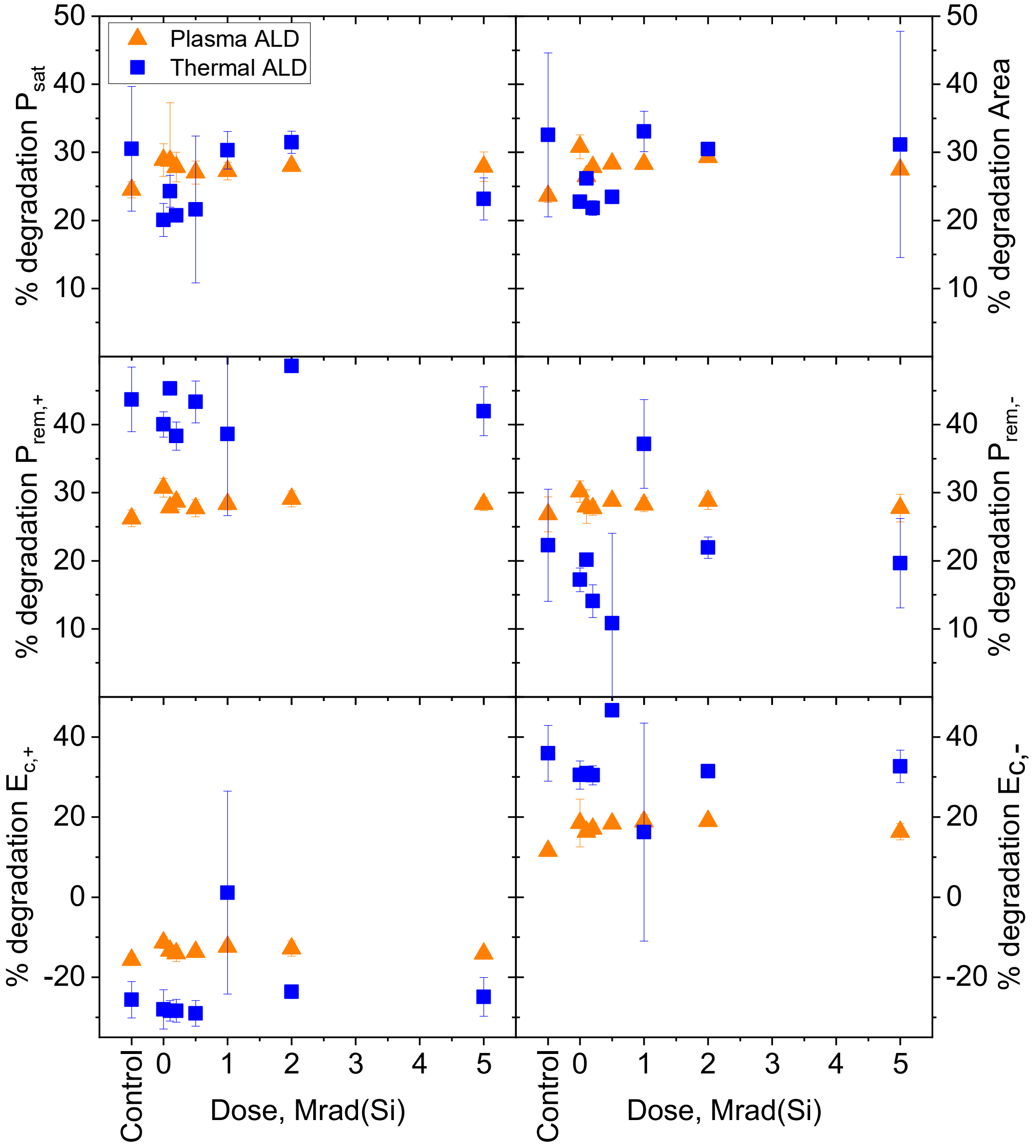

Figure 7-4 Degradation trends in polarization response in PEALD (orange) and THALD (blue) samples. Parameters shown include saturated polarization (P_{sat}, top left), overall area under curve (A, top right), positive remanent polarization ($P_{rem,+}$, middle left), negative remanent polarization ($P_{rem,-}$, middle right), positive coercive field ($E_{C,+}$, bottom left) and negative coercive field ($E_{C,-}$, bottom right).

the same values. Compared to the 0 Mrad(Si) sample, the degradation was similar at the lower doses (0.1 to 0.5 Mrad), and greater at higher doses (1 to 5 Mrad), seemingly indicating an accumulation of radiation-induced defects which lead to degraded response.

In perovskite ferroelectric materials such as PZT, radiation-induced free electrons can be trapped in oxygen vacancies and result in singly charged, more mobile defects. Under applied electric field, such singly charged oxygen vacancies can accumulate at the ferroelectric-electrode interfaces, reduce ferroelectricity and ultimately degrade the material's response.[49] However, PZT thin films studied over a similar period of time do not show significant signs of aging in P_{sat}, with degradation of <1% in the 0 Mrad(Si) samples.[49] The degradation due to irradiation in those films also maintained below 2% for TID studies up to 5 Mrad(Si). Hence, the effects of aging on the saturation polarization in HZO films are of more significant concern than the degradation due to radiation in both sets of HZO thin films.

Intriguingly, while the PEALD samples show a consistent change (~27% decrease) in the positive and negative P_{rem}, the THALD samples show a much larger degradation in all samples for the positive remanent polarization, $P_{rem,+}$, and non-monotonic changes between 10 and 37% degradation in the negative, $P_{rem,-}$. The degradation in $P_{rem,+}$ and $P_{rem,-}$ for irradiated samples with respect to the 0 Mrad(Si) sample ranged from -2 to +10%, and from -6 to +15%, respectively. The results are consistent with observations with respect to the saturation polarization, in that aging is the major contributor to the observed changes in the samples for HZO films regardless of the processing approach. However, while in the PEALD samples the changes in saturation and remanent polarization are of similar values (regardless of dose or parameter), the changes in the THALD samples are clearly polarity dependent, with larger degradation in the positive rather than negative remanent polarization. This observation is consistent with the P-E curves in Figure 7-3, where the negative remanent polarization seems to be in large part unaffected by radiation exposure. However, both the coercive fields and the area under the curve also substantially change after radiation exposure, possibly compounding effective degradation in the ferroelectric content within the films.

Both sets of films had a similar level of internal bias after wake-up (Figure 7-5). Internal bias was calculated as $E_{internal} = (E_{C,+} + E_{C,-})/2$. After irradiation, $E_{internal}$ increased in both set of films, however, the change towards positive fields was substantially higher in the THALD samples. Internal bias in perovskite ferroelectric is often associated with an asymmetric distribution of defects within the material, such as the collection of oxygen vacancies towards one of the ferroelectric-electrode interfaces.[121] Such behavior has also been observed in fluorite ferroelectrics, where post-annealing under different gases lead to changes in the internal bias due to differences in oxygen vacancy concentrations at the top and bottom electrodes.[75] Other studies have also suggested that internal bias in hafnia-based films may be caused by trapping of electrons in deep states of oxygen vacancies, which then pin domains in particular orientations through cycling.[73] Both of these effects can lead to the asymmetric nature in the degradation of the remanent polarization for the irradiated samples reported here.

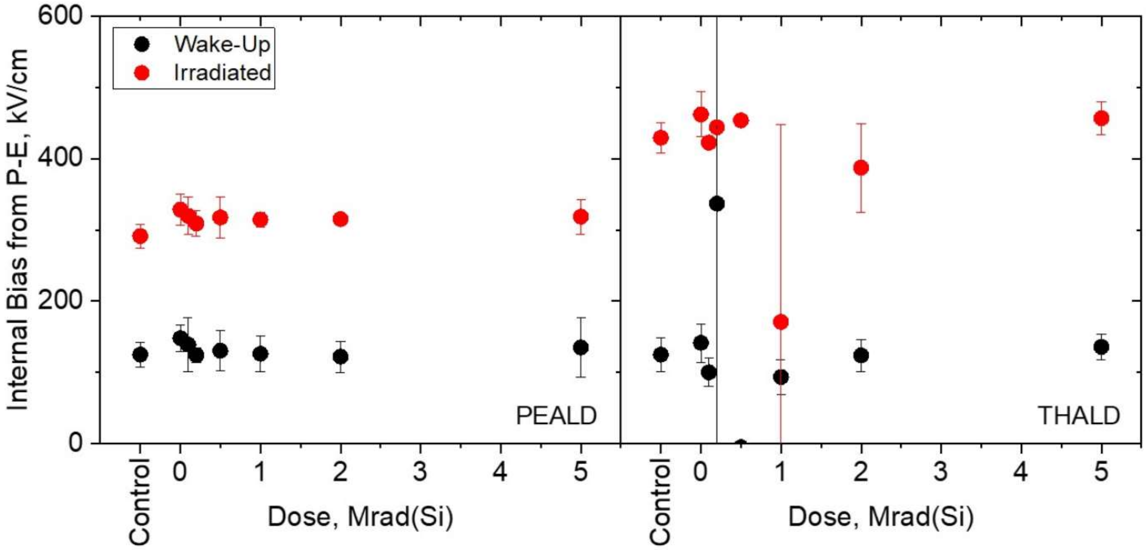

Figure 7-5 Internal bias of PEALD (left) and THALD (right) films before and after irradiation, calculated from coercive fields of *P-E* loops.

Further examination of the paraelectric contribution of the dielectric response ($\varepsilon_{paraelectric}$) calculated from the slope of the linear portion of the P-E curve from 2500 kV/cm to 2000 kV/cm, reveals larger changes in the THALD samples than the PEALD samples (Figure 7-6).[122–125] Although the standard deviations make it difficult to draw concrete trends, it is shown that at low doses $\varepsilon_{paraelectric}$ decreases, and at higher doses increases for the THALD samples. The trend noticeably follows that found in P_{sat} and A, pointing towards an accumulation of radiation-induced defects which degrade the ferroelectricity to a greater extent in the THALD films than in the PEALD films. Additionally, from Figure 7-3 it is seen that the nucleation of opposite domains after positive saturation occurs more rapidly than after negative saturation for both of the THALD and PEALD samples. It is unclear why nucleation of opposite domains is more difficult after saturation at negative fields, however the defects responsible for this also contribute to the positive shift in $E_{internal}$.

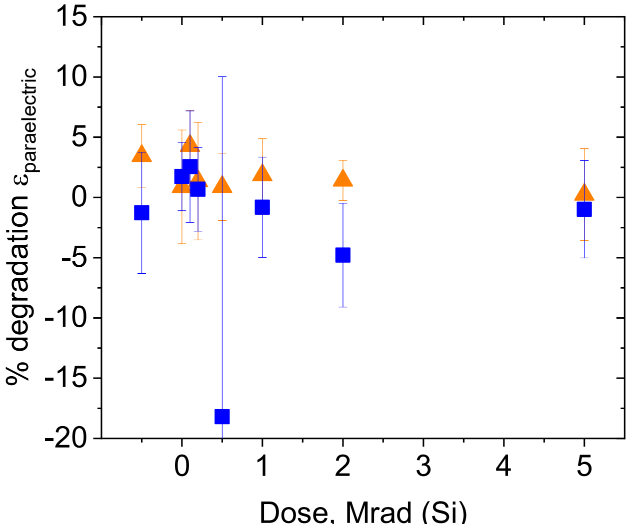

Figure 7-6 Degradation trends in the paraelectric contribution to the dielectric response for PEALD (orange) and THALD (blue) HZO thin films.

Asymmetric changes are also found in the switching fields for THALD, obtained from the electric fields of where the maximum and minimum current occurs ($E_{switch,+}$ and $E_{switch,-}$). (Figure 7-7). The PEALD samples show relatively equal shifts in $E_{switch,+}$ and $E_{switch,-}$ of approximately 10% towards positive fields. The THALD samples show a larger shift in $E_{switch,+}$ of about 20%, and a smaller shift in $E_{switch,-}$,along with more sporadic changes across the doses studied. In typical perovskite ferroelectrics, the positive and negative switching fields found in the I-E measurement coincide with the positive and negative coercive fields found in the P-E measurement. Thus, one would expect the degradation seen in E_{switch} to match with the degradation in E_C. However, the degradation trends of these parameters do not match for either films. A closer inspection of E_C and E_{switch} reveals a large discrepancy between the values, especially for the THALD samples

(Figure 7-8 and Figure 7-9). This indicates that there is a substantial amount of current that is not associated with the ferroelectricity in the films, and may possibly be associated with the semiconductor nature of the films. In both cases, E_{switch} shifts to a lesser degree after irradiation than E_C, further suggesting that defects introduced affect the ferroelectric and semiconductor properties differently.

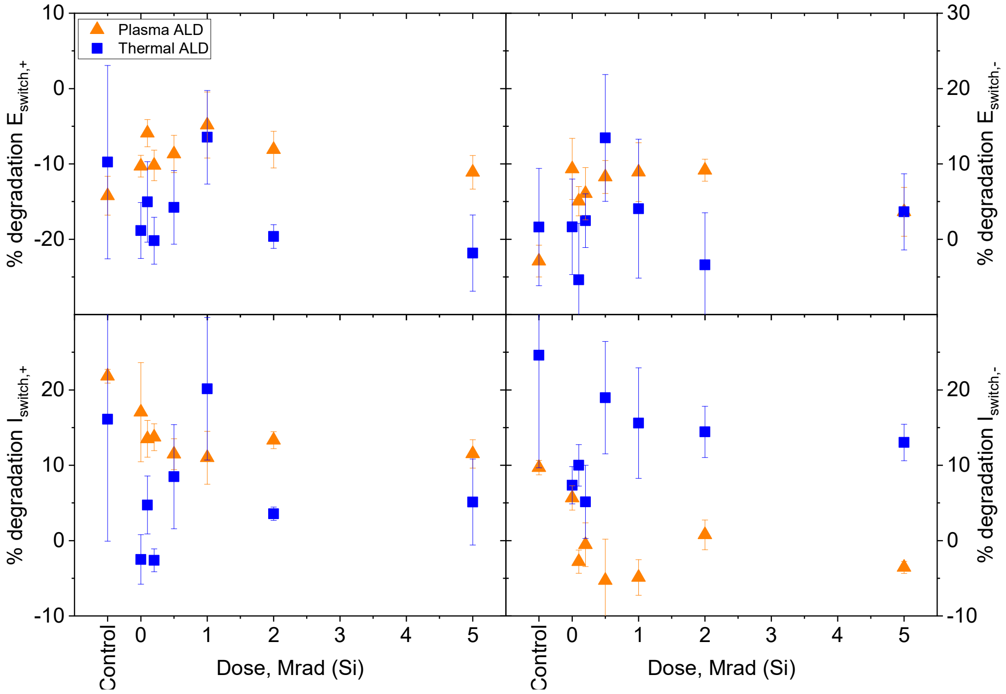

Figure 7-7 Degradation trends for switching current response in PEALD (orange) and THALD (blue) samples.

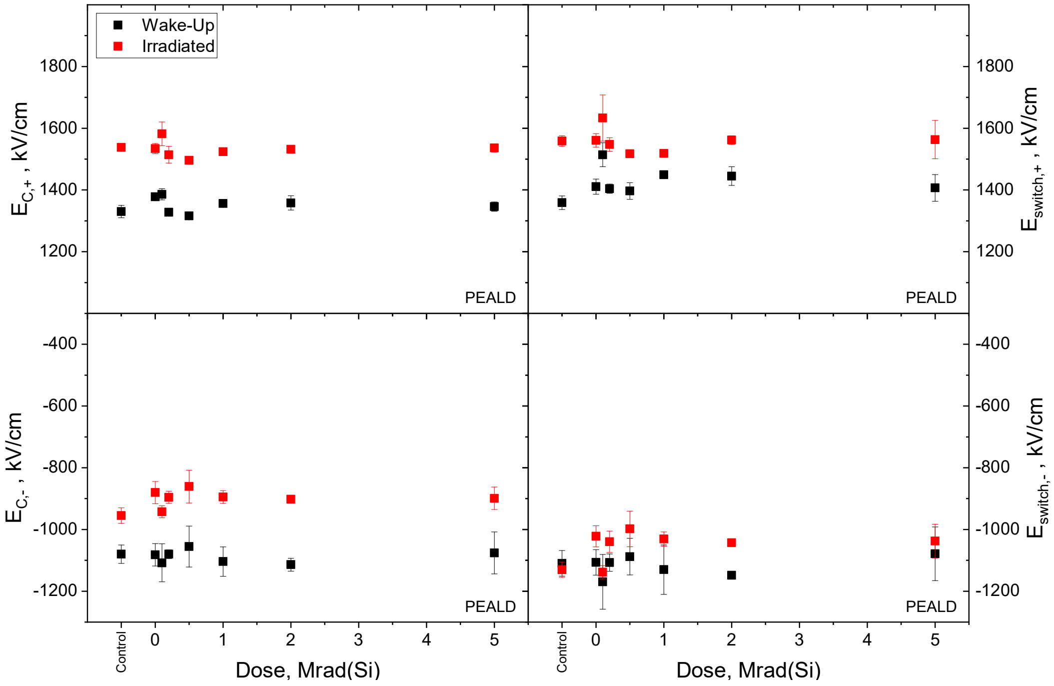

Figure 7-9 Comparison of Ec and Eswitch for PEALD HZO thin films.

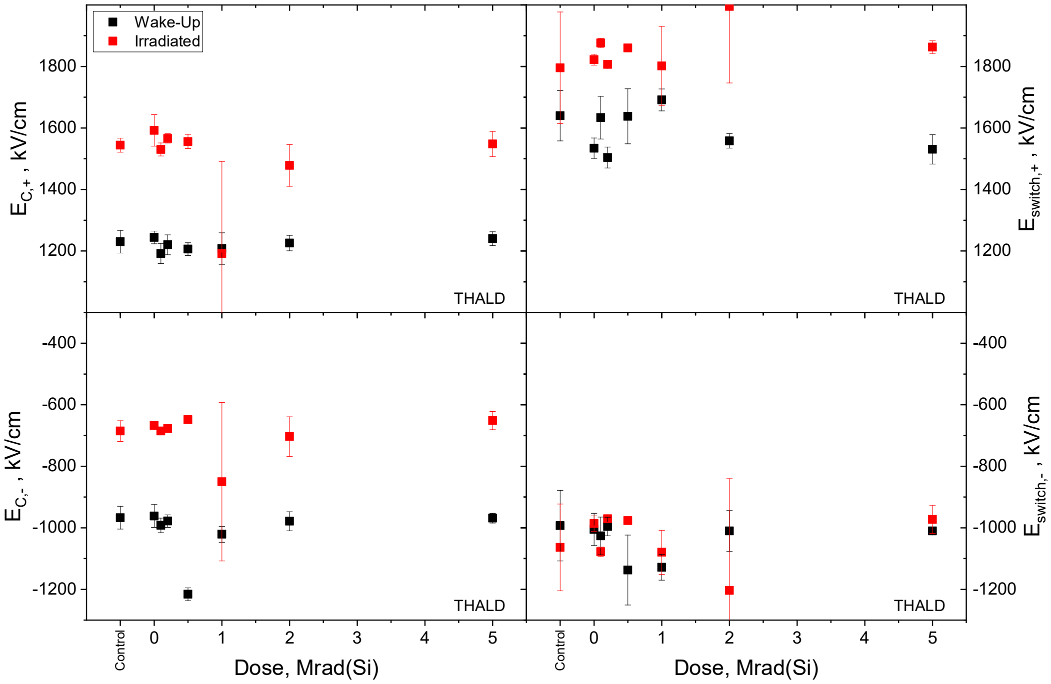

Figure 7-8 Comparison of Ec and Eswitch for THALD HZO thin films.

Further asymmetry relating to both samples are observed in the switching current curves (Figure 7-7). The currents at the switching fields ($I_{switch,+}$ and $I_{switch,-}$) are also particularly asymmetric for the PEALD processed samples, with substantially larger $I_{switch,+}$ than $I_{switch,-}$, and reduced asymmetry at positive than negative voltages. In these samples, the positive switching current degrades at irradiation significantly more than the negative switching current.

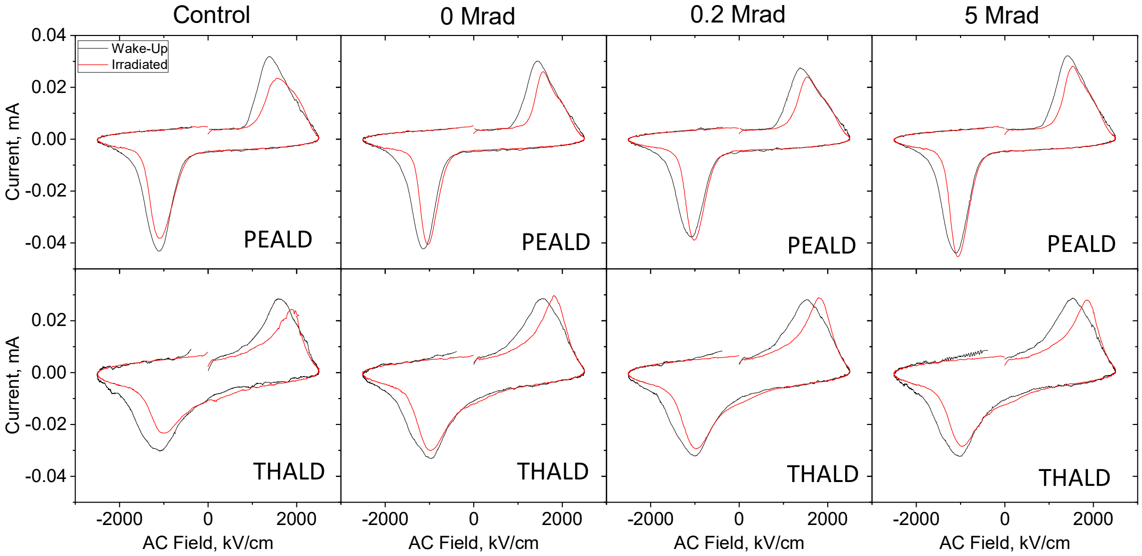

Figure 7-10 Representative switching current loops before and after irradiation for select PEALD (top) and THALD (bottom) HZO thin films. From left to right are the control, 0 Mrad(Si), 0.2 Mrad(Si), and 5Mrad(Si).

Looking more closely at the switching current loops (Figure 7-10) of the PEALD samples, secondary switching current peaks appear to the right of the previous switching peaks. Specifically, the secondary peaks appear in the control samples and irradiated loops to the right of the prominent in PEALD samples as shoulders of the positive switching current, and as new peaks close to 0 kV/cm (at reversing of the field) for the THALD samples. The difference in the location of such secondary peaks suggests different mechanisms in which the ionization radiation interacts with the PEALD and THALD samples. Specifically, secondary peaks at higher fields can be due to either presence of defects that strongly pin ferroelectric domains at switching (under positive applied electric fields), or weakening of preexisting pinning sites through ionizing radiation. However, in the latter case, it is expected that the overall area under the switching curve be increased at "activation" of new domains under appropriately high applied electric fields, while in the former case, the overall area under the curve is expected to decrease. Indeed, the overall area under the curve at switching is reduced in all samples (consistently with the *P-E* curves). Hence, the new peaks are more consistent with newly created, or more strongly pinned domains. We note that the stronger pinning of preexisting domains is also consistent with the overall reduction of the ferroelectric character (i.e. reduction of P_{sat} and P_{rem}) in the samples.

In the THALD samples, $I_{switch,-}$ generally showed more degradation than $I_{switch,+}$, in addition to the appearance of the new secondary (negative current) peak is found near zero field. Comparing this with the pristine loops in Figure 7-11, it appears that the two peaks exist in the pristine state before the wake-up cycling. However, after wake-up the two peaks mostly "morph" into a single wider peak at intermediate fields. After irradiation or aging, the peaks separate and shift by different amounts to lower (absolute) fields. While the origin of this peak is still unknown, it may be another indication of a change in the semiconductor properties of the material, where the defects introduced are creating new conduction paths in the films, such as introduction of an intermediate band in which electrons can move into at lower fields.

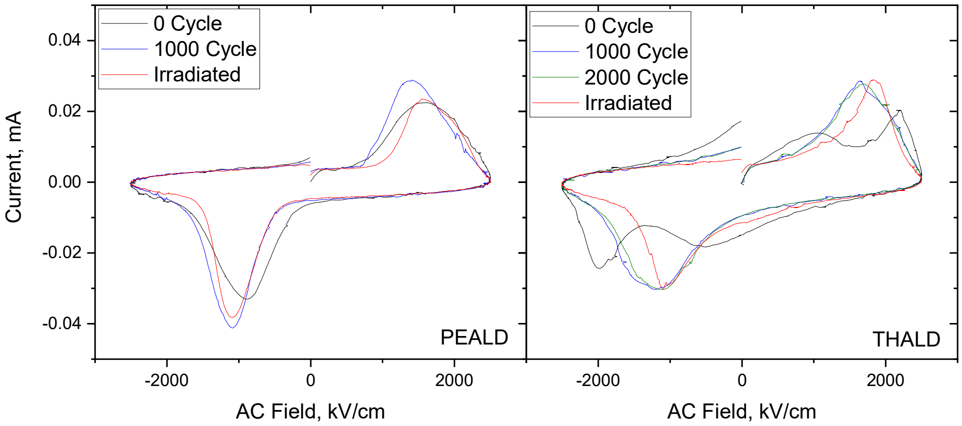

Figure 7-11 Evolution of switching current loops from pristine (0 cycle) to cycled and finally ”irradiated”. Samples shown are the controls, so the irradiated curve shows only effects of aging.

In comparison the PZT films, the HZO films show markedly different characteristics in both cycling and aging. It is clear that with even less than 1000 cycles, the ferroelectricity is very strongly influenced in HZO films than compared with PZT films, where much higher cycling is required to influence the polarization response.[25] This indicates that the defects responsible for the ferroelectricity in HZO thin films may require less energy to move than in PZT thin films. Previous studies on HfO_2 have suggested that in fluorite-structured ferroelectrics, accumulation of oxygen vacancies at the dielectric-electrode interface during processing can stabilize the tetragonal phase in these regions, limiting the initial ferroelectric response in these films. A redistribution of the oxygen vacancies through electrical cycling can lead to the ferroelectric wake-up through the reduction of the stabilizing effect on the tetragonal phase.[72,126] Additionally, significant aging occurred in the samples after only two weeks, which is not observed in ferroelectric perovskite films over the same period of time in similar TID studies.[49,91] This further suggests the activation energy for defects to realign into more energetically favorable positions is much lower in the HZO films than in PZT, leading to suppression of ferroelectricity in a shorter amount of time.

With a direct comparison between the *P-E* and *I-E* loops, it becomes clear that additional changes occur affecting the conduction than expected from simple polarization switching, as observed in many perovskite ferroelectrics. Previous studies on HfO_2 films have shown that gamma radiation can induce crystallographic changes in these materials, where broadening of XRD peaks with increasing radiation dose suggested significant changes in crystallite size and strain. Shifts were observed in the flat band and mid-gap voltages, in turn affecting the conductivity of the films, attributed to trapped charges in oxygen vacancies.[127] Other studies have suggested changes in oxidation states of Hf and O with differing gamma radiation dose.[128] Although in the present report the composition is different compared to the prior reports, similar changes in the material's band gap would be possible and indeed would be consistent with our observations. It is reasonable to assume that the stability of the unit cell in the as-deposited samples, and after the eventual wake-up, could affect the extent of the ionization radiation disruption to the preexisting structure and conductivity, and should be further explored.

Overall, the PEALD samples studied here showed more stable P_{rem} after irradiation up to 5 Mrad(Si) compared to the THALD samples, with the latter showing degradation ranging from 11 to 50%. However, previous studies on for THALD HZO thin films have reported <5% degradation in polarization response after 10 Mrad(Si) irradiation. The apparent discrepancy might be due to the crystallization temperature used for the two sets of films. The films used in the prior report were post annealed at 550 °C, compared to the 400 °C used for the THALD HZO thin films in the current study.[81] The differing results suggest that the defect landscape responsible for radiation tolerance of the films is extremely process-dependent, and that the lower post-annealing temperatures for THALD HZO thin films may have led to an overall lower "quality" of the crystallized ferroelectric material. Thus, PEALD is overall an advantageous approach over THALD in providing greater radiation tolerance in ferroelectric HZO thin films at a lower post-annealing temperatures.

7.5 Conclusions

In summary, PEALD and THALD ferroelectric HZO thin films were investigated to compare the effect of processing approach on the radiation tolerance of the fluorite ferroelectric films. While both films suffered from aging-related degradation, the PEALD films showed more stable polarization response across doses up to 5 Mrad(Si), compared to THALD samples. Strong internal biases were found in both set of films after both aging and irradiation. Secondary peaks in the switching current loops, and their relative changes at different TID, further confirm differences in the defects preexisting and induced post aging and/or irradiation in the two sets of HZO films. While the PEALD films exhibit slightly lower saturated and remanent polarization than THALD films, the greater stability after irradiation makes them more attractive for applications with high radiation exposure. In comparison to PZT thin films, the PEALD films showed greater radiation tolerance in remanent polarization, making them good candidates for radiation-tolerant ferroelectric memory devices, although additional challenges will need to be addressed based on the additional complexity of the changes induced in the switching current.

7.6 Acknowledgements

This work was supported by the Defense Threat Reduction Agency, Basic Research Award No. HDTRA 1-15-1-0035 to Georgia Institute of Technology. The contents do not necessarily reflect the position or the policy of the federal government, and no official endorsement should be inferred.

CHAPTER 8. SUMMARY AND FUTURE WORK

8.1 Summary and Conclusions

Ferroelectric oxide materials exhibit large dielectric, piezoelectric, pyroelectric, and polarization response, making them extremely attractive for the miniaturization of numerous microelectronic devices, from random access memory, to MEMS sensors and actuators, and even energy harvesting units. In addition, an increasing interest in utilizing these devices in radiation-hostile environments, including in aerospace for satellites and airplanes, for medical physics tools, and for monitoring on nuclear systems, breeds another requirement of radiation-tolerant materials. While research on optimization of current material systems has shown improvements in size, efficiency, and radiation-tolerance, efforts are beginning to stall as physical limitations are reached. The work in this thesis explores new material systems which have strong potential as alternative materials to the current standards (e.g. PZT) which have both strong functional response and strong radiation-tolerance. Through this work, a better fundamental understanding of material properties responsible for the high functional response and radiation tolerance is achieved, enabling the design of even better material systems for these applications. This is accomplished by probing the defects and defect-defect interactions which influence both functional response and radiation tolerance, including domain walls, grain boundaries, porosity, crystal structure, radiation-induced free electrons, and mobile oxygen vacancies.

8.1.1 Microstructure Engineering PMN-PT Thin Films

Optimization of chemical solution deposition processing parameters to defect-engineer PMN-PT thin films allowed for partial control of grain structure and porosity. The addition of excess Pb with respect to the stoichiometry in the precursor solution of the seed layer, PTO, allowed for more consistent 001-orientation in the PMN-PT films, ensuring maximum functional response in the films studied. The addition of excess Pb in precursor solution also allowed for minimization of intragranular porosity of the PMN-PT thin films: the films exhibited monotonically increasing dielectric permittivity, remanent polarization, and effective piezoelectric response with increasing excess Pb content. Tests on processing recipes used in previous studies, as well as modified literature recipes, revealed the importance of utilizing high crystallization temperatures (~ 800 °C) to ensure large, columnar grain structure. And while higher drying and pyrolysis temperatures combined with lower crystallization temperatures greatly reduced porosity, the dielectric, polarization, and piezoelectric responses were compromised due to the increased concentration of grain boundaries present in a film of small, stacked grains.

8.1.2 Radiation Tolerance of PMN-PT Thin Films

An initial study exposing PMN-PT thin films to gamma-radiation doses up to 10 Mrad(Si) revealed that radiation tolerance of PMN-PT thin films were equivalent or superior to PZT thin films, while maintaining higher functional response than the PZT thin films. The dielectric and polarization response changed <5% and the effective piezoelectric response changed <10% for the PMN-PT thin films across all doses studied. The multi-valence B-site cations present in PMN-PT may have acted as trapping sites for radiation-induced electrons, preventing further accumulation of mobile oxygen vacancies known to cause deleterious effects similar to fatigue. It was observed that at low doses < 0.5 Mrad(Si), the dielectric and piezoelectric responses showed evidence of enhancement. While these enhancements were minimal and within the experimental errors, enhanced response after low radiation exposure has been previously observed in other functional materials, and could be another method of defect-engineering materials with greater functional response.

Although the previous study showed greater radiation tolerance in PMN-PT compared to PZT films, the PMN-PT thin films contained a greater concentration of porosity and grain boundaries. Such interfacial regions might act as defect sinks and increase the films' radiation tolerance. Additional TID studies were then conducted on films engineered with various microstructures, including varying levels of porosity and grain boundaries, as well as differing grain structures. All films showed <5% degradation in dielectric and polarization response, and <15% degradation in piezoelectric response. The microstructure of the films had strong effects on the overall functional response but showed little to no influence on the radiation tolerance, confirming that PMN-PT films are inherently more radiation-tolerant than PZT films. An interesting observation in the experiments is the much lower extrinsic contributions present in all PMN-PT films compared with the previously studied PZT films, contradicting the previous hypothesis that increased domain wall motion leads to higher functional response and radiation tolerance. It is assumed, then, that other inherent properties hold greater influence on the radiation tolerance, such as the presence of chemical and polar nanoregions.

8.1.3 Radiation and aging effects on ferroelectric HZO thin films

TID studies were conducted on ferroelectric HZO thin films exposed to gamma-radiation up to 5 Mrad(Si). The films were processed either via plasma-enhanced atomic layer deposition (PEALD) or via thermal atomic layer (THALD) deposition. Films processed with both techniques showed much stronger degradation due to aging than to irradiation. The polarization response showed degradation of up to 25% and 30% due to aging in the PEALD and THALD films, respectively. Outside of the effects of aging, the PEALD films showed substantially more stable polarization response across the doses studied, with variations of <5%, while the THALD films showed up to 10% degradation. We posit that the higher stability of the ferroelectric phase in the pristine PEALD films contributes to its stability against radiation tolerance. The redistribution of oxygen vacancies may prevent the formation of the defect-rich tetragonal phase and instead promote the formation of the orthorhombic phase responsible for the ferroelectricity in HZO thin films. Discrepancies between coercive fields of the P-E loops and switching fields of the I-E loops suggest that the defects present influence the semiconductivity of the materials differently than the ferroelectricity. Unusual additional peaks were found in both PEALD and THALD films, possibly due to the introduction of defects which change the semiconductor properties of the films.

8.2 Future work

This section details potential areas for future work to advance engineering methods for and scientific understanding of radiation tolerance in ferroelectric materials for microelectronic device applications. Future studies include the use of spatial chemical characterization techniques to understand the influence of processing techniques on Pb migration; improved processing approaches in order to more consistently control the microstructure of the films and ultimately separate (and possibly quantify) the impact of each parameter (grain density, orientation, porosity, etc.) on radiation tolerance of the films; the use of structural characterization techniques to further understand processing effects on material properties; post-irradiation healing methods that would enable a longer lifetime for the devices or alternatively self-healing after radiation exposure; and additional ionic and electronic characterization to further understanding of the impact of radiation exposure on the defect landscape of ferroelectric materials.

8.2.1 Spatial distribution of chemical elements in PMN-PT

Furthering our understanding of the Pb distribution (or segregation) on the surface and within the film stack may inform additional processing techniques useful to maintain Pb stoichiometry within the film without compromising the microstructure. SEM and AFM imaging often reveal surface particles of unknown compositions, largely undetectable by XRD analysis. These particles, if not the same composition as the ferroelectric layers, can degrade the functional response of the films, and potentially negatively affect the microstructure of the layers deposited on top. Angle resolved X-ray photoelectron spectroscopy (XPS) involves varying the take-off angle to increase the measurement's surface sensitivity. This increased surface sensitivity can lead to identification of secondary phases on the surface of the material such as pyrochloric phases or simple oxide phases. Secondary phases previously unknown on the surface of CSD processed PZT thin films have recently been identified as nanocrystalline ZrO_2 using this technique.[129,130] This technique could be used to more accurately identify the surface chemistry of PMN-PT films, and subsequently inform how different processing parameters will influence the formation of secondary phases.

Energy-dispersive x-ray spectroscopy (EDX) or time-of-flight secondary ion mass spectrometry (ToF-SIMS) can be used to monitor the distribution of Pb and other elements in the ferroelectric stack. TEM can provide images with atomic resolution, and in conjuction with EDX can better identify specific areas of Pb deficiency, such as comparing the Pb content of the top layer to the bulk of the thin film. This technique could also be leveraged to understand the extent of Pb diffusion into the bottom electrode stack, and how different techniques to control Pb content can affect such diffusion. Large Pb diffusion into and under the bottom electrode stack mechanically weaken the adhesion to the substrate and can ultimately result into film delamination (with increasing deposited film thickness or during use). ToF-SIMS performed on cross-sections of the film can also provide additional information on the Pb distribution throughout. Information with respect to chemical heterogeneities in the film and correlation with different processing techniques will help inform the links between processing-structure-properties of these films.

8.2.2 Improved Reliability in PMN-PT Thin Film Processing

As presented in this work, PMN-PT thin films show promising functional response and radiation tolerance for use in next generation multi-functional devices. However, there are still challenges to reliably fabricating pore-free and crack-free films. While some parameters have been shown to increase the density and improve the grain structure of PMN-PT thin films, the continued presence of porosity and potential cracking in the films have to be fully addressed. As discussed in Chapter 4, the control of Pb content is crucial to fabrication of high density, oriented PMN-PT films, as insufficient Pb results in domed grain formation (resulting in lower electric breakdown), and excessive PbO can create PbO pockets that volatilize at crystallization temperature, leaving behind pores. In materials such as La-doped PZT (PLZT), the utilization of PbO covercoat has been reported to increase the ferroelectric phase of the material, and eliminate nanocrystalline formation on the top surface.[131] The use of the covercoat could provide additional benefits to PMN-PT by not only alleviating secondary phase formation, but also preventing the formation of domed grains. This technique was briefly explored in Bastani et al, showing promising results for PMN-PT thicker than 600 nm.[56] However the trapping of PbO pockets created additional leakage issues in the thin films. The concentration of the PbO covercoat to prevent PbO pockets as well as its necessity over each annealed layer should be further explored to improve PMN-PT thin film quality. The use of acetic acid wash subsequent to each crystallization can remove eventual remaining PbO nanocrystals, and hence possibly decrease the presence of PbO pockets trapped between layers. Challenges with such an approach may include the additional processing times necessary to add and pyrolyze covercoats, as well as additional acetic acid washes in between to mitigate trapping of PbO particles between layers.

A challenge repeatedly encountered in this work was a lack of consistent processing parameters in literature. A contributor to such persisting differences, even within the same research groups, is the partial pressure of PbO present in the rapid thermal annealing tool during crystallization. Volatilization of PbO from precursor solution, can result into coatings on the surface of the annealing chamber, ultimately affecting PbO partial pressure during subsequent runs. Similarly contributing to the variable atmosphere is eventual gas flows that in some tools are mandatory for cooling of the quartz chamber. The addition of PbO directly into the annealing chamber to create a PbO overpressure may alleviate the issues discussed above. This method was shown to improve density in sintering of PLZT films as it prevented excess volatilization of PbO from the films.[132] A similar method can be applied during crystallization of PMN-PT thin films, possibly reducing or even eliminating the need for balancing of PbO in other processing steps.

8.2.3 Post-Irradiation Healing

The work in this thesis suggests the viability of PMN-PT and HZO thin films for next-generation radiation-tolerant multi-functional devices. However, there is still little understanding of how these materials will operate under varying conditions, such as through aging, continuous cycling (fatigue), and possible fluctuations in temperature. Previous studies have suggested that electrical cycling at low fields or thermal treatment at above the Curie temperature can lead to recovery of radiation-induced degradation of ferroelectric and piezoelectric response.[41,50] This effect is attributed to redistribution of defects within the material through the methods above. Further studies should also be conducted to determine if some of the radiation-induced defects are reversible over time (self-healing), or if the samples will degrade further with aging (compound effects). Previous study on PZT thin films showed some amount of recovery in the C-V response after the samples were left un-probed for an additional period of time (few days) post-irradiation.[133] Studies on aging, thermal loading, and electrical cycling post-irradiation can provide additional information on the operation of these materials under the varying conditions, as well as provide strategies to heal devices exposed to radiation. The extent to which the functional response is recoverable can inform whether the defects introduced are reversible, giving additional information on the types of defects formed by radiation exposure.

8.2.4 Structural characterization of HZO thin films

While PEALD HZO films showed superior response to THALD films in this study, detailed studies of differences in defect distribution resulting from the two processing approaches and hence possible effects of aging are needed. As was shown in this thesis, the PEALD thin films appeared to show significantly more stable ferroelectricity than the THALD thin films, but both suffered significantly from aging affects. Investigations on the crystal structure of the HZO films may reveal the distribution of oxygen vacancies within the HZO thin films and subsequently the effect on its ferroelectricity. Scanning transmission electron microscopy (STEM) has been used to study the changes in the crystal structure of HfO_2-based thin films at different stages of electrical cycling (e.g. pristine, woken-up, fatigued). Tetragonal, monoclinic, and orthorhombic phases were correlated with differences in oxygen vacancy accumulation throughout the films.[72] An increase in orthorhombic phase (and thus decrease in tetragonal and monoclinic phases) after cycling was attributed to a redistribution of oxygen vacancies.[73] STEM imaging can be used to observe the changes of the crystal structure of the PEALD and THALD thin films in various stages (pristine, woken-up, fatigued, aged, and irradiated), allowing for a better understanding of oxygen vacancy migration under different conditions and its effect on the ferroelectricity.

8.2.5 Ionic and Electronic Conductivity Measurements

Further investigation should be conducted to understand how defects change or move in the HZO films might affect its ferroelectricity. Similarly, investigations are needed on how the semiconductor nature of the material may influence its functional properties. Specifically, ionic and electronic conductivity measurements can provide insight into the changes in the defect landscape, and elucidate the origins of the additional peaks found in the aged and irradiated HZO samples. Changes in the electronic conductivity of the samples can be investigated using current density-voltage (I-V) measurements.[134] Thermally stimulated depolarization measurements (TSDM) have previously been used to observe the concentrations and movements of singly-charged and doubly-charged oxygen vacancies within HfO_2 thin films.[73,135] Impedance spectroscopy can also be utilized to measure changes to the defect concentrations and mobility in these films. These methods will provide valuable information on the changes in the defect landscape which affect the films' ferroelectricity after aging or radiation exposure that can be used to further engineer material systems to be susceptible to the deleterious effects of radiation-induced defects.

REFERENCES

1. Trolier-Mckinstry, S. & Muralt, P. Thin film piezoelectrics for MEMS. *J. Electroceramics* **12**, 7–17 (2004).

2. Kholkin, A. L., Pertsev, N. A. & Goltsev, A. V. Piezoelectricity and Crystal Symmetry. in *Piezoelectric and Acoustic Materials for Transducer Applications* 17–38 (2008).

3. Damjanovic, D. Ferroelectric, dielectric and piezoelectric properties of ferroelectric thin films and ceramics - Abstract - Reports on Progress in Physics. *Reports Prog. Phys.* **61**, 1267 (1998).

4. Martin, L. W. & Rappe, A. M. Thin-film ferroelectric materials and their applications. *Nat. Rev. Mater.* **2**, (2016).

5. Fang, D. *et al.* Advances in developing electromechanically coupled computational methods for piezoelectrics/ferroelectrics at multiscale. *Appl. Mech. Rev.* **65**, (2013).

6. An american national standard IEEE standard definitions of terms associated with ferroelectric and related materials. *IEEE Trans. Ultrason. Ferroelectr. Freq. Control* **50**, 1–32 (2004).

7. Zhu, X., Liu, Z. & Ming, N. Perovskite oxide nanotubes: Synthesis, structural characterization, properties and applications. *J. Mater. Chem.* **20**, 4015–4030 (2010).

8. Bolten, D., Böttger, U. & Waser, R. Reversible and irreversible piezoelectric and ferroelectric response in ferroelectric ceramics and thin films. *J. Eur. Ceram. Soc.* **24**, 725–732 (2004).

9. Benedek, N. A. & Fennie, C. J. Why are there so few perovskite ferroelectrics? *J. Phys. Chem. C* **117**, 13339–13349 (2013).

10. Bassiri-Gharb, N. Dielectric and Piezoelectric Nonlinearities in Oriented Pb(Yb1/2Nb1/2)O3-PbTiO3 Thin Films. (Pennsylvania State University, 2005).

11. Zhuang, Z., Haun, M., Jang, S. & Cross, L. Composition and Temperature-Depndence of the Dielectric, Piezoelectric and Elastic Properties of Pure PZT Ceramics. *IEEE Trans. Ultrason. Ferroelectr. Freq. Control* **36**, 413–416 (1989).

12. Ang, C. & Yu, Z. Dielectric behavior of PbZr0.52Ti0.48O3 thin films: Intrinsic and extrinsic dielectric responses. *Appl. Phys. Lett.* **87**, 3821–3823 (2004).

13. Vonhippel, A. Ferroelectricity, Domain Structure, and Phase Transitions of Barium Titanate. *Rev. Mod. Phys.* **22**, 221–237 (1950).

14. Poplavko, Y., Tsykalov, V. & Molchano, V. Microwave dielectric dispersion of ferroelectric and paralectric phases of barium titanate. *Sov. Phys. Solid State, USSR* **10**, 2708 (1969).

15. Kersten, O., Hofmann, M. & Schmidt, G. Dielectric-Dispersion of Mn-doped Ceramics. Ferroelectrics Letters Section. *Ferroelectr. Lett. Sect.* **6**, 75–80 (1986).

16. Bottger, U. & Arlt, G. Dielectric Microwave Dispersion in PZT Ceramics. Ferroelectrics. *Ferroelectrics* **127**, 95–100 (1992).

17. Herbiet, R., Tenbrock, H. & Arlt, G. The aging behavior of the complex material parameters - ε, d, and s in ferroelectric PZT ceramics. *Ferroelectrics* **74**, 37–53 (1987).

18. Arlt, G., Dederichs, H. & Herbiet, R. 90-Degrees-Domain Wall Relaxation in Tetragonally Distorted Ferroelectric Ceramics. *Ferroelectrics* **74**, 37–53 (1987).

19. Carl, K. & Hardtl, K. Electrical Aftereffects in Pb(Ti,Zr)O3 Ceramics. *Ferroelectrics1987* **17**, 473–486 (1978).

20. Bassiri-Gharb, N. *et al.* Domain wall contributions to the properties of piezoelectric thin films. *J. Electroceramics* **19**, 47–65 (2007).

21. Rayleigh, L. Notes on electricity and magnetism: On the behaviour of iron and steel under the operation of feeble magnetic forces. *Philos. Mag. Ser. 5* **142**, (1887).

22. Kronmuller, H. Theory of rayleigh law in magnetically multiaxial and uniaxial crystals. *Theory rayleigh law Magn. multiaxial uniaxial Cryst.* **32**, C1-390-C391-391 (1971).

23. Taylor, D. V. & Damjanovic, D. Piezoelectric properties of rhombohedral Pb(Zr, Ti)O3 thin films with (100), (111), and 'random' crystallographic orientation. *Appl. Phys. Lett.* **76**, 1615–1617 (2000).

24. Zhang, S., Xia, R. & Shrout, T. Lead-free piezoelectric ceramics vs. PZT? *J. Electroceramics* **19**, 251–257 (2007).

25. Genenko, Y. A., Glaum, J., Hoffmann, M. J. & Albe, K. Mechanisms of aging and fatigue in ferroelectrics. *Mater. Sci. Eng. B* **192**, 52–82 (2015).

26. Brewer, S. J. *et al.* Effect of top electrode material on radiation-induced degradation of ferroelectric thin film structures. *J. Appl. Phys.* **120**, (2016).

27. Aggarwal, S. *et al.* Switching properties of capacitors using electrodes. **75**, 1787–1789 (1999).

28. Alexe, M., Harnagea, C., Hesse, D. & Gösele, U. Polarization imprint and size effects in mesoscopic ferroelectric structures. *Appl. Phys. Lett.* **79**, 242–244 (2001).

29. Bornand, V., Trolier-McKinstry, S., Takemura, K. & Randall, C. A. Orientation dependence of fatigue behavior in relaxor ferroelectric-PbTiO3 thin films. *J. Appl. Phys.* **87**, 3965–3972 (2000).

30. Dawber, M. & Scott, J. F. A model for fatigue in ferroelectric perovskite thin films. *Appl. Phys. Lett.* **76**, 1060–1062 (2000).

31. Huang, F. *et al.* HfO2-Based Highly Stable Radiation-Immune Ferroelectric Memory. *IEEE Electron Device Lett.* **38**, 330–333 (2017).

32. Fowler, J. F. X-ray induced conductivity in insulating materials. *Proc. R. Soc. London. Ser. A. Math. Phys. Sci.* **236**, 464–480 (1956).

33. Oen, O. S. & Holmes, D. K. Cross Sections for Atomic Displacements in Solids by Gamma Rays. *J. Appl. Phys.* **30**, 1289 (1959).

34. Sickafus, K. E. *et al.* Radiation-induced amorphization resistance and radiation tolerance in structurally related oxides. *Nat. Mater.* **6**, 217–223 (2007).

35. Gao, J. *et al.* Total dose radiation effects of Pt/PZT/Pt ferroelectric capacitors fabricated by PLD method. *Semicond. Sci. Technol.* **14**, 836–839 (1999).

36. Gao, J. *et al.* Characteristics of Au/PbZr0.52Ti0.48O3/YBa2Cu3O7−δ capacitors fabricated on LaAlO3 and Y2O3-stabilized ZrO2 infstrates during irradiation. *Philos. Mag. B Phys. Condens. Matter; Stat. Mech. Electron. Opt. Magn. Prop.* **79**, 829–838 (1999).

37. Yang, S. A. *et al.* Gamma-ray irradiation effects on electrical properties of ferroelectric PbTiO3 and Pb(Zr0.52Ti0.48)O3 thin films. *Thin Solid Films* **562**, 185–189 (2014).

38. Baturin, I. *et al.* Influence of irradiation on the switching behavior in PZT thin films. *Mater. Sci. Eng. B Solid-State Mater. Adv. Technol.* **120**, 141–145 (2005).

39. Scott, J. F., Araujo, C. A., Meadows, H. B., McMillan, L. D. & Shawabkeh, A. Radiation effects on ferroelectric thin-film memories: Retention failure mechanisms. *J. Appl. Phys.* **66**, 1444–1453 (1989).

40. Benedetto, J. M., Moore, R. A., Mclean, F. B., Brody, P. S. & Dey, S. K. Sol-Gel Ferroelectric Pzt Capacitors'. *Ieee Trans. Nucl. Sci.* **37**, 1713–1717 (1990).

41. Moore, R. A., Benedetto, J. & Rod, B. J. Total Dose Effect on Ferroelectric PZT Capacitors used as Non-Volatile Storage Elements. *IEEE Trans. Nucl. Sci.* **40**, 1591–1596 (1993).

42. Lee, S. C. *et al.* Total-Dose Radiation Effects on Sol-Gel Derived PZT Thin Films. *IEEE Trans. Nucl. Sci.* **39**, 2036 (1992).

43. Glower, D. D., Hester, D. L. & Warnke, D. F. Effects of Radiation-Induced Damage Centers in Lead Zirconate Titanate Ceramics. *J. Am. Ceram. Soc.* **8**, (965).

44. Broomfield, G. H. The effect of low-fluence neutron irradiation on silver-electroded lead-zirconate-titanate piezoelectric ceramics. *J. Nucl. Mater.* **91**, 23–34 (1980).

45. Hilczer, B. & Kulek, J. Effect of neutron irradiation on the electrical conductivity and current-voltage characteristics of PXZ1-xTx)O3 solid solution. *Ferroelectrics* **18**, (1978).

46. Miclea, C., Tanasoui, C., Miclea, C. F., Spanulescu, I. & Cioangher, M. Effect of neutron irradiation on some piezoelectric properties of PZT type ceramics. *Jounral Phys. IV* **128**, 115–120 (2005).

47. Graham, J. T. *et al.* Neutron irradiation effects on domain wall mobility and reversibility in lead zirconate titanate thin films. *J. Appl. Phys.* **113**, (2013).

48. Henriques, A. *et al.* Crystallographic changes in lead zirconate titanate due to neutron irradiation. *AIP Adv.* **4**, 117125 (2014).

49. Brewer, S. J. *et al.* Enhanced radiation tolerance in Mn-doped ferroelectric thin films. *Appl. Phys. Lett.* **111**, (2017).

50. Bastani, Y. *et al.* Effects of high energy x ray and proton irradiation on lead zirconate titanate thin films dielectric and piezoelectric response. *Appl. Phys. Lett.* **102**, (2013).

51. Proie, R. M. *et al.* Total ionizing dose effects in piezoelectric MEMS relays. *IEEE Trans. Nucl. Sci.* **60**, 4505–4511 (2013).

52. Sayyah, R., Macleod, T. C. & Ho, F. D. Radiation-Hardened Electronics and Ferroelectric Memory for Space Flight Systems. *Ferroelectrics* **413**, 170 (2011).

53. Guo, Y. *et al.* The phase transition sequence and the location of the morphotropic phase boundary region in (1-x)[Pb(Mg1/3Nb2/3)O3]-xPbTiO3 single crystal. *J. Phys. Condens. Matter* **15**, (2003).

54. Park, S. & Shrout, T. R. Characteristics of Relaxor-Based Piezoelectric Single crystals for Ultrasonic Transducers. *IEEE Trans. Ultrason. Piezoelectrics, Freq. Control* (1997).

55. Bokov, A. A. & Ye, Z. G. Recent progress in relaxor ferroelectrics with perovskite structure. *J. Mater. Sci.* **41**, 31–52 (2006).

56. Bastani, Y. & Bassiri-Gharb, N. Processing optimization of lead magnesium niobate-lead titanate thin films for piezoelectric MEMS application. *J. Am. Ceram. Soc.* **95**, 1269–1275 (2012).

57. Johnson-Wilke, R. L. *et al.* Ferroelectric/Ferroelastic domain wall motion in dense and porous tetragonal lead zirconate titanate films. *IEEE Trans. Ultrason. Ferroelectr. Freq. Control* **62**, 46–55 (2015).

58. Park, J. H., Xu, F. & Trolier-McKinstry, S. Dielectric and piezoelectric properties of sol-gel derived lead magnesium niobium titanate films with different textures. *J. Appl. Phys.* **89**, 568–574 (2001).

59. Keech, R. *et al.* Lateral scaling of Pb(Mg1/3Nb2/3)O 3-PbTiO3 thin films for piezoelectric logic applications. *J. Appl. Phys.* **115**, 0–8 (2014).

60. Keech, R., Shetty, S., Wang, K., Trolier-Mckinstry, S. & Ballarini, R. Management of Lead Content for Growth of {001}-Oriented Lead Magnesium Niobate-Lead Titanate Thin Films. *J. Am. Ceram. Soc.* **99**, 1144–1146 (2016).

61. Keech, R. *et al.* Thickness-dependent domain wall reorientation in 70/30 lead magnesium niobate- lead titanate thin films. *J. Am. Ceram. Soc.* **100**, (2017).

62. Mikolajick, T. *et al.* FeRAM technology for high density applications. *Microelectron. Reliab.* **41**, 947–950 (2001).

63. Kim, K. & Lee, S. Integration of lead zirconium titanate thin films for high density ferroelectric random access memory. *J. Appl. Phys.* **100**, (2006).

64. Böscke, T. S., Müller, J., Bräuhaus, D., Schröder, U. & Böttger, U. Ferroelectricity in hafnium oxide thin films. *Appl. Phys. Lett.* **99**, (2011).

65. Müller, J. *et al.* Ferroelectric Zr0.5Hf0.5O2 thin films for nonvolatile memory applications. *Appl. Phys. Lett.* **99**, 0–3 (2011).

66. Müller, J. *et al.* Improved manufacturability of ZrO2 MIM capacitors by process stabilizing HfO2 addition. *Microelectron. Eng.* **86**, 1818–1821 (2009).

67. Müller, J. *et al.* Ferroelectricity in simple binary ZrO 2 and HfO 2. *Nano Lett.* **12**, 4318–4323 (2012).

68. Hyuk Park, M. *et al.* Evolution of phases and ferroelectric properties of thin Hf 0.5Zr0.5O2 films according to the thickness and annealing temperature. *Appl. Phys. Lett.* **102**, 0–5 (2013).

69. Park, M. H. *et al.* Morphotropic Phase Boundary of Hf 1- x Zr x O 2 Thin Films for Dynamic Random Access Memories. *ACS Appl. Mater. Interfaces* **10**, 42666–42673 (2018).

70. Kim, H. J. *et al.* A study on the wake-up effect of ferroelectric Hf0.5Zr0.5O2 films by pulse-switching measurement. *Nanoscale* (2016).

71. Park, M. H. *et al.* Study on the internal field and conduction mechanism of atomic layer deposited ferroelectric Hf0.5Zr0.5O2 thin films. *J. Mater. Chem. C* **3**, 6291–6300 (2015).

72. Grimley, E. D. *et al.* Structural Changes Underlying Field-Cycling Phenomena in Ferroelectric HfO2 Thin Films. *Adv. Electron. Mater.* **2**, (2016).

73. Fengler, F. P. G., Hoffmann, M., Slesazeck, S., Mikolajick, T. & Schroeder, U. On the relationship between field cycling and imprint in ferroelectric Hf0.5Zr0.5O2. *J. Appl. Phys.* **123**, 0–8 (2018).

74. Kim, S. J. *et al.* Large ferroelectric polarization of TiN/Hf0.5Zr0.5O2/TiN capacitors due to stress-induced crystallization at low thermal budget. *Appl. Phys. Lett.* **111**, 0–5 (2017).

75. Park, M. H. *et al.* Study on the size effect in Hf0.5Zr0.5O2 films thinner than 8 nm before and after wake-up field cycling. *Appl. Phys. Lett.* **107**, (2015).

76. Zhou, D. *et al.* Wake-up effects in Si-doped hafnium oxide ferroelectric thin films. *Appl. Phys. Lett.* **103**, (2013).

77. Martin, D. *et al.* Ferroelectricity in Si-Doped HfO2 revealed: A binary lead-free ferroelectric. *Adv. Mater.* **26**, 8198–8202 (2014).

78. Onaya, T. *et al.* Ferroelectricity of HfxZr1−xO2 thin films fabricated by 300 °C low temperature process with plasma-enhanced atomic layer deposition. *Microelectron. Eng.* **215**, 111013 (2019).

79. Chen, K.-Y., Tsai, Y.-S. & Wu, Y.-H. Ionizing Radiation Effect on Memory Characteristics for HfO 2 -Based Ferroelectric Field-Effect Transistors . *IEEE Electron Device Lett.* **40**, 1370–1373 (2019).

80. Xiao, W. *et al.* Thermally Stable and Radiation Hard Ferroelectric Hf 0.5 Zr 0.5 O 2 Thin Films on Muscovite Mica for Flexible Nonvolatile Memory Applications . *ACS Appl. Electron. Mater.* **1**, 919–927 (2019).

81. Sun, Q. *et al.* Total ionizing dose effects of 60Co γ-rays radiation on HfxZr1−xO2 ferroelectric thin film capacitors. *J. Mater. Sci. Mater. Electron.* **31**, 2049–2056 (2020).

82. Assink, R. A. & Schwartz, R. W. 1H and 13C NMR Investigations of Pb(Zr,Ti)O3 Thin-Film Precursor Solutions. *Chem. Mater.* **5**, 511–517 (1993).

83. Wang, L. P. Thesis. (Pennsylvania State University, 2001).

84. Bassiri-Gharb, N., Bastani, Y. & Bernal, A. Chemical solution growth of ferroelectric oxide thin films and nanostructures. *Chem. Soc. Rev.* **43**, 2125–2140 (2014).

85. Furiouslettuce. Bragg Plane Diffraction. (2009).

86. Lotgering, F. Topotactical reactions with ferrimagnetic oxides having hexagonal crystal structures 1. *J. Inorg. Nucl. Chem.* **9**, 113 (1959).

87. Furushima, R., Tanaka, S., Kato, Z. & Uematsu, K. Orientation distribution-Lotgering factor relationship in a polycrystalline material as an example of bismuth titanate prepared by a magnetic field. *J. Ceram. Soc. Japan* **118**, 921–926 (2010).

88. Ramesh, R. *Thin Film Ferroelectric Materials and Devices*. (Springer Science & Business Media, 2013).

89. Griggio, F. & Trolier-McKinstry, S. Grain size dependence of properties in lead nickel niobate-lead zirconate titanate films. *J. Appl. Phys.* **107**, 024105 (2010).

90. Guo, H. & Zhang, J. *Scanning probe microscopy (SPM) of epitaxial oxide thin films*. *Epitaxial Growth of Complex Metal Oxides* (Elsevier Ltd, 2015). doi:10.1016/B978-1-78242-245-7.00011-7.

91. Chin, E. S., Cress, C. D., Rudy, R. Q. & Bassiri-Gharb, N. Effects of Gamma Irradiation on Functional Response of Relaxor-Ferroelectric Thin Films. *IEEE Trans. Ultrason. Ferroelectr. Freq. Control* **67**, 1059–1065 (2020).

92. Scott, J. F. & De Araujo, C. A. P. Ferroelectric Memories. *Science (80-.).* **246**, 1400–1405 (1989).

93. Prinzie, J., Steyaert, M. & Leroux, P. Radiation Effects in CMOS Technology. in *Radiation Hardened CMOS Integrated Circuits for Time-Based Signal Processing, Analog Circuits and Signal Processing* 1–20 (2018).

94. Ovid'ko, I. A. & Sheinerman, A. G. Irradiation-induced amorphization processes in nanocrystalline solids. *Appl. Phys. A* **81**, 1083 (2005).

95. Jin, L., Xi, Z., Xu, Z. & Yao, X. Study of ferroelectric domain morphology in PMN-32% PT single crystals. *Ceram. Int.* **30**, 1695 (2004).

96. Sanchez, L. M. *et al.* Optimization of PbTiO3 seed layers and Pt metallization for PZT-based piezoMEMS actuators. *J. Mater. Res.* **28**, 1920 (2013).

97. Kratzer, M., Lasnik, M., Rohrig, S., Teichert, C. & Deluca, M. Reconstruction of the domain orientation distribution function of polycrystalline PZT ceramics using vector piezoresponse force microscopy. *Sci. Rep.* **8**, (2018).

98. Zeng, H. R. *et al.* Spatial inhomogeneity of ferroelectric domain structure in Pb(Mg1/3Nb2/3)O3-30%PbTiO3 single crystals. *Mater. Lett.* **59**, 238–240 (2005).

99. Huang, J., Dennis Chasteen, N. & Fitzgerald, J. J. X-Band EPR studies of ferroelectric lead titanate (PT), piezoelectric lead magnesium niobate (PMN), and PMN/PT powders at 10 and 85 K. *Chem. Mater.* **10**, 3848–3855 (1998).

100. Vikhnin, V. S., Zakharchenya, R. I., Asatryan, H. R., Kutsenko, A. B. & Kapphan, S. E. Polarons and charge-transfer vibronic excitons in ferroelectric oxides: EPR and photoluminescence studies of PbxNbyOz ceramics. *Appl. Magn. Reson.* **28**, 137 (2005).

101. Warren, W. L., Pike, G. E., Vanheusden, K., Dimos, D. & Tuttle, B. A. Defect-dipole alignment and tetragonal strain in ferroelectrics. *J. Appl. Phys.* **79**, 9250 (1996).

102. Avrami, M. Kinetics of Phase Change. I General Theory. *J. Chem. Phys.* **7**, 1103 (1939).

103. Griggio, F. *et al.* Substrate Clamping Effects on Irreversible Do-main Wall Dynamics in Lead Zirconate Titanate Thin Films. *Phys. Rev. Lett.* **108**, 157604 (2012).

104. Denis, L. M., Esteves, G., Walker, J., Jones, J. L. & Trolier-McKinstry, S. Thickness dependent response of domain wall motion in declamped {001}Pb(Zr0.3Ti0.7)O3 thin films. *Acta Mater.* **151**, 243–252 (2018).

105. Saremi, S. *et al.* Enhanced Electrical Resistivity and Properties via Ion Bombardment of Ferroelectric Thin Films. *Adv. Mater.* **28**, 10750–10756 (2016).

106. Fischer, D. X., Prokopec, R., Emhofer, J. & Eisterer, M. The effect of fast neutron irradiation on the superconducting properties of REBCO coated conductors with and without artificial pinning centers. *Supercond. Sci. Technol.* **31**, (2018).

107. Foltyn, S. R. *et al.* Materials science challenges for high-temperature superconducting wire. *Nat. Mater.* **6**, 631–642 (7AD).

108. Leray, J. L. *et al.* Radiation Effects in Thin-Film Ferroelectric PZT for Non-Volatile Memory Applications in Microelectronics. *J. Phys. III* **7**, 1227–1243 (1997).

109. Bednyakov, P. S., Sluka, T., Tagantsev, A. K., Damjanovic, D. & Setter, N. Formation of charged ferroelectric domain walls with controlled periodicity. *Sci. Rep.* **5**, (2015).

110. Sluka, T., Tagantsev, A. K., Damjanovic, D., Gureev, M. & Setter, N. Enhanced electromechanical response of ferroelectrics due to charged domain walls. *Nat. Commun.* **3**, (2012).

111. Oldham, T. R. & McLean, F. B. Total ionizing dose effects in MOS oxides and devices. *IEEE Trans. Nucl. Sci.* **50**, 483–499 (2003).

112. Claeys, C. L. & Simoen, E. *Radiation Effects in Advanced Semiconductor Materials and Devices*. (2002).

113. Shen, T. D. Radiation tolerance in nanostructure: Is smaller better? *Nucl. Instruments Methods Phys. Res. Sect. B* **266**, 921–925 (2008).

114. Brewer, S. J. *et al.* Effect of microstructure on irradiated ferroelectric thin films. *J. Appl. Phys.* **121**, (2017).

115. Ihlefeld, J. F., Borland, W. J. & Maria, J.-P. Enhanced dielectric and crystalline properties in ferroelectric barium titanate thin films. *Adv. Funct. Mater.* **17**, 1199–1203 (2007).

116. Cho, S. Y., Kwak, J. H., Yang, S. A. & Bu, S. D. Effects of annealing on domain-wall contributions to the dielectric properties of pzt thin films. *J. Korean Phys. Soc.* **63**, 2002–2007 (2013).

117. Liu, G., Zhang, S., Jiang, W. & Cao, W. Losses in ferroelectric materials. *Mater. Sci. Eng. R Reports* **89**, 1–48 (2015).

118. Schwank, J. R., Nasby, R. D., Miller, S. L., Rodgers, M. S. & Dressendorfer, P. V. Total-dose radiation-induced degradation of thin film ferroelectric capacitors. **37**, 1703–1712 (1990).

119. Persson, A. E. O. *et al.* Reduced annealing temperature for ferroelectric HZO on InAs with enhanced polarization. *Appl. Phys. Lett.* **116**, 0–4 (2020).

120. Hur, J. *et al.* Direct Comparison of Ferroelectric Properties in Hf0.5Zr0.5O2 between Thermal and Plasma-Enhanced Atomic Layer Deposition. *Under Rev.*

121. Sun, S., Wang, Y., Fuierer, P. A. & Tuttle, B. A. Annealing effects on the internal bias field in ferroelectric PZT thin films with self-polarization. *Integr. Ferroelectr.* **23**, 25–43 (1999).

122. Jaffe, B., W., C. & H., J. *Piezoeletric ceramics*. *Piezoeletric ceramics* vol. 3 (1971).

123. Tagantsev, A. K. The role of the background dielectric susceptibility in uniaxial ferroelectrics. *Ferroelectrics* **69**, 321–323 (1986).

124. Levanyuk, A. P., Strukov, B. A. & Cano, A. Background dielectric permittivity: Material constant or fitting parameter? *Ferroelectrics* **503**, 94–103 (2016).

125. Boni, G. A. *et al.* Low value for the static background dielectric constant in epitaxial PZT thin films. *Sci. Rep.* **9**, 1–8 (2019).

126. Hoffmann, M. *et al.* Stabilizing the ferroelectric phase in doped hafnium oxide. *J. Appl. Phys.* **118**, (2015).

127. Maurya, S. Effect of zero bias Gamma ray irradiation on HfO2 thin films. *J. Mater. Sci. Mater. Electron.* **27**, 12796–12802 (2016).

128. Kaya, S., Yıldız, I., Lok, R. & Yılmaz, E. Co-60 gamma irradiation influences on physical, chemical and electrical characteristics of HfO2/Si thin films. *Radiat. Phys. Chem.* **150**, 64–70 (2018).

129. Gueye, I. *et al.* Chemistry of surface nanostructures in lead precursor-rich PbZr 0.52 Ti 0.48 O 3 sol-gel films. *Appl. Surf. Sci.* **363**, 21–28 (2016).

130. Gueye, I. *et al.* Operando hard X-ray photoelectron spectroscopy study of the Pt/Ru/PbZr0.52Ti0.48O3 interface. *Appl. Phys. Lett.* **111**, 1–5 (2017).

131. Tani, T. & Payne, D. A. Lead Oxide Coatings on Sol–Gel-Derived Lead Lanthanum Zirconium Titanate Thin Layers for Enhanced Crystallization into the Perovskite

Structure. *J. Am. Ceram. Soc.* **77**, 1242–1248 (1994).

132. SNOW, G. S. Fabrication of Transparent Electrooptic PLZT Ceramics by Atmosphere Sintering. *J. Am. Ceram. Soc.* **56**, 91–96 (1973).

133. Brewer, S. J. Radiation Hardness in Ferroelectric Thin Films for MEMS Applications. (Georgia Institute of Technology, 2017).

134. Zhang, W. L. *et al.* Impact of Radiation Effect on Ferroelectric Al- doped HfO 2 Metal-Ferroelectric-Insulator- Semiconductor Structure. **2**, 8–13 (2020).

135. Fengler, F. P. G. *et al.* Analysis of Performance Instabilities of Hafnia-Based Ferroelectrics Using Modulus Spectroscopy and Thermally Stimulated Depolarization Currents. *Adv. Electron. Mater.* **4**, 1–11 (2018).